

X-Ray Crystal Structure of a Ribosomal Protein S6, S15, S18: rRNA Complex from *T. thermophilus*, and Investigation of Conformational Changes in 16S rRNA Fragments from *B. stearothermophilus* During Ribonucleoprotein Assembly

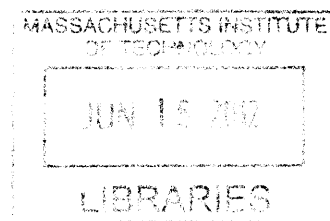
by
Peter M. Funke

B.S. in Chemistry with Honors, B.S. in Physics
The Pennsylvania State University, 1995

Submitted to the Department of Chemistry in Partial Fulfillment of the
Requirements for the Degree of

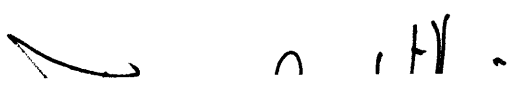
Master of Science
in Chemistry

at the
Massachusetts Institute of Technology
February, 2012



ARCHIVES

© 2012 Massachusetts Institute of Technology.
All Rights Reserved

Signature of Author: _____
 Department of Chemistry
January 6, 2012

Certified by: _____
James R. Williamson
Professor of Chemistry and Molecular Biology, The Scripps Research Institute
Thesis Supervisor

Accepted by: _____
Professor Robert Field
Chair, Department Committee on Graduate Students

X-Ray Crystal Structure of a Ribosomal Protein S6, S15, S18: rRNA Complex from *T. thermophilus*, and Investigation of Conformational Changes in 16S rRNA Fragments from *B. stearothermophilus* During Ribonucleoprotein Assembly

by

Peter M. Funke

Submitted to the Department of Chemistry on January 6, 2012 in Partial Fulfillment of the Requirements for the Degree of Master of Science in Chemistry

Abstract

The X-ray crystallographic structure of a fragment of the 30S ribosomal subunit from *Thermus thermophilus* containing ribosomal proteins S6, S15, S18, and a minimal rRNA binding site (T4 RNP) containing two different three-helix junctions was solved to 2.6 Å. The protein S15 contains four bundled α -helices and binds the rRNA along the minor groove of helix 22 and contacts elements of both three-helix rRNA junctions. The protein S6 contains a four-stranded β -sheet buttressed by two α -helices and forms a heterodimer with S18, a poorly structured protein with both α -helices and random coil elements. The S6:S18 heterodimer binds across the helix 22, helix 23, helix 23a RNA junction and makes no direct contacts to S15. Time-resolved fluorescence resonance energy (trFRET) methods were used to assess conformational changes in both RNA three-helix junctions in separate model systems from *Bacillus stearothermophilus*. Helix 21 and helix 23 are shown to stack coaxially onto each end of helix 22 in the absence of either S15 or divalent magnesium ions. S15 and magnesium are both shown to stabilize a reorganization of the helix 20, helix 21, helix 22 RNA junction, whereby helix 20 rotates proximal to helix 22. Single-pair fluorescence resonance energy transfer (spFRET) methods were used to show a conformational change in individual RNA molecules in solution upon addition of either S15 or magnesium. We also observe individual subpopulations of unbound and bound RNA as we titrate S15 around the known protein dissociation constant K_d . We incorporate our structural information into a more detailed model of cooperative binding between S15 and the S6:S18 heterodimer during T4 RNP formation, and address the implications for sequential protein binding in the central domain during 30S subunit assembly.

Thesis Supervisor: James R. Williamson

Title: Professor of Chemistry and Molecular Biology, The Scripps Research Institute

Table of Contents

Abstract 2

Chapter 1: A Golden Age of Ribosome Structural Biology 5

1.1 The ribosome is central to all living organisms 5

1.2 30S particles can assemble independently 9

1.3 30S central domain an interesting target for detailed structural investigation 11

1.4 The pace of ribosome structural biology has been breathtaking 11

Chapter 2: X-ray crystal structure of the S6, S15, S18: rRNA complex from *T. thermophilus* 14

2.1 Introduction 14

2.2 Crystallization of central domain RNPs 16

2.3 Data collection and processing 18

2.4 The T4 RNP structure 24

2.5 Discussion 32

Chapter 3: Investigation of conformational changes in fragments of *B. stearothermophilus* 16S rRNA monitored by fluorescence spectroscopy 36

3.1 Introduction 36

3.2 Time-resolved fluorescence resonance energy transfer (trFRET) as a method to measure distances in large biomolecules 37

3.3 Distance measurements in a linear duplex RNA molecule 39

3.4 Magnesium-stabilized conformational change in the helix 20, helix 21, helix 22 junction of 16S rRNA 42

3.5 BS15 induced conformational change in the helix 20, helix 21, helix 22 rRNA 50

3.6 Conformation of the helix 22, helix 23, helix 23a rRNA junction upon magnesium chloride titration.	55
3.7 Single-pair FRET (spFRET) observation of helix 20, helix 21, helix 22 rRNA conformational subpopulations	57
3.8 Discussion.....	63
Chapter 4: Materials and Methods	69
4.1 Reagents	69
4.2 T4 RNP crystallography	70
4.3 Time-resolved fluorescence resonance energy transfer (trFRET).....	71
4.4 Single-pair fluorescence resonance energy transfer (spFRET).....	72
Bibliography.....	74

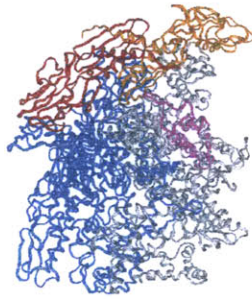
Chapter 1: A Golden Age of Ribosome Structural Biology

1.1 The ribosome is central to all living organisms

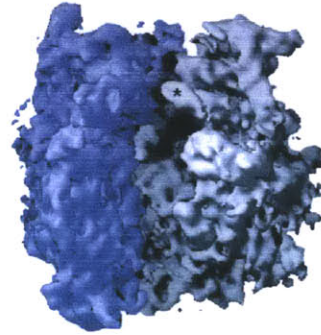
Francis Crick postulated the Central Dogma of biology as the one way transfer of sequence information from DNA into RNA, and the subsequent translation of this genetic information into protein (Figure 1.1) (Crick, 1970). The translation step in the Central Dogma is carried out by the ribosome, an ancient and massive complex of three large rRNAs and over 50 proteins which links genotype and phenotype. A detailed knowledge of ribosome structures is essential to understanding function, both as a conceptual framework to consolidate decades of detailed biochemical information, and to facilitate the design of new experiments to more precisely address outstanding question of ribosome function.

Extensive biochemical studies have elucidated the basic steps in translation of mRNA into polypeptides. This complicated process is often divided loosely into two separate steps: initiation of protein synthesis by formation of the 70S initiation complex, and elongation of nascent proteins by peptidyltransferase activity (Figure 1.2). Formation of the 70S initiation complex involves many individual steps, including the *in vivo* assembly of the individual 30S and 50S ribosomal subunits. These subunits are themselves massive particles: the *E. coli* 30S ribosomal subunit contains a 1542 nucleotide 16S rRNA and 20 'S' proteins, and the 50S particle contains a 115 nucleotide 5S rRNA, a 2904 nucleotide rRNA, and 34 'L' proteins (Figure 1.3) (Gutell, 1994). During initiation the 30S subunit is bound by initiation factors IF-1, IF-2, and IF-3. This complex then binds the mRNA in the decoding region of the 16S rRNA and f-met tRNA in the 30S P site upon release of IF-3 to form the 30S initiation complex. This step can be inhibited by the bacteriostat spectinomycin. This 30S initiation complex then binds the 50S subunit upon release of IF-1 and IF-2 to form the 70S initiation complex. This step can be blocked by aminoglycoside antibiotics like streptomycin, kanamycin, and neomycin.

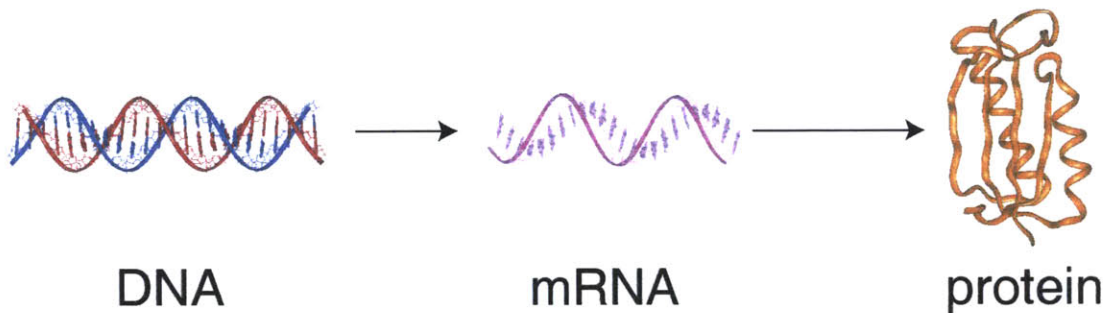
Central Dogma of Biology



RNA polymerase
Zhang, et al., *Cell*, **98**, 1999.



70S ribosome
Cate, et al., *Science*, **285**, 1999.



The ribosome links genotype to phenotype!

Figure 1.1 *The central dogma of biology*. DNA is first transcribed into messenger RNA (mRNA) by an RNA polymerase. This mRNA is then translated into protein by the ribosome. This one way process links genotype to phenotype!

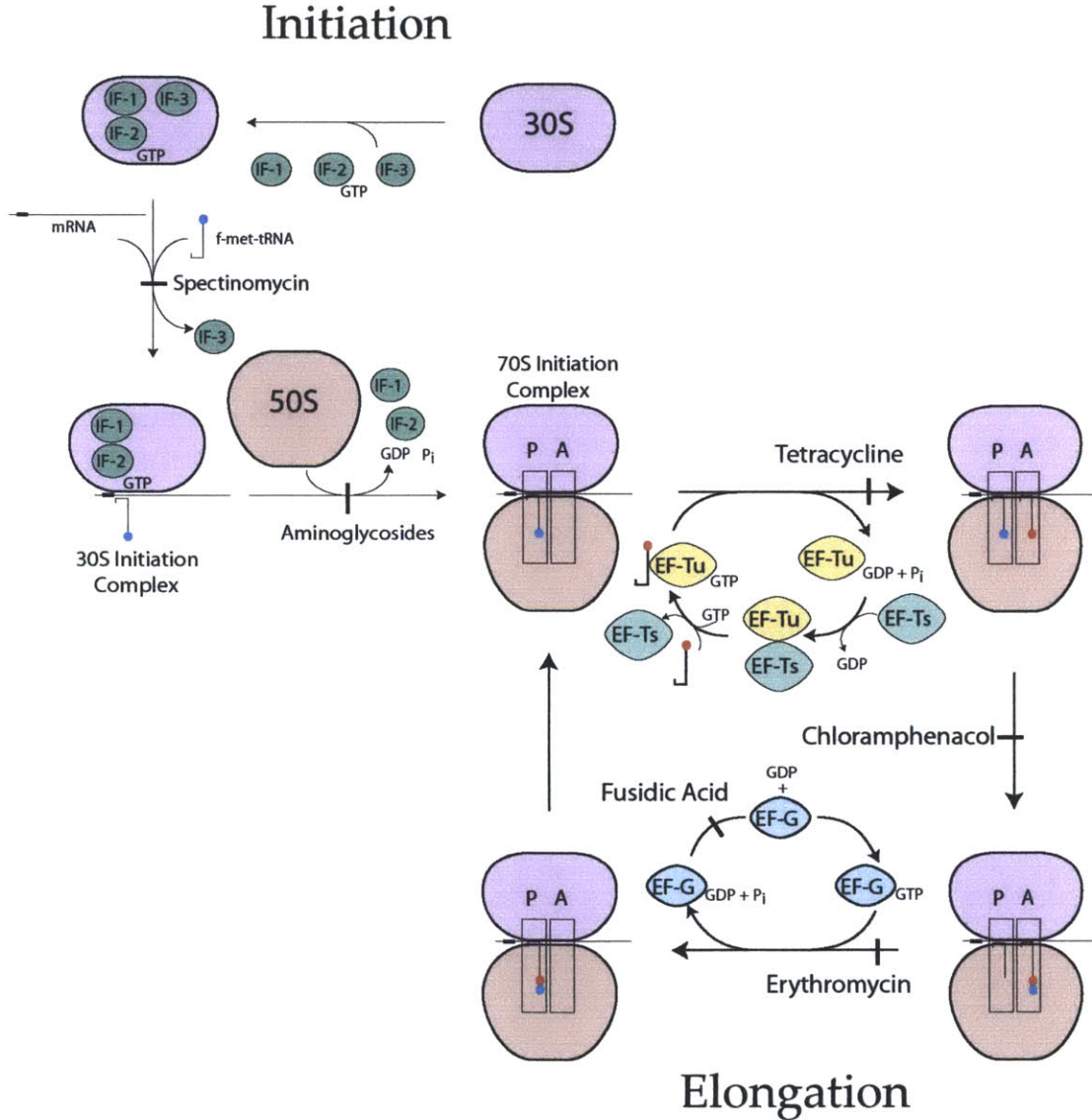


Figure 1.2 *Ribosome formation and function.* The 30S ribosomal subunit is initially bound by initiation factors IF-1, IF-2-GTP, and IF-3. mRNA binds this complex, along with f-Met-tRNA, and IF-3 is released to form the 30S initiation complex. The 50S subunit joins to form the 70S initiation complex, and the other two initiation factors are released. The f-met-tRNA is located in the P-site, ready for peptidyltransferase activity. Aminoacyl-tRNAs are delivered to the A-site of the 70S initiation complex by the elongation factor Tu (EF-Tu)-GTP complex, which is formed with elongation factor Ts (EF-Ts). The ribosome then performs its primary function and creates a peptide bond between the amino acids in the P-site and A-site. The growing polypeptide is cycled from the A-site to the P-site with help from elongation factor G (EF-G), and the ribosome is reset to continue the polypeptide elongation process. Many of these steps are targets for small molecule bacterial antibiotics.

Ribosome Anatomy

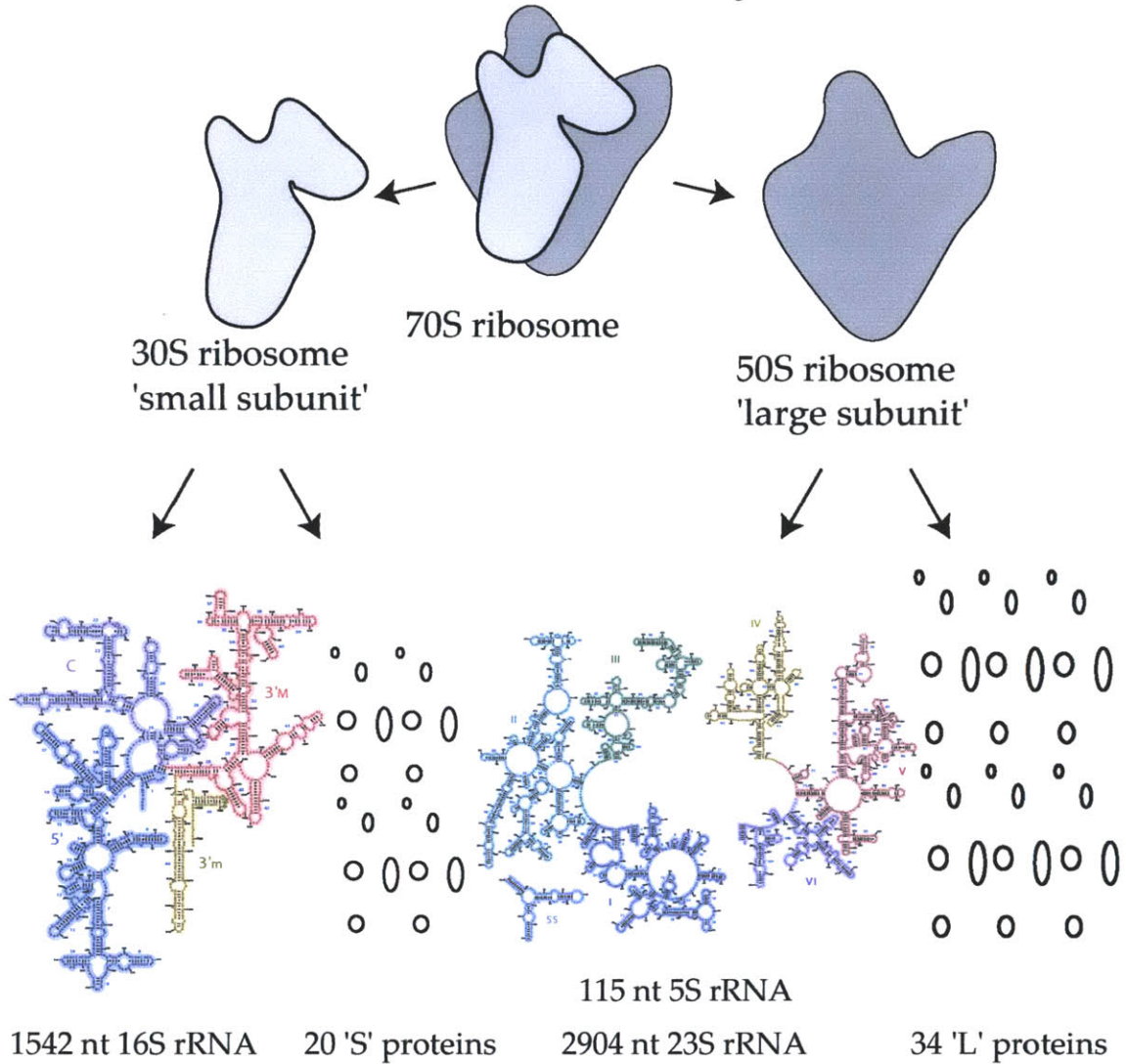


Figure 1.3 *Ribosome Anatomy*. The *E. coli* 70S ribosome is composed of two subunits: 30S and 50S. The 30S subunit is composed of a 1542 nucleotide 16S rRNA and 20 'S' proteins. The 50S subunit is composed of a 115 nucleotide 5S rRNA, a 2904 nucleotide 23S rRNA, and 34 'L' proteins.

The elongation step in polypeptide synthesis begins with formation of a ternary complex containing an aminoacyl-tRNA, elongation factor Tu (EF-Tu), and GTP. This ternary complex is formed through the activity of elongation factor Ts (EF-Ts). The aminoacyl-tRNA is placed in the A-site, and this step can be halted by the bacteriostat tetracycline, which binds reversibly to the 30S ribosome. The peptide bond is formed through the peptidyltransferase activity of the 50S P-site. This protein-independent activity is located in the 23S rRNA and can be blocked by the bacteriostat chloramphenicol. The growing polypeptide is moved from the A-site to the P-site by elongation factor G (EF-G) and the ribosome is reset for another round of peptide bond formation and polypeptide elongation. This step can be inhibited by the macrolide erythromycin, a bacteriostat which inhibits translocation of the growing polypeptide, and by fusidic acid, a bacteriostat which disrupts the function of EF-G.

1.2 30S particles can assemble independently.

In the late 1960s and early 1970s Masayasu Nomura and colleagues showed functional 30S and 50S ribosome subunits could be reconstituted *in vitro* from their individual ribosomal proteins and rRNAs (Traub and Nomura, 1968; Fahnestock, *et al.*, 1973). These fascinating results suggested all the information necessary for subunit assembly was encoded in the constituent proteins and RNAs themselves.

Extensive investigation of the order of addition led Nomura and colleagues to develop a detailed map of the 30S assembly process (Fig. 1.4) (Nomura, 1973). This map indicated a cooperative process, in which a set of proteins initially bind the 16S rRNA, and another set of proteins bind this partially assembled particle. This map has been supplemented with other biochemical data to produce a more complete picture of 30S assembly that includes both temporal and spatial information.

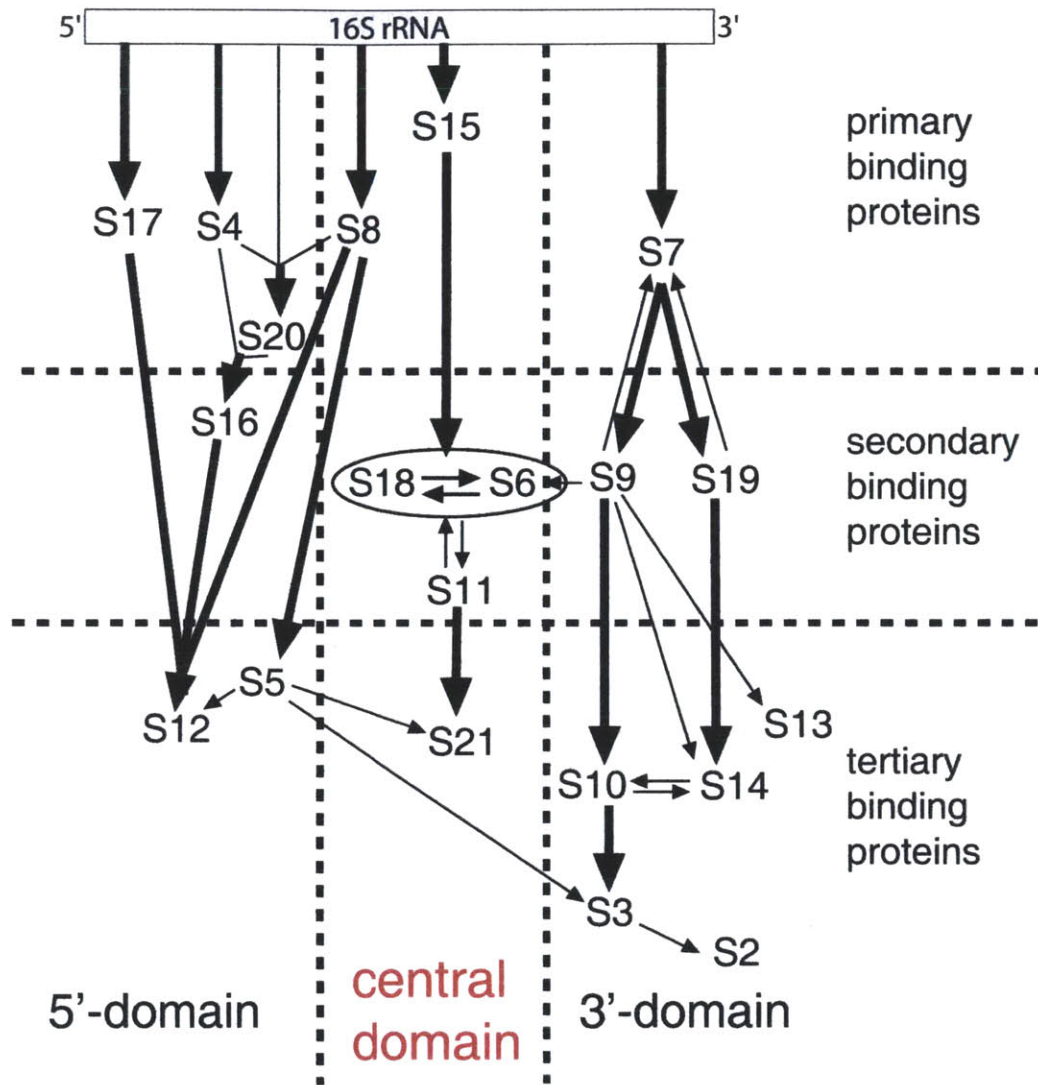


Figure 1.4 30S Assembly Map. The 30S ribosome assembly map suggests both a spatial and temporal relationship of ribosomal protein binding to 16S rRNA. Many primary binding proteins are found in the 5' and central domains, while many secondary and tertiary binding proteins are found in the central and 3' domains.

1.3 30S central domain an interesting target for detailed structural investigation

An abundance of previous studies had made the central domain of the 30S ribosomal subunit an attractive target for structural investigation when this project was started. In the mid 1990s Robert Batey determined a minimal rRNA binding site for *Bacillus stearothermophilus* S15 consisting of a three-helix rRNA junction (Batey and Williamson, 1996a). These studies led to our first successful targets for crystallization of an S15:rRNA complex. Robert's work also indicated both the basic protein S15 and multivalent cations, including magnesium, cobalt, and spermidine, could induced an rRNA conformational change as indicated by enhanced polyacrylamide gel electrophoresis (PAGE) mobility (Batey and Williamson, 1998). The details of the RNA conformational change were further investigated in our lab by Jeff W. Orr using transient electric birefringence techniques and solid supported single molecule fluorescence resonance energy transfer (Orr, *et al.*, 1998; Ha, *et al.*, 1999; Kim, *et al.*, 2002). Sultan Agalarov investigated details of central domain assembly in *Thermus thermophilus*, and showed the core of the central domain rRNA was necessary for binding proteins S6, S8, S11, S15, and S18, but that distal portions of the central domain rRNA are not necessary for protein binding (Agalarov, *et al.*, 1998; Agalarov and Williamson, 2000). These studies led to the RNP complex we eventually used for X-ray crystallographic studies, a quaternary complex of the proteins S6, S15, S18 and a minimal rRNA containing two three-helix rRNA junctions (the 'T4' particle). These studies also hinted at a mechanism of 30S central domain assembly, first with the formation of a multi-protein 'core' structure, followed by folding of more distal RNA elements onto this preformed structure.

1.4 The pace of ribosome structural biology has been breathtaking.

Structural studies of ribosomes began in the 1960s with observation of whole ribosomes and individual subunits by electron microscopy (Inouye, *et al.*, 1964). Three dimensional image reconstruction techniques produced density maps with

30 Å resolution by the mid 1980s (Yonath, *et al.*, 1987). These results were augmented with immuno electron microscopy and neutron diffraction studies to determine the relative position of individual proteins within the *E. coli* 30S subunit (Capel and Moore, 1988).

The atomic resolution X-ray crystallographic and NMR structures of individual ribosomal proteins began to appear slowly. The first atomic resolution protein structure was L7/L12 (Leijonmarck and Liljas, 1987). The rate of appearance of ribosomal protein structures increased, with seven structures published in the next decade, and six structures published in 1998 alone.

The first ribonucleoprotein complexes of individual ribosomal proteins and minimized rRNA binding sites appeared in 1999. These included both NMR and X-ray structures of the L25 protein bound to 5S rRNA (Stoldt, *et al.*, 1999; Lu and Steitz, 2000), and an X-ray structure of an L11-23S rRNA complex (Wimberly, *et al.*, 1999). Also, 5 Å maps of the 50S ribosome, 5.5 Å maps of the 30S ribosome, and 7.8 Å maps of 70S ribosomes hinted at things to come (Ban *et al.*, 1999; Clements *et al.*, 1999; Cate *et al.*, 1999). These discoveries were a prelude to 2000, a year of unprecedented discovery of ribosome structure.

Our structure of the quaternary S6, S15, S18 - rRNA complex from the 30S central domain finally appeared in the spring of 2000 (Agalarov, *et al.*, 2000). This was the first atomic resolution structure of a multi protein-rRNA complex, and was viewed as a major accomplishment. Our excitement was quickly overshadowed, however, by a 2.4 Å structure of the 50S ribosome, and a 3.05 Å structure of the 30S ribosome (Ban, *et al.*, 2000; Wimberly, *et al.*, 2000). Low resolution X-ray crystal structures of 70S ribosomes quickly followed (Yusupov, *et al.*, 2001), and ever since there has been a flood of new ribosome structures, including intermediates bound to tRNAs, mRNAs, elongation factors, and antibiotics. A search of the RCSB data base in July 2011 returned 330 hits for the search term "30S ribosome".

While our thunder had been stolen, and our 'divide and conquer' approach to ribosome structures had been overtaken by the 'brute force' approach, these structures were a reason to celebrate, for they gave us the information we so desired and pointed the way to more detailed investigation of ribosome function and assembly. To this end we used fluorescence techniques to revisit conformational changes in a T4-like rRNA system from *B. stearothermophilus* address details of sequential assembly in the T4 particle as a model system for 30S central domain assembly.

Chapter 2: X-ray crystal structure of the S6, S15, S18: rRNA complex from *T. thermophilus*

2.1 Introduction

We embarked on an X-ray crystallography project to determine the atomic resolution structure of a ribonucleoprotein complex containing protein S15. Determination of the three-dimensional structure of biomolecules by X-ray crystallography is a multi-step, iterative process, in which many of the individual steps are rate-limiting to the overall process (Figure 2.1). The first step in structure determination is choosing a biomolecule or engineered variant as an initial target, and choosing the specific organism from which that target comes. Some biomolecules are better than others at forming diffraction-quality crystals, particularly molecules that are ‘compact’, and often molecules from thermophilic organisms. We chose initially to investigate an S15:rRNA complex from *B. stearothermophilus*, and later switched to a more interesting S6, S15, S18: rRNA complex from *T. thermophilus*.

Diffraction quality crystals are often produced by sitting-drop vapor diffusion. A small drop of buffered solution containing the biomolecule target gently evaporates to equilibrium with a nearby reservoir of buffer, raising the concentration of biomolecule until crystal nucleation and formation are favored. The conditions suitable for crystal growth are often determined by screening components of the buffered solution. These include, but are not limited to, the choice of buffer and pH of the solution, the concentrations and variety of mono- and divalent salts, and the addition of precipitation agents. Another variable for screening is the biomolecule target itself. RNA-Protein complexes of biological interest are often parts of larger cellular structures, and a systematic process of minimization can lead to targets that form crystals more readily. After initial crystals have been obtained they are screened in-house for both X-ray diffraction quality and for the ability to bind heavy metals for multiple isomorphous replacement (MIR) phase determination. Small crystals are soaked in cryo protectant solutions to find conditions that allow for rapid freezing in liquid nitrogen, and then for data collection from crystals imbedded in a glassy matrix. Crystals are then soaked in dilute solutions of heavy metals to find condi-

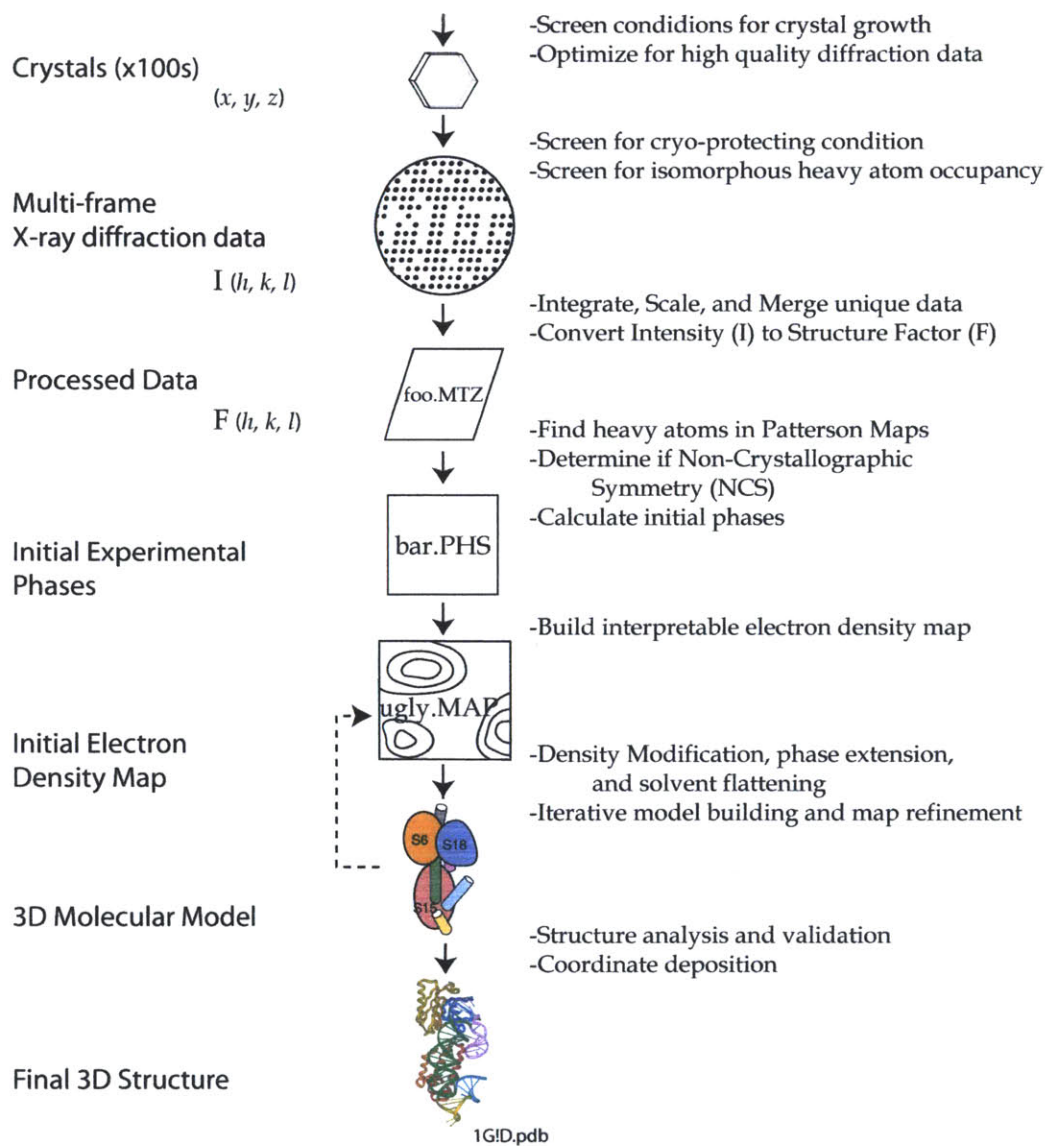


Figure 2.1 *Flow chart for crystallography process.* Diffraction quality crystals are screened for, and grown in quantity for high resolution X-ray diffraction data collection. Heavy-atoms are soaked into the crystals for multiple isomorphous replacement (MIR) phasing methods. Heavy atom positions are found in patterson maps, initial phases are calculated, and initial electron density maps are built. These phases and maps are iteratively refined through rounds of model building, density modification, phase extension, and solvent flattening. The structure goes through a final round of structure validation before deposition of the coordinates in the Protein Data Bank (PDB).

tions that promote metal binding without damaging the crystals or changing their dimensions. Preliminary data collection is used to determine the space group and unit cell dimensions. High quality crystals are then taken to a synchrotron X-ray source for high resolution data collection. The high intensity synchrotron X-ray beam allows for rapid data collection, less radiation damage to the crystals, and higher angle reflections. The diffraction data are recorded on a solid-state image plate detector for both native crystals and metal soaked crystals, and the full and partial reflections from each image are merged into a complete data set. Multiple isomorphous replacement (MIR) is used to generate phase information for the X-ray reflections. The location of heavy atoms soaked into the crystals are found in Patterson maps and combined with non-crystallographic symmetry (NCS) information to calculate initial phases. These initial phases are used to calculate a first, crude electron density map, into which we build an initial structural model based on known sequence information. The structural model is then used to back calculate electron density, thus beginning a laborious process of iterative map refinement and new model building. The new electron density is further improved by solvent flattening and phase extension, and the process repeated until there is no more improvement on the electron density.

2.2 Crystallization of central domain RNPs.

The bacterial ribosomal protein S15 and a minimal rRNA binding site from the central domain of the *Bacillus stearothermophilus* 30S ribosome were chosen as initial structural target (BS15:Fr12 rRNA, Figure 2.2). The protein S15 was cloned from *B. stearothermophilus* and overexpressed in *E. coli*, and the minimal rRNA binding site from 16S rRNA was produced by *in-vitro* run-off transcription (Batey and Williamson, 1996a). Using sparse-matrix and grid-screening techniques we found two separate crystallization conditions using hanging-drop vapor diffusion. These conditions for crystallization were surprisingly different, one containing 1.8 M ammonium sulfate, and the other containing 40% (w/v) PEG 6000. These initial crystals showed great promise and diffracted to 2.65 Å in-house, but they also proved difficult to grow.

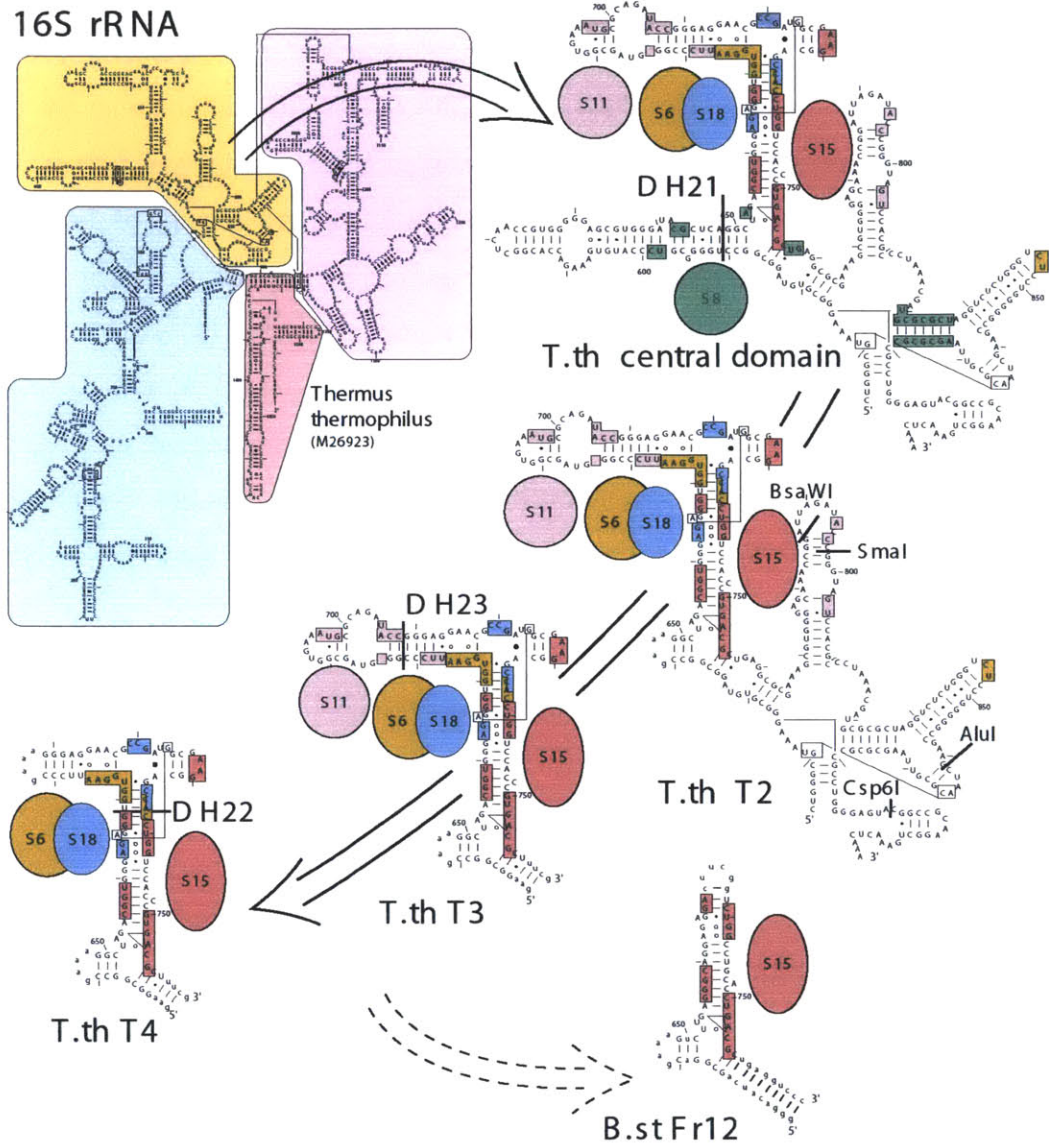


Figure 2.2 *Central Domain RNP minimization*. The S15:Fr12 rRNA complex from *B. stearothermophilus* (lower right) was chosen as our initial structure target for crystal screening. Subsequently a series of minimal RNPs from the central domain of the *T. thermophilus* 30S ribosomal subunit were characterized. The T4 particle was chosen as a new structure target based on compactness as measured by centrifugation, and contains proteins S6, S15, and S18, and an rRNA consisting of the entire helix 22 and portions of the three-helix junctions at each end.

A separate investigation into the assembly of the 30S central domain in *Thermus thermophilus* led us to a new structure target (Figure 2.2) (Agalarov and Williamson, 2000). A minimal RNP (*T.th* T4) containing the three ribosomal proteins S6, S15, S18, and a minimal RNA binding site was chosen as an attractive crystallization target because it appeared compact by centrifugation. The crystallization conditions for the *B. st.* Fr12:S15 complex were used as a starting point for crystallization screening of the *T.th.* T4 particle by Sultan Agalarov. Sultan eventually found a condition with 1.8 M lithium sulfate, 20 mM magnesium chloride, and 50 mM potassium cacodylate (pH 6.5) that promoted crystallization (Figure 2.3). Although the first crystals were small specks, conditions were refined to promote growth of needle shaped crystals, and finally large single hexagonal crystals suitable for high resolution X-ray data collection. As the crystallization of the quaternary T4 RNP particles improved, we shifted our attention away the binary Fr12:BS15 and focused all our effort on this system.

2.3 Data collection and processing.

Initial in-house screening of *T.th.* T4 crystals was performed in San Diego at The Scripps Research Institute on a Siemens X-ray generator with a rotating copper anode at 1.54 Å, or in the Xuong lab at UCSD using a custom copper anode (Figure 2.4). The crystals were flash frozen in liquid nitrogen in a 20% glycerol cryo protectant buffer solution and the data were collected on MAR 345 image plate detectors. The best in-house data extended to 3.5 Å on single images. Unfortunately the long exposure times of 15 to 20 minutes per image resulted in severe radiation damage to the crystals. Images collected toward the end of a 60 image data set were of poor quality and were difficult or impossible to merge with the initial images.

High resolution X-ray data were collected at the Stanford Synchrotron Radiation Laboratory (SSRL) Spear2 ring on beam line BL 7.1 at 1.08 Å and on BL 9.1 at 0.98 Å. The first truly useful data set contained reflections extending to 2.89 Å. These data were acquired in 60 second images, greatly reducing radiation-induced damage to the crystals and allowing for merging of all images into a complete data set. Better data were later collected to 2.60 Å and incorporated into the model building and refinement process. Heavy-atom

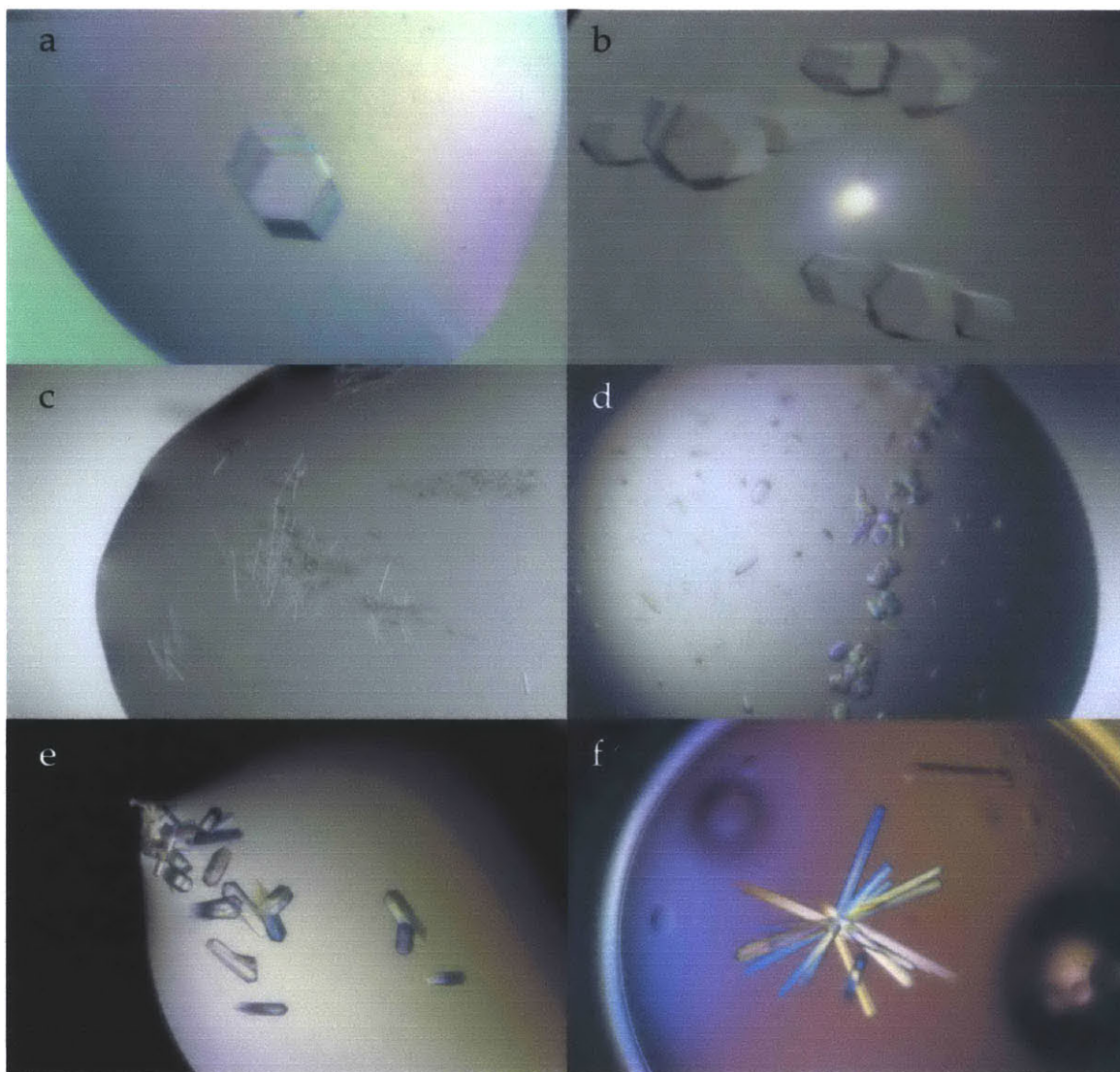


Figure 2.3 *T. thermophilus* crystal photos. a) Diffraction quality hexagonal birefringent crystal suitable for high resolution X-ray data collection. b) Poor quality multi-crystal chunks. c) Small needle-like crystals unsuitable for data collection. d) Small chunk crystals unsuitable for data collection. e) Small rod-like crystals suitable for data collection and heavy atom screening. f) Long rod-like crystals suitable for screening.

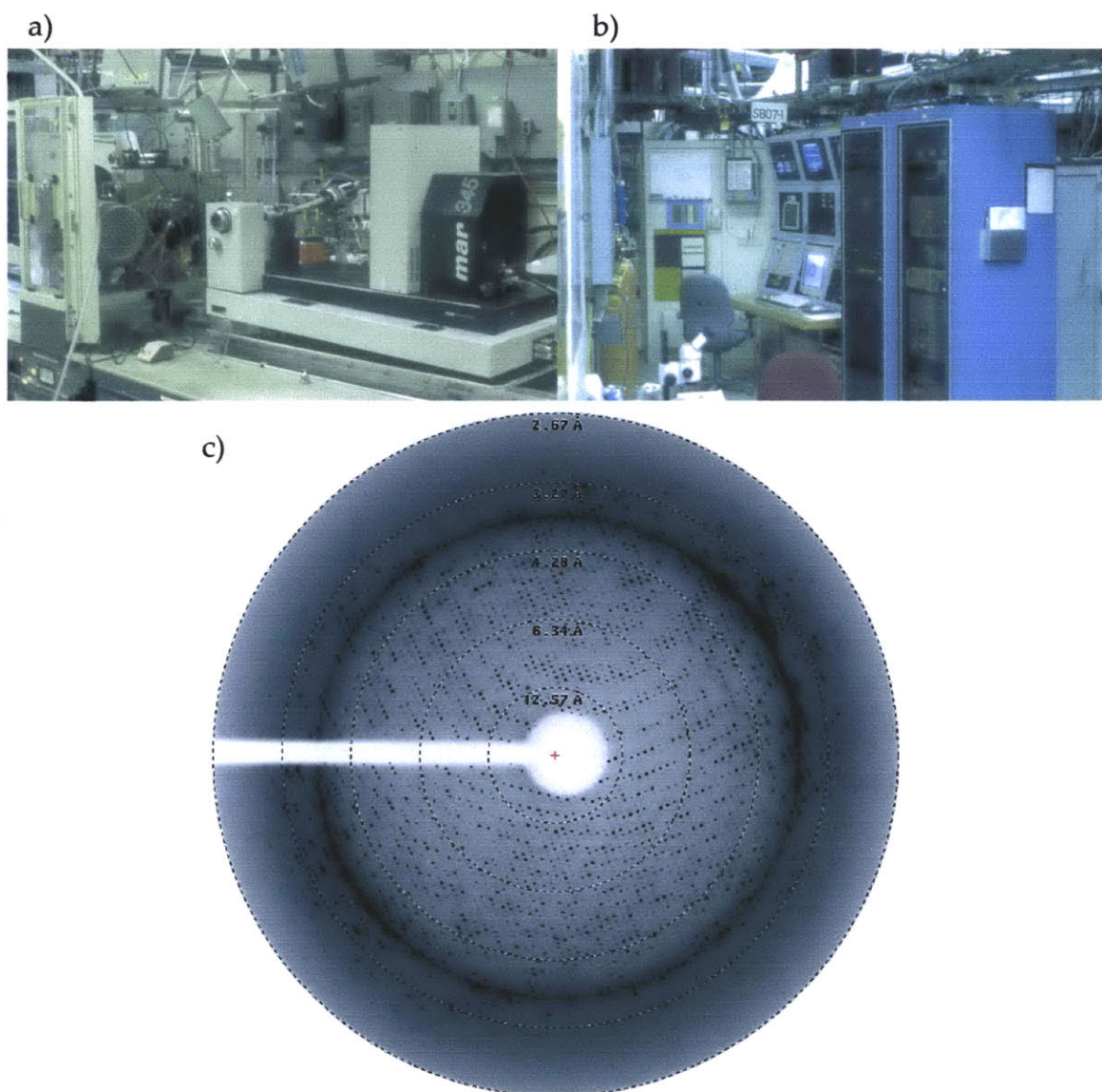


Figure 2.4 *X-ray data collection from T4 RNP crystals.* a) Initial data were collected at UCSD in the laboratory of Dr. Xuong using a custom copper anode X-ray generator and a MAR 345 image plate detector. b) High-resolution data were collected at Stanford Synchrotron Research Laboratory (SSRL) Spear2 ring on beam line 7.1, also with a Mar 345 detector. c) Sample data from a native crystal.

soaked crystals were also screened at SSRL. The short exposures times and rapid image plate read-out allowed for collection of ~20 data sets in sixty four hours of beam time.

The initial data processing was carried out on-site using MOSFLM (Leslie, 1994). Whole and partial reflections on each image were identified, integrated for intensity, and combined into a complete data set. The lowest symmetry space group was $P6_5$, with two copies of the RNP complex in the asymmetric unit. The unit cell dimensions of the crystal were $169 \text{ \AA} \times 169 \text{ \AA} \times 113.5 \text{ \AA}$, and the RNPs filled approximately 30 percent of the space in the crystals. Heavy-atom binding sites for phase determination by MIR were found in patterson maps and difference fourier maps using the XtalView software package (McRee, 1999). Integrated processed native data and isomorphous heavy-atom data were used to generate initial noisy maps. After much searching, peaks representing a heavy atom binding sites of a uranium-derivatized crystal was found (Figure 2.5). Omit maps were used to improve these initial maps, and to search for other derivative binding sites in lead and mercury soaked crystals. Initial phases for the electron density maps were generated from the position of the uranium derivative using the CCP4 program MLPHARE. Eventually the experimental phases were extended to 3.5 \AA using data from seven heavy atom derivatives (Agalarov, *et al.*, 2000). These electron density maps, while noisy, contained elements clearly recognizable as RNA phosphate backbone. Phosphate atoms were modeled into the electron density in an initial round of model building. The maps were recalculated and the phases extended to 2.8 \AA using non-crystallographic symmetry (NCS) averaging, solvent flattening, histogram matching, and SigmaA phase extension using the CCP4 program DM. The model was further refined to 2.6 \AA using iterative rounds of positional and *B*-factor refinement resulting in final electron density maps and a finished structure (Figure 2.6). An initial R_{free} of 29.8 % was reported using 2.3 % of the data, and R_{cryst} was reported as 26.6 %. The electron density maps were particularly poor for the distal portion of helix 23 RNA, and only a few RNA residues could be modeled. Also, portions of protein S18, including the first 30 N-terminal residues, and a few short segments in the middle of the protein showed either weak or no electron density. After deposition of our structure in the PDB, we incorporated an S18 structure from a 30S crystal structure (1FJF.pdb) into our refinement and the maps were recalculated (Wimberley,

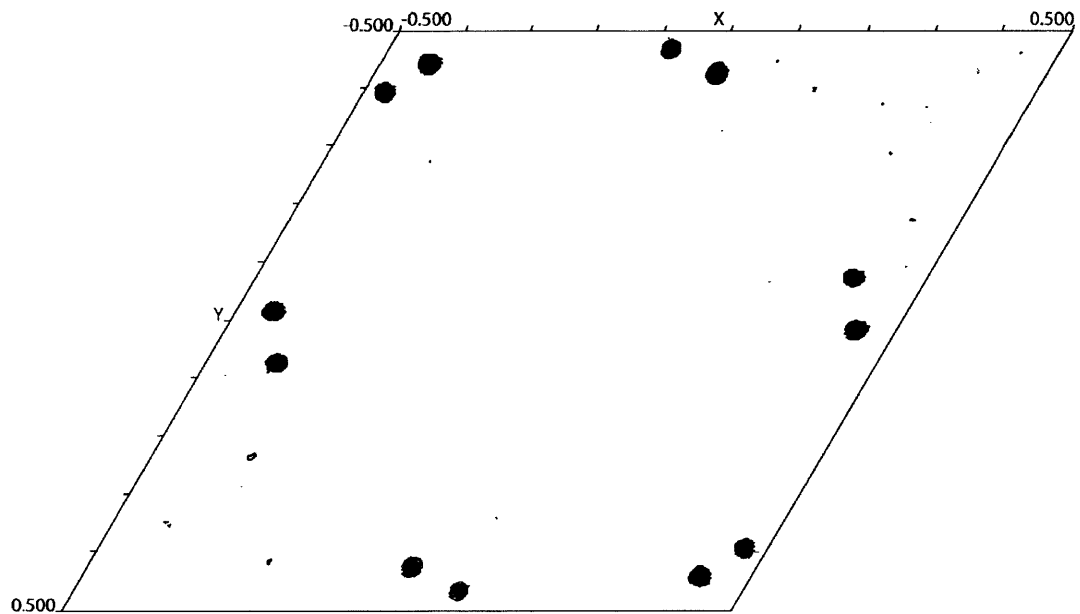


Figure 2.5 Patterson omit map. Uranium-derivatized T4 RNP crystal omit map against the native high-resolution data. The 12 heavy atom peaks show 6-fold symmetry of the crystal and two copies of the RNP complex in the asymmetric unit.

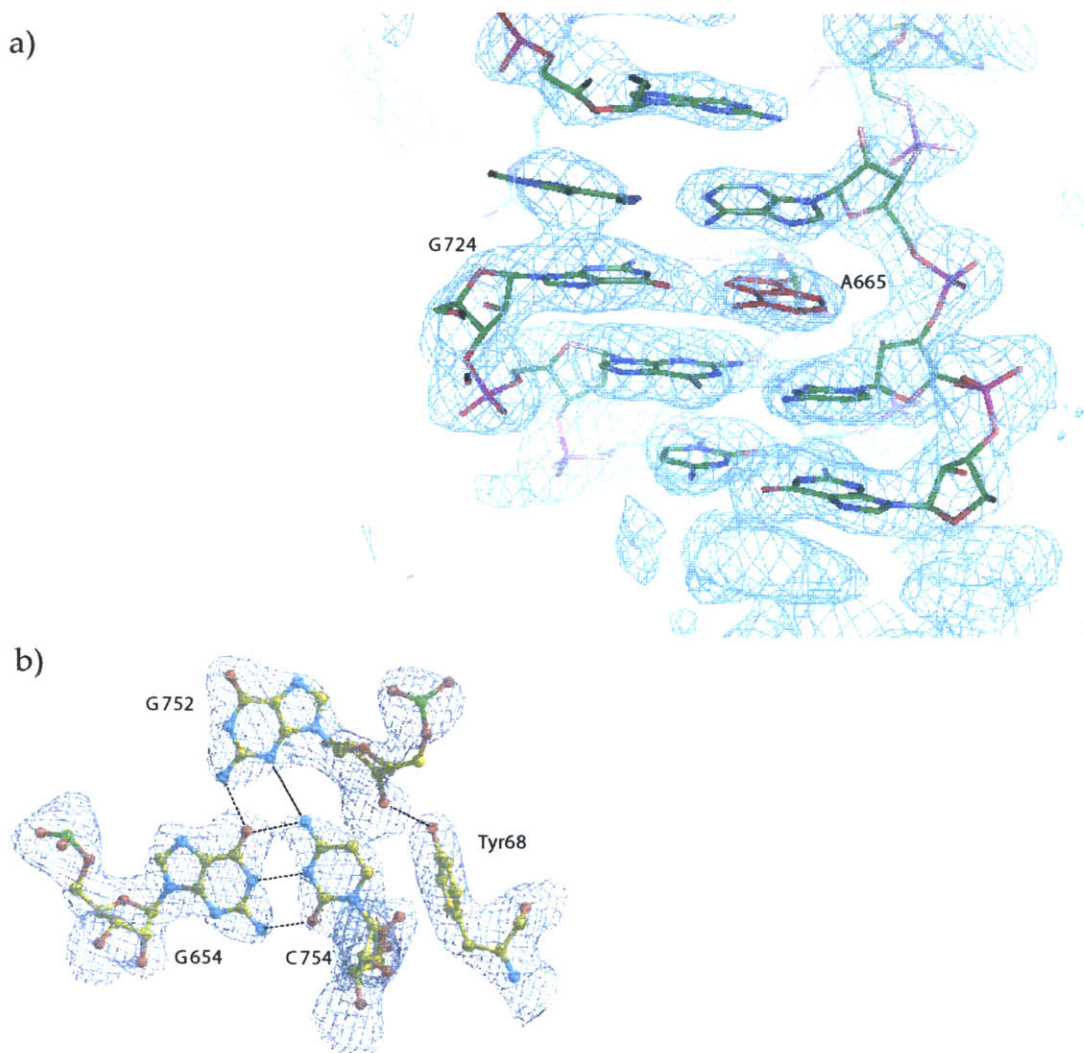


Figure 2.6 *Sample electron density maps.* a) Electron density is shown for the G654:G752:G754 base-triple in the helix 20, helix 21, helix 22 rRNA junction. We initially had difficulty assigning the proper rotation of the C754 base. b) Electron density is shown for the A665:G724 interhelical base pair between helix 22 and helix 23a.

et. al., 2000). Residues with no density were deleted, residues with visible density were retained, and short portions of the model were placed in proper register. The R_{free} remained unchanged at 29.8 %, while the R_{cryst} improved from 26.6 % to 25.4%.

2.4 The T4 RNP structure

The T4 RNP complex has a unique structure (Figure 2.7). The 120 nucleotide rRNA folds into two three-helix junctions at opposite ends of helix 22. The helix 20, helix 21, helix 22 junction contains a reverse Hoogsteen base pair and a novel base triple. The helix 22, helix 23, helix 23a junction adopts a unique structure containing an interhelical base pair. The protein S15 binds the RNA and spans both junctions. The proteins S6 and S18 form a heterodimer and bind across the upper three helix junction. The distal portion of Helix 23 shows poor electron density and the complete structure could not be built. Similarly, protein S18 could only be modeled for regions of strong electron density. The two structures in the asymmetrical unit were quite similar and showed only minor differences.

The S15 protein is a highly basic four helix bundle which binds the T4 RNA across both three-helix junctions (Figure 2.8). The 88 amino acid protein contains 14 lysine and seven arginine residues, and folds into four α -helices connected by three short loops. There are at least five novel high resolution S15 structures. Two structures are of the free protein: S15 NMR (PDB id 1AB3, Berglund, *et al.*, 1997), and S15 X-ray (PDB id 1A32, Clemons, Jr., *et al.*, 1998). The other three structures are of S15 bound in RNPs: S15:rRNA binary complex (PDB id 1DK1, Nikulin, *et al.*, 2000), S15 in quaternary T4 RNP (PDB id 1G1X, Agalarov, *et al.*, 2000), and S15 in 30S ribosome structure (PDB id 1J5E, *et al.*, Wimberley, 2000). The T4 RNP S15 structure is similar to the free-protein NMR structure, to the structure bound to a minimal RNA binding site, and to the structure found in the 30S particle. The RMSD with the NMR structure is 3.4 Å. The free-protein X-ray structure is slightly different from the T4 RNP S15 structure, with the first α -helix of S15 in the crystal structure extended away from the core of the protein. The overall RMSD between our T4 S15 and the free-protein crystal structure is quite large at 80.4 Å, but the RMSD of the core of the protein excluding the first α -helix is 3.3 Å.

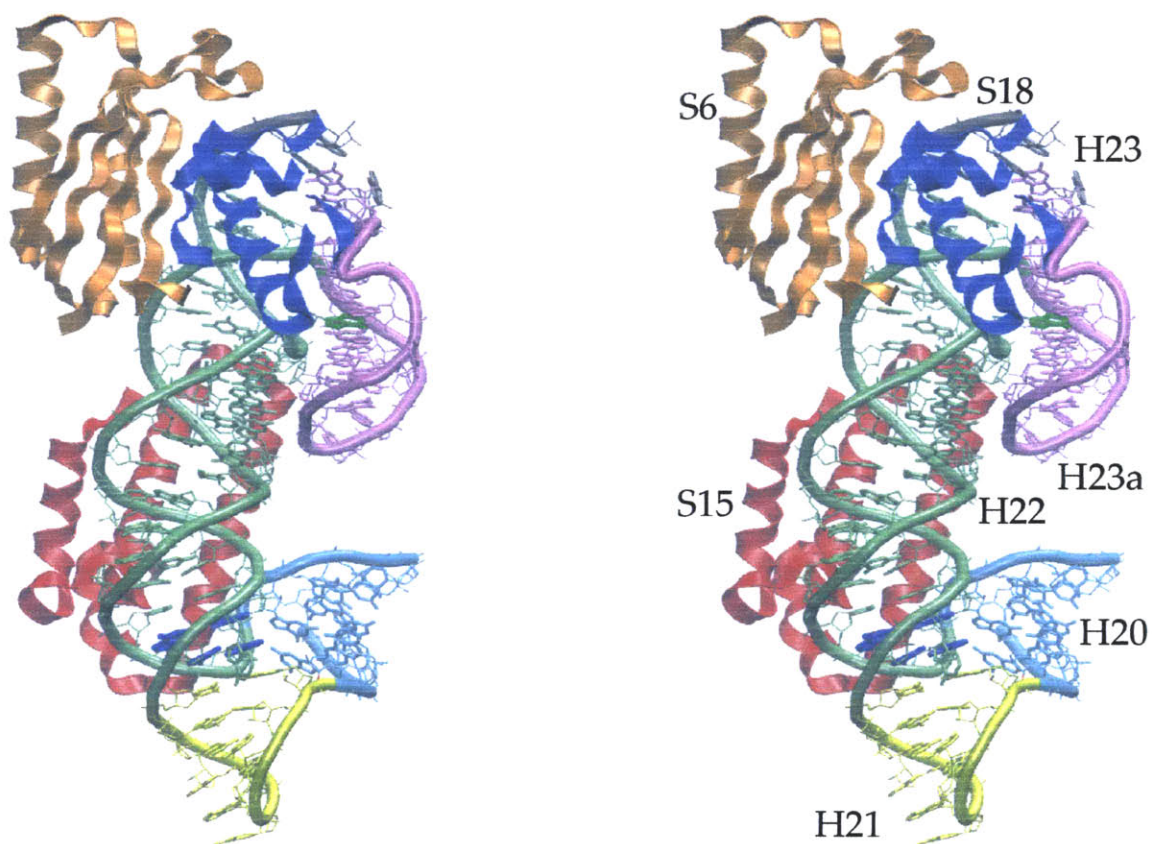


Figure 2.7 *Cross-eyed stereogram of the *T.th* X-ray crystal structure.* The rRNA from the 30S central domain contains portions from helix 20 (light blue), helix 21 (yellow), helix 22 (light green), helix 23 (grey), and helix 23a (light purple). The ribosomal protein S15 (red) binds across the helix 20, helix 21, helix 22 RNA junction. The proteins S6 (orange) and S18 (dark blue) form a heterodimer and bind across the helix 22, helix 23, helix 23a RNA junction. Portions of helix 23a RNA showed no electron density and were not modeled, as were portions of S18, including the 30 N-terminal residues and a few other residues in the core.

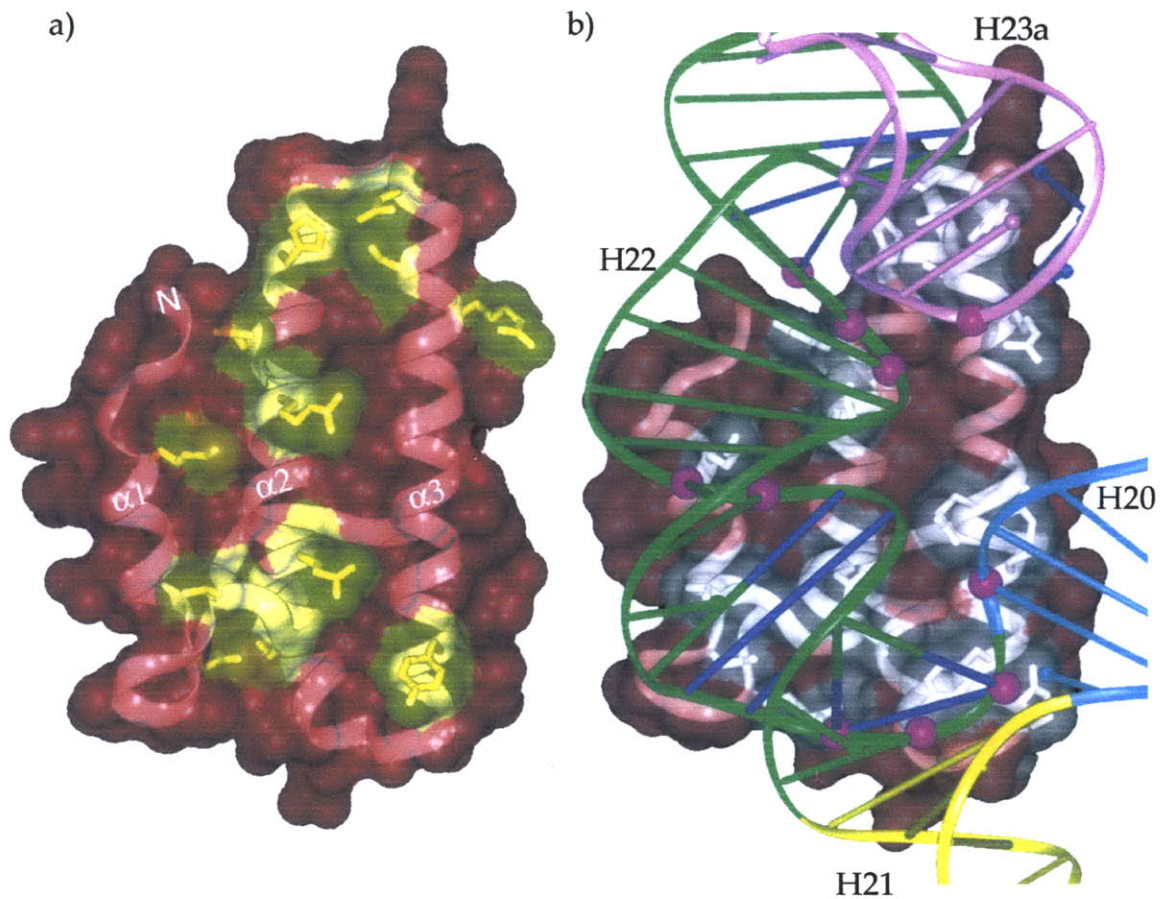


Figure 2.8 *S15 in the T4 RNP* a) Ribbon and transparent space filling representation of protein S15. Positive residues (yellow) on one side of the four α -helical bundle line the RNA binding face. b) The S15 protein makes four sets of contacts to the T4 RNA: across the folded helix 20, helix 21, helix 22 junction, to two backbone phosphates along helix 22, to the helix 22 purine-rich loop, and to the folded helix 23a tetraloop. S15 contacts to phosphates in the RNA backbone are shown as purple spheres, and contacts to either bases or sugars are shown in dark blue.

The S15 protein interacts with the T4 rRNA in four places: across the folded helix 20, helix 21, helix 22 junction, to two backbone phosphates along helix 22, to the helix 22 purine-rich loop, and to the folded helix 23a tetraloop (Figure 2.8b). S15 residue Tyr 68 from α -helix 4 interacts with the helix 20, helix 21, helix 22 RNA junction at the G654:G752:C754 base-triple (Figure 2.9). S15 residues Asp20, Thr21, Gly22, Thr24, and Gln27 in the loop connecting α -helix 1 and α -helix 2 interact with RNA minor groove residues adjacent the junction in helix 22. Several S15 residues in the loop between α -helix 2 and α -helix 3 interact with the highly conserved purine-rich loop in the rRNA Helix 22 (Figure 2.10). S15 residues His41, His45, Asp48, and Ser51 make close contacts to base and ribose moieties in the RNA minor groove. The groove is widened by non Watson-Crick base pairing and by the conformation of the extrahelical residue A665, which makes a base pair with G724 in helix 23a. The S15 residues His50 and Arg53 located in α -helix 3 interact with the GAAG rRNA tetraloop in helix 23a (Figure 2.11). The indole group of His50 is a few Angstroms from the bases on residues A728, A729, and G730, potentially participating in hydrogen bonding interactions. The guanidinium group of Arg53 is 'stacked' near A728, perhaps making both hydrophobic and ionic interactions.

The 102 amino acid ribosomal protein S6 folds into a compact structure, a four-stranded β -sheet buttressed by two α -helices (Figure 2.12a). The protein binds the ribosomal protein S18 along the face of the β -sheet and makes RNA contacts along one side of the β -sheet and along one α -helix. This S6 structure is remarkably similar to the free protein X-ray structure (Lindahl, et al., 1994), with an RMSD between the two structures of 2.1 Å. The only minor difference is conformation of a loop region that makes close contacts to S18, presumably upon heterodimerization.

The ribosomal protein S18 contains a mixture of α -helix and random coil structure (Figure 2.12a). Neither a free S18 X-ray crystal structure or solution NMR structure exist, and the model building was particularly difficult. Only similar structures are found in whole 30S ribosome subunits. Electron density was weak or absent for the first 30 amino acid residues, a portion in the middle of the protein, and the last five to ten residues; we had

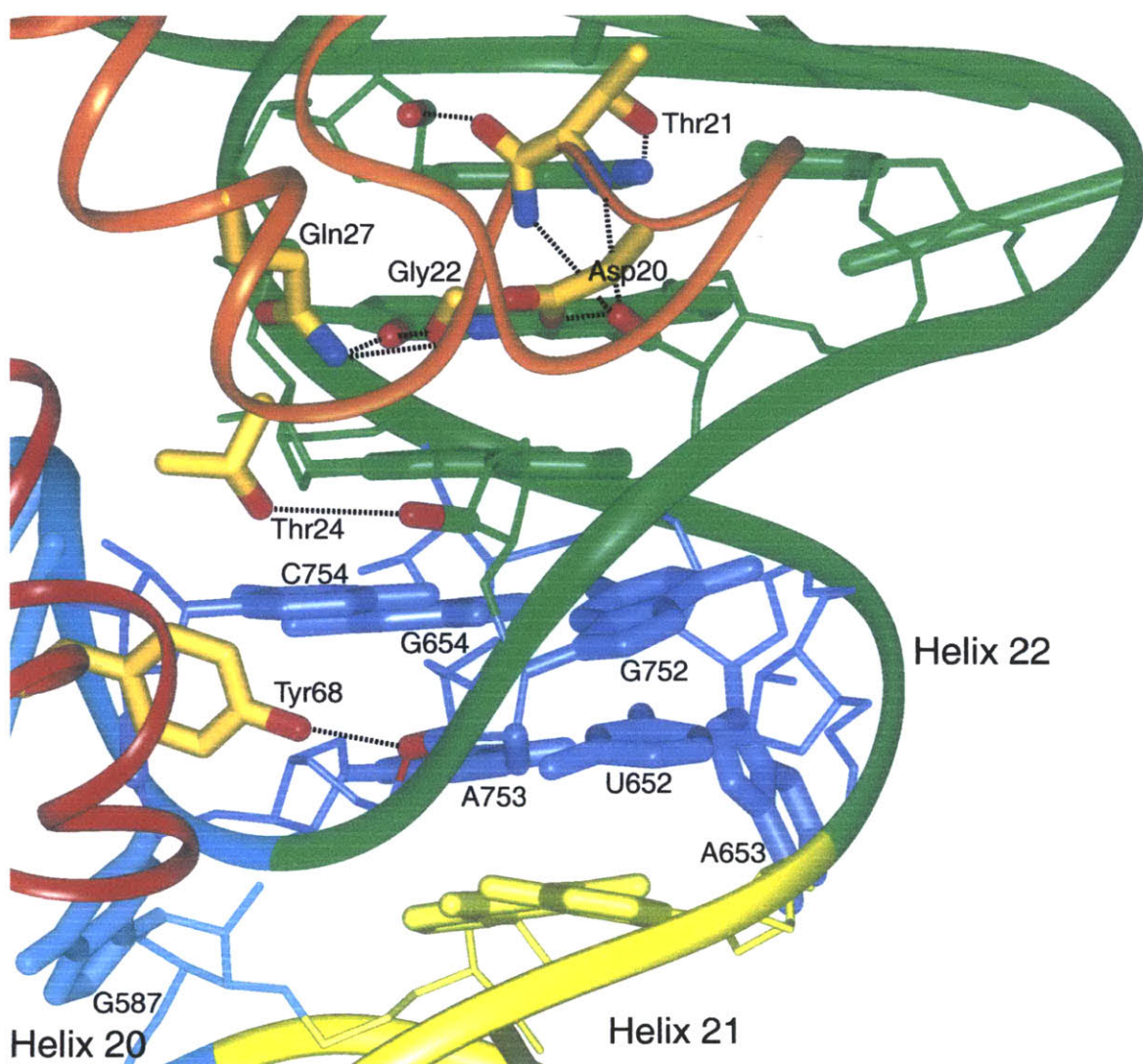


Figure 2.9 *S15 interactions with the helix 20, helix 21, helix 22 rRNA junction.* S15 residue Tyr68 from α -helix 4 makes close contacts with the rRNA junction (dark blue residues). S15 residues Asp20, Thr21, Gly22, Thr24, and Gln27 in the loop connecting α -helix 1 and α -helix 2 (orange ribbon) interact with RNA minor groove residues in H22 adjacent the RNA junction (green residues).

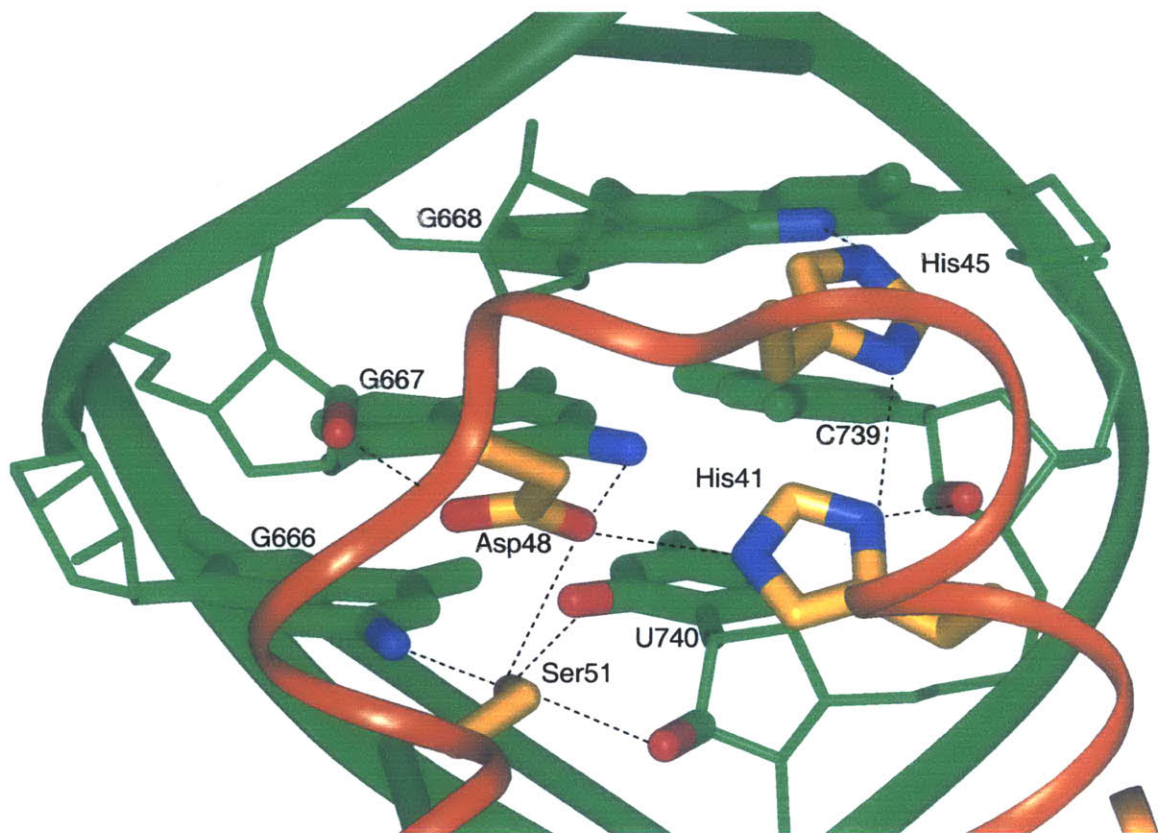


Figure 2.10 *S15-helix 22 rRNA interactions*. S15 residues His41, His45, Asp48, and Ser51 in the loop between α -helix 2 and α -helix 3 (orange ribbon) make close contacts to base and ribose moieties in the minor groove of rRNA helix 22 (green). This RNA minor groove is widened by non-Watson-Crick base pairing and the conformation of the nearby extrahelical A665 residue.

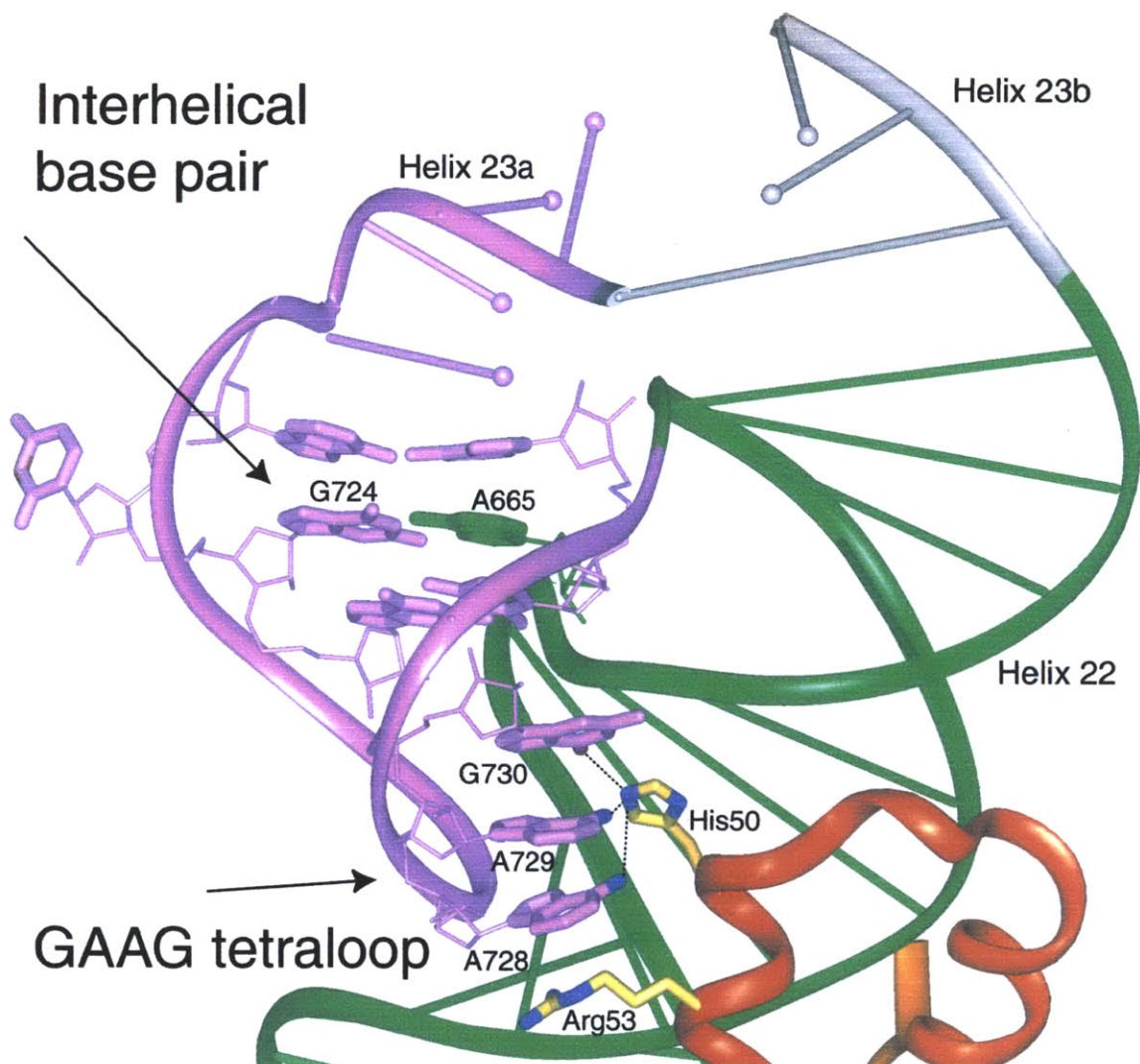


Figure 2.11 *S15-helix 23a RNA interaction*. The S15 residues His50 and Arg53, located in a-helix 3 (orange ribbon), interact with the GAAG rRNA tetraloop in helix 23a (lavender). The indole group of His50 is a few Angstroms from the bases on residues A728, A729, and G730, potentially participating in hydrogen bonding interactions. The guanidinium group of Arg 53 is stacked near A728, perhaps making both hydrophobic and ionic interactions.

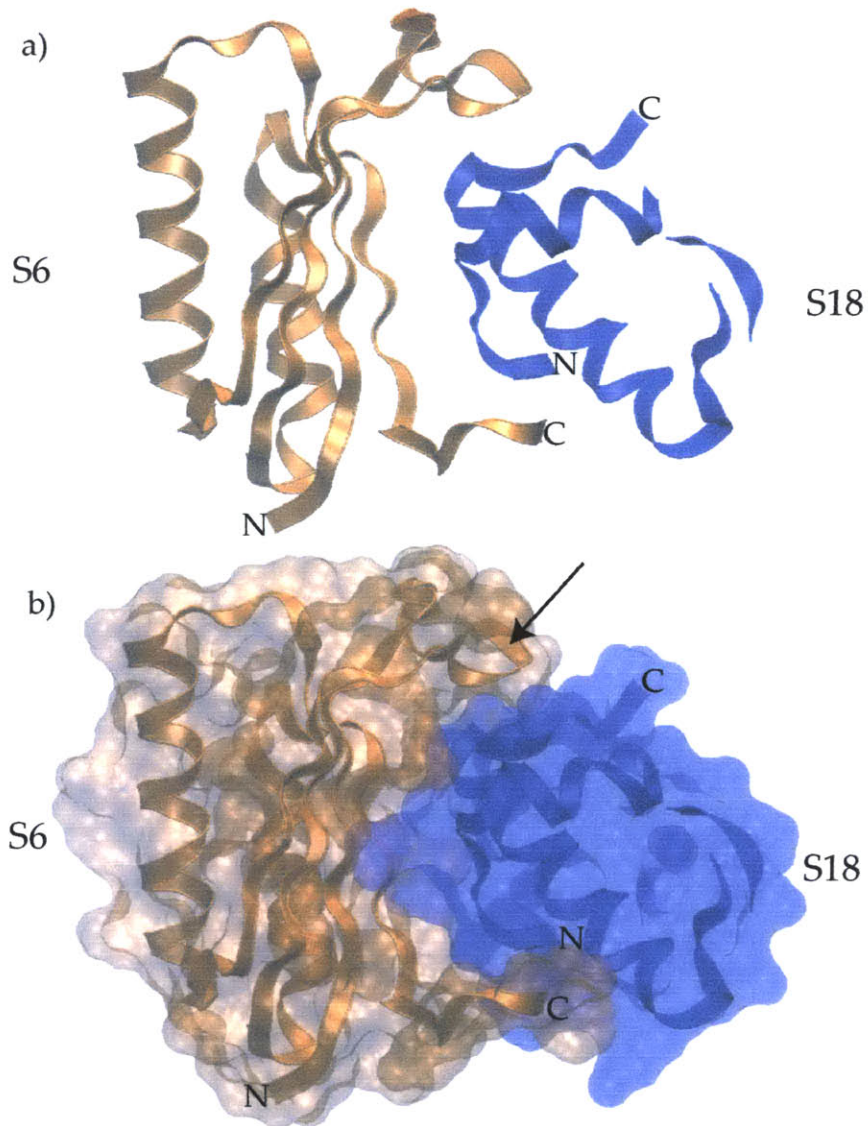


Figure 2.12 *Ribosomal protein S6 and S18.* a) Protein S6 (orange ribbon) contains a four-stranded β -sheet buttressed by two α -helices. Protein S18 (blue ribbon) is a mixture of α -helices and random coil. We were able to build only a portion of the T4-bound S18 due to weak or missing electron density at the N-terminus, in the middle, and near the C-terminus. Portions of S18 in the binding faces for S6 and the rRNA appear well structured. b) S6:S18 heterodimer (orange and blue space-filling model) reveals extensive hydrophobic and complementary electrostatic interactions along the binding interface. The small difference between the free S6 X-ray crystal structure and the T4 bound structure appears to be the folding of the loop region (arrow) onto S18 upon heterodimer formation.

great difficulty building this part of the model. Our initial deposition into the PDB was determined to be partially incorrect and we submitted a revised structure as described above.

Ribosomal proteins S6 and S18 heterodimerize along the beta sheet of S6 and across α -helix 2 and coil portion of S18 (Fig. 2.12b). The C-terminus and a loop from the larger S6 protein extend from opposite sides of the beta sheet, forming a pocket in which the S18 protein can bind. The structure of S6 in the T4 RNP is slightly different from the crystal structure of the free S6 protein. The loop containing S6 residue 50 folds around S18, analogous to a thumb in a hand shake. S18 binding appears to be a mixture of hydrophobic and specific ionic interactions.

The S6:S18 heterodimer binds the rRNA across the helix 22, helix 23, helix 23a junction (Figure 2.13). S6 residues on one edge of β -sheet and one side of an α -helix bind along the minor groove of Helix 22. Residues on S18 α -helix 3 span the entire upper rRNA junction, as if locking the RNA into a folded conformation. Positively charged S18 residues Arg64, Lys68, Lys71, and Arg72 all make close contacts to RNA phosphate groups, and Lys71 and Arg74 make close contacts to Watson-Crick faces of RNA bases in the 16S Helix 23a loop.

2.5 Discussion.

The T4 RNP structure provided a fascinating first look at a multiprotein RNP from the core of the 30S ribosomal subunit central domain. The structure confirmed many previous biochemical details about S15 interaction with the rRNA, and provided insight into a mechanistic understanding of ordered 30S assembly of *in vitro*, as first demonstrated by Nomura in the late 1960s. Previous biochemical studies using chemical probing and hydroxy radical footprinting had shown protein S15 interacts primarily with helix 22, helix 23, and helix 23a of 16S rRNA (Svensson, *et al.*, 1988; Powers and Noller, 1995). Batey and Williamson determined protein S15 can bind a series of minimal rRNA consisting of only the helix 20, helix 21, helix 22 RNA junction and a portion of helix 22 containing a purine rich internal loop (Batey and Williamson, 1996a). These minimal fragments

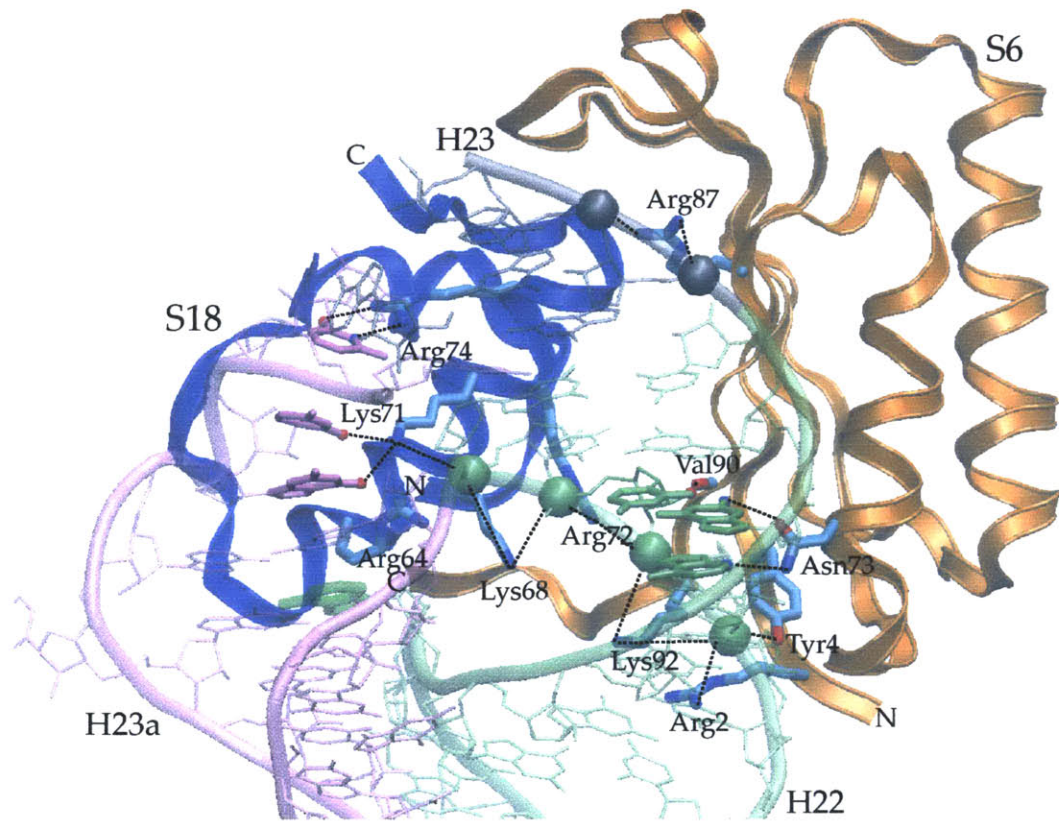


Figure 2.13 *S6:S18 interaction with T4 rRNA*. The protein heterodimer binds across the helix 22, helix 23, helix 23a junction. Charged residues on one side of protein S6 contact the RNA backbone in the minor groove at the transition from helix 22 to helix 23. Positively charged residues in S18 span the entire RNA junction.

bind with apparent wild-type affinity and do not require helix 23 or helix 23a for specific protein binding. Our T4 crystal structure is consistent with these findings, and confirms the determinants of specificity for S15 binding in the minor groove side of helix 22 rRNA near the helix 20, helix 21, helix 22 junction and in the purine rich loop.

Our structure also shows interesting contacts between S15 and the helix 23a GAAG tetraloop, and an unexpected interhelical base pair between helix 22 and helix 23a. It is primarily these contacts that led to our initial structural model of 30S central domain assembly, in which protein S15 binding promotes the proper folding of the helix 22, helix 23, helix 23a junction for S6:S18 binding in the absence of any direct protein-protein contacts between S15 and the S6:S18 heterodimer (Fig. 2.14). In our model proteins S8 and S15 can both bind the helix 20, helix 21, helix 22 junction early in central domain assembly, but only protein S15 can stabilize the proper fold of the helix 22, helix 23, helix 23a junction necessary for binding the S6:S18 heterodimer. This notion is consistent with experiments that show enhanced chemical sensitivity of RNA nucleotides upon binding S15, and subsequent protection upon binding the S6:S18 heterodimer (Svensson, *et al.*, 1988). The rest of the central domain, including helix 24, helix 25, and helix 26, may then fold onto this 'core' of the central domain. This preliminary assembly model based on insight gleaned from the T4 particle would be extended as more information became available.

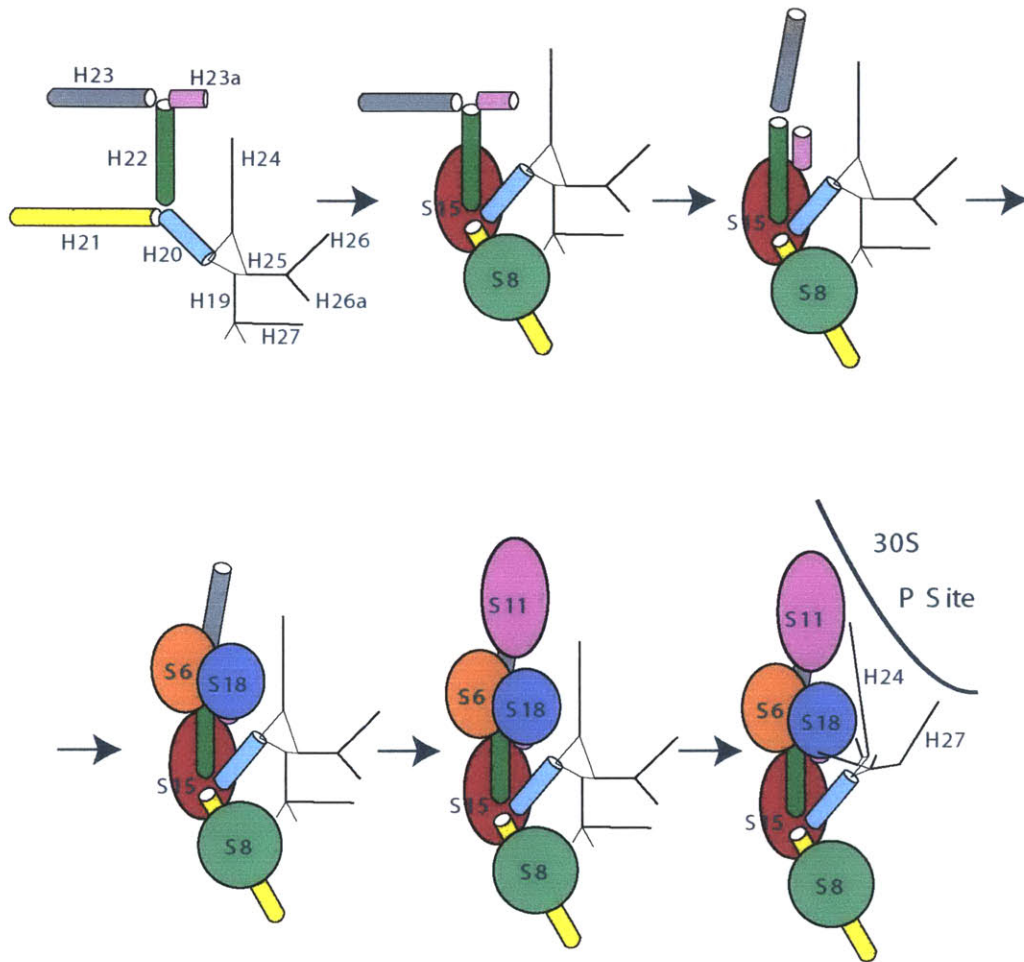


Figure 2.14 *Model of 30S central domain ordered assembly.* Early binding of proteins S15 and S8 stabilize the folding of the helix 20, helix 21, helix 22 junction. Subsequent stabilization of the helix 22, helix 23, helix 23a junction by protein S15 creates the binding site for the heterodimer S6:S18. Subsequent assembly steps involve binding of protein S11 and folding of the rest of the central domain rRNA onto this preformed 'core' structure to form a functional central domain within the 30S ribosomal subunit.

Chapter 3: Investigation of conformational changes in fragments of *B. stearothermophilus* 16S rRNA monitored by fluorescence spectroscopy

3.1 Introduction

Assembly of complete 30S ribosome subunits involves many discrete events of RNA folding and protein binding. Amazingly, the 1542 nucleotide 16S rRNA folds into three compact subdomains and binds 20 proteins in the absence of any cofactors *in vitro* (Traub and Nomura, 1968). We are interested in investigating the influence protein S15 and divalent cations on structural changes in fragments of 16S central domain rRNA to better understand the sequential nature of 30S ribosome assembly (Figure 1.5).

The RNA binding site for S15 was localized to a portion of the 16S rRNA central domain (Mougel et al, 1998; Muller et al., 1979; Powers and Noller, 1995), and a minimal binding site was determined using a series of sequential deletions of the RNA in a electrophoretic mobility shift assay (Batey and Williamson, 1996a). Enhanced electrophoretic mobility of these minimal rRNAs in the presence of various cations and S15 protein implied a reorganization of the RNA three-helix junction into a more compact shape (Batey and Williamson, 1998). Further investigation of this rRNA three-helix junction using transient electric birefringence (TEB) allowed for more detailed modeling of the conformational change (Orr et al., 1998). The measured tumbling rates of a series of RNAs constructed with ~70 base pair extensions on the three helices in the presence of salts and S15 protein were used to calculate the molecules moments of inertia, from which the conformation of the three helix junction was modeled. In the unfolded state the RNA helices were reported to be essentially planar, and each extended at 120 degrees; in the folded state helices 20 and 21 stack coaxially and helices 20 and 22 form a 60 degree angle.

rRNA conformational changes were also investigated by single molecule fluorescence methods. Biotinylated RNAs labeled with fluorescent dyes were attached to a substrate and fluorescence efficiency was observed as a probe for RNA folding upon addition of protein or magnesium (Ha, *et al.*, 1999). The measured bimolecular equilibrium dissocia-

tion constant (K_d) and dissociation rate constant (k_{off}) were in agreement with previously measured values (Batey and Williamson, 1998). Fluorescence correlation spectroscopy (FCS) methods were also used to develop a more detailed model of magnesium-stabilized RNA conformational change, in which one can not discriminate between metal binding before or after the RNA conformational change (Kim, et al., 2002).

Here we use time-resolved fluorescence resonance energy transfer (trFRET) methods to monitor the conformational changes in the rRNA binding site for protein S15. We add fluorescent dyes pair-wise around a tripartite helix 20, helix 21, helix 22 RNA binding site for S15 and directly monitor the conformational changes stabilized by magnesium and S15. We also use trFRET to look for magnesium-stabilized conformational change in a helix 22, helix 23, helix 23a junction. We also use single-pair fluorescence resonance energy transfer (spFRET) methods to observe conformational subpopulations of individual RNAs free in solution. These preliminary results with freely diffusing molecules confirm previous findings with surface-immobilized RNAs and show that single-molecule methods can bridge our understanding of ensemble behavior. We incorporate these results into a more complete model of the formation of the T4 RNP, and by extension to the 30S central domain core, and gain greater insight into the sequential nature of S6:S18 binding.

3.2 Time-resolved fluorescence resonance energy transfer (trFRET) as a method to measure distances in large biomolecules

The distance between two different fluorescent dyes site-specifically bound to a macromolecule can be determined by calculating the rate of energy transfer between the dyes in a two step process (Yang and Millar, 1996; Klostermeier and Millar, 2002). First, the lifetimes of a single donor fluorophore are calculated from the observed fluorescence decay using an ultrafast pulse laser and time-resolved detection methods. Then the lifetimes of the donor fluorophore are measured in the presence of an acceptor fluorophore, and the difference between the lifetimes are related to the rate of energy transfer, which is directly related to the distance between fluorophores.

The fluorescence decay of the donor can be modelled empirically as a sum of exponentials

$$I_D(t) = \sum_i \alpha_i \exp\left(-\frac{t}{\tau_i}\right)$$

where α_i are the amplitudes and τ_i are the lifetime of the i th exponentials, and the i sub-states represent different micro environments of the donor fluorophore.

The real fluorescence decay is complicated by the instrument itself, which adds a small component to the beginning of the observation. This instrument response function (IRF) is measured separately by passing the exciting laser pulse through a dilute particulate solution and measuring the scattered light. The real fluorescence lifetimes and amplitudes are extracted by convolving the IRF with test lifetime and amplitude values, then iteratively comparing this combination with the experimental data by non-linear least squares fitting until convergence.

$$I_{Obs}(t) = irf \otimes I_D(t)$$

The extracted lifetimes and amplitudes of the donor-only fluorescence sample are then compared to the observed decay of the donor-acceptor fluorescence decay using the formula below,

$$I(t) = \sum_k \alpha_k \sum_i \alpha_i \int p_k(r) \exp\left[-\frac{t}{\tau_i} \left(1 + \left(\frac{R_0}{r}\right)\right)\right] dr$$

where R_0 is the mean distance of energy transfer for the dye pair, and the distance distribution p_k is a weighted gaussian distribution of distances. This model was evaluated assuming either a single distance, or assuming two separate distances. In this case the equation was fit with relative weights p_1 and p_2 and mean distances R_1 and R_2 . The goodness of fit was determined by the reduced chi-square value, χ^2 , and by appearance of the weighted residuals.

Our experimental strategy to measure conformational changes of the two three helix junctions at the ends of helix 22 in 16S ribosomal RNA is to attach a donor fluorophore dye to the 5' end of any available helix and measure the observed donor-only fluorescence decay. We then attach an acceptor dye to any other free 5' helix end and observe the change in the donor fluorescence in the presence of acceptor, and use the equation above to determine the distance between the dyes.

3.3 Distance measurements in a linear duplex RNA molecule

A 23 base pair duplex RNA was used to calibrate the trFRET method for our fluorescein-tetramethylrhodamine dye pair. A 1 μ M donor-only RNA sample was prepared by annealing two complementary oligonucleotides, one with a single fluorescein moiety attached to the 5' end by a flexible six-carbon linker (Fig. 3.1). The samples were prepared in a low salt buffer (10 mM Hepes pH 6.5, 100 mM NaCl) and illuminated at by a femtosecond laser in the absence or presence of 3000 μ M magnesium chloride. The decay data were collected perpendicular to the excitation and fit to a model with either two or three exponentials. In both instances the model with three exponentials fit the data better, yielding significantly lower χ^2 values and better appearance of the residuals.

A donor-acceptor duplex RNA was similarly prepared with fluorescein and tetramethylrhodamine fluorophores attached to the 5' ends of the complementary oligonucleotides (Fig. 3.2). The fluorescein fluorescence decay was again measured in the absence and presence of 3000 μ M magnesium chloride, and these data were fit to the energy transfer model using the time constants extracted from the donor-only experiment, and either one

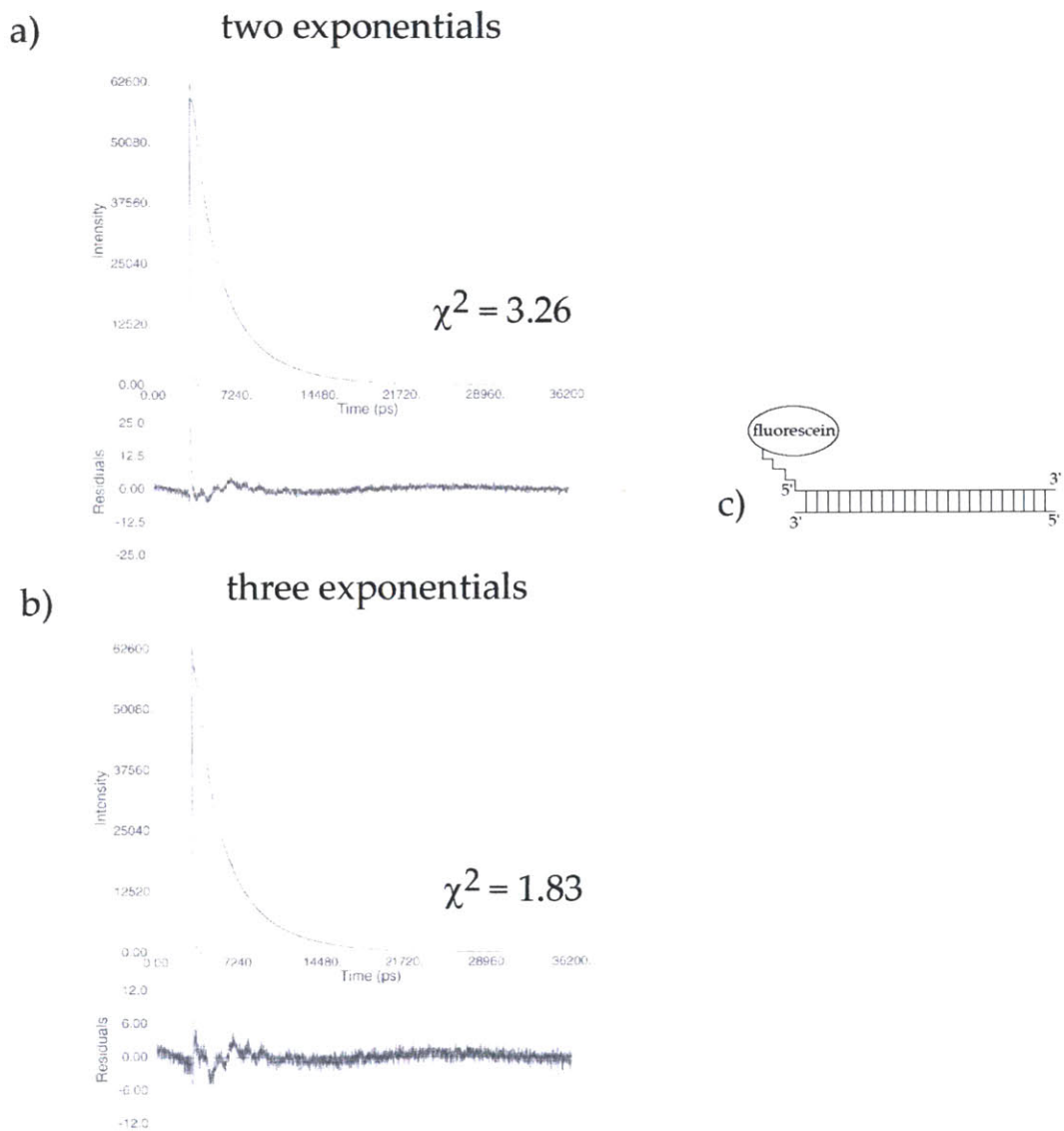


Figure 3.1 *Linear Control RNA Donor-only Fluorescence Decay*. a) Fluorescein fluorescence decay of the linear duplex RNA fit to a model with two separate exponential time constants has a high χ^2 value of 3.26. Significant deviations appear in the residual differences between the fit and the data at the beginning of the fluorescence decay near the instrument response function. b) Donor-only fluorescein fluorescence decay fit to three different exponentials has a χ^2 value of 1.83. The residual differences between the fit and the data show better significantly better agreement, especially at the beginning of the fluorescence decay. c) Cartoon representation of the 23 base pair helix 20-helix 21 linear control RNA with fluorescein dye attached by a six carbon linker to the 5' end of the helix 21 end.

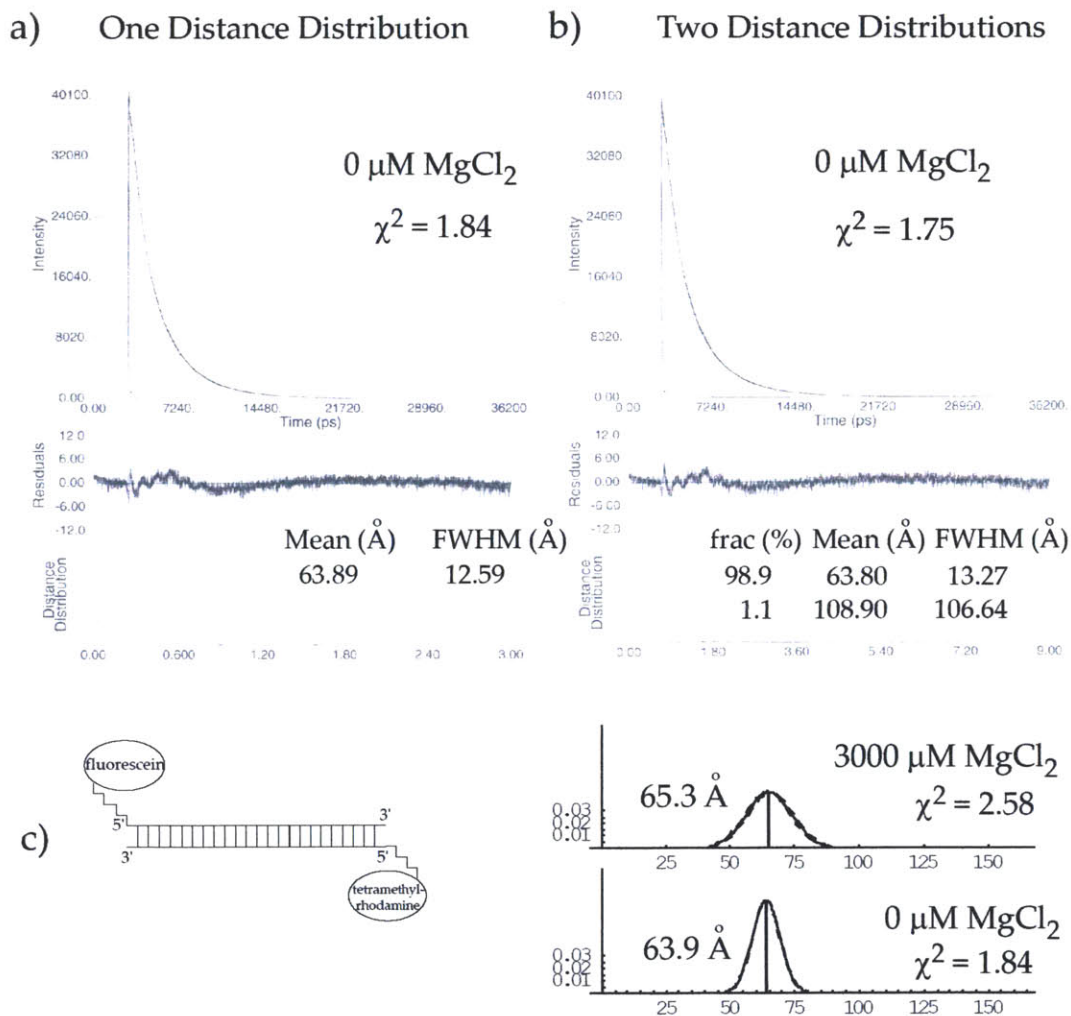


Figure 3.2 Linear Control RNA Distance Measurement. a) Fluorescence decay of the donor-acceptor duplex RNA at low MgCl_2 fit to a model with one distance distribution, including χ^2 value, mean distance, and full width at half max (FWHM). b) Fluorescence decay of the linear RNA fit to a model with two different distance distributions. has a lower χ^2 value of 1.75; however the small fraction and impossibly long distance of the second distance distribution indicate this is not a real improvement to the fit with only one distance distribution. c) Cartoon representation of the 23 base pair linear control RNA, and trFRET results at both $0 \mu\text{M MgCl}_2$ and $3000 \mu\text{M MgCl}_2$. The mean distances are quite similar and confirm our assumptions that the linear RNA does not undergo a substantial conformational change upon addition of MgCl_2 .

or two discrete distances. At low salt ($0 \mu\text{M Mg}^{++}$) a single distance distribution fit the data reasonably well ($\chi^2 = 1.84$) and returned a mean distance of 63.9 \AA , very near the 64.4 \AA distance calculated from known duplex A-form RNA geometry. The fit to a model with a second distance distribution was slightly better ($\chi^2 = 1.75$); however the second distribution was only 1.1 % and the mean distance was impossibly long at 108.9 \AA . At high salt ($3000 \mu\text{M Mg}^{++}$) a single distance distribution fit the data ok ($\chi^2 = 2.57$) and returned a mean distance of 65.3 \AA , also close to our calculated value. The addition of a second distance distribution did not improve the fit. These results gave us confidence in our method.

3.4 Magnesium-stabilized conformational change in the helix 20, helix 21, helix 22 junction of 16S rRNA

The helix 20, helix 21, helix 22 rRNA junction has been shown to undergo a conformational change upon addition of cations, in particular magnesium, using a variety of different methods (Batey and Williamson; 1998, Orr, *et al.*, 1998; Ha, *et al.*, 1999). Here we use trFRET to directly monitor these changes to gain greater insight into assembly of the T4 particle.

Three separate donor-only RNA samples were prepared by annealing a single fluorescein-labeled oligonucleotide with a small excess of two unlabeled nucleotides in a low salt buffer (10 mM Hepes pH 6.5, 100 mM NaCl). Each donor-only RNA sample was illuminated by a femtosecond laser, and magnesium chloride was titrated from $0 \mu\text{M}$ to $3000 \mu\text{M}$. The fluorescence decay data were measured and fit to a model with either two or three exponentials. In each case a model with three exponentials fit the data better than two exponentials based on both lower χ^2 values quality of appearance of the residuals. These values were used later in the energy transfer calculations.

Six separate donor-acceptor rRNA samples were prepared with each permutation of the fluorescein-tetramethylrhodamine dye-pair to measure the distance in each direction between any two of the three helices. These RNAs were prepared by annealing the 5' flu-

orescein-labeled oligonucleotide in a small excess of the 5' tetramethylrhodamine-labeled oligonucleotide and an unlabeled oligonucleotide in the low salt buffer (10 mM Hepes pH 6.5, 100 mM NaCl). The samples were illuminated by a femtosecond laser and the fluorescein fluorescence decay data was collected as magnesium chloride was titrated from 0 μM to 3000 μM . These data were fit to the energy transfer model using the lifetimes extracted from the donor-only experiments. The model was tested with both one distance distribution and two different distance distributions and the quality of the fit compared.

The averaged bi-directional distance calculations around the helix 20, helix 21, helix 22 junction upon magnesium chloride titration using an energy transfer model with a single distance distribution are shown below (Fig. 3.3, Fig. 3.4). These results indicate the distance between helix 20 and helix 21 remains essentially unchanged, as does the distance between helix 21 and helix 22. Only the distance between helix 20 and helix 22 undergoes a significant change upon addition of magnesium chloride.

The directional energy transfer results between helix 20 and helix 21 are shown below using a model with a single distance distribution (Figure 3.5). At each magnesium concentration a single distance distribution fit the data reasonably well and returned a mean distances ranging from 58 \AA at low magnesium to 60 \AA at high magnesium. In each case the addition of a second distance distribution resulted in lower χ^2 values; however these second distance distributions had mean values between 78 \AA and 158 \AA , significantly longer than physically possible in this RNA construct. In these instance we conclude an energy transfer model with two distance distributions does not describe the data better than a model with a single distance distribution.

The energy transfer results in the opposite direction from helix 21 to helix 20 are slightly more nuanced. At lower magnesium chloride concentration (0 μM , 30 μM , 100 μM) a model with two distance distributions gives a slightly better fit to the data based on χ^2 values, and the mean distances between 55 \AA and 68 \AA are physically reasonable. At higher magnesium chloride concentrations above the previously reported K_d values for magnesium (Ha, *et al.*, 1999), the model with a single distance distribution fits the data better

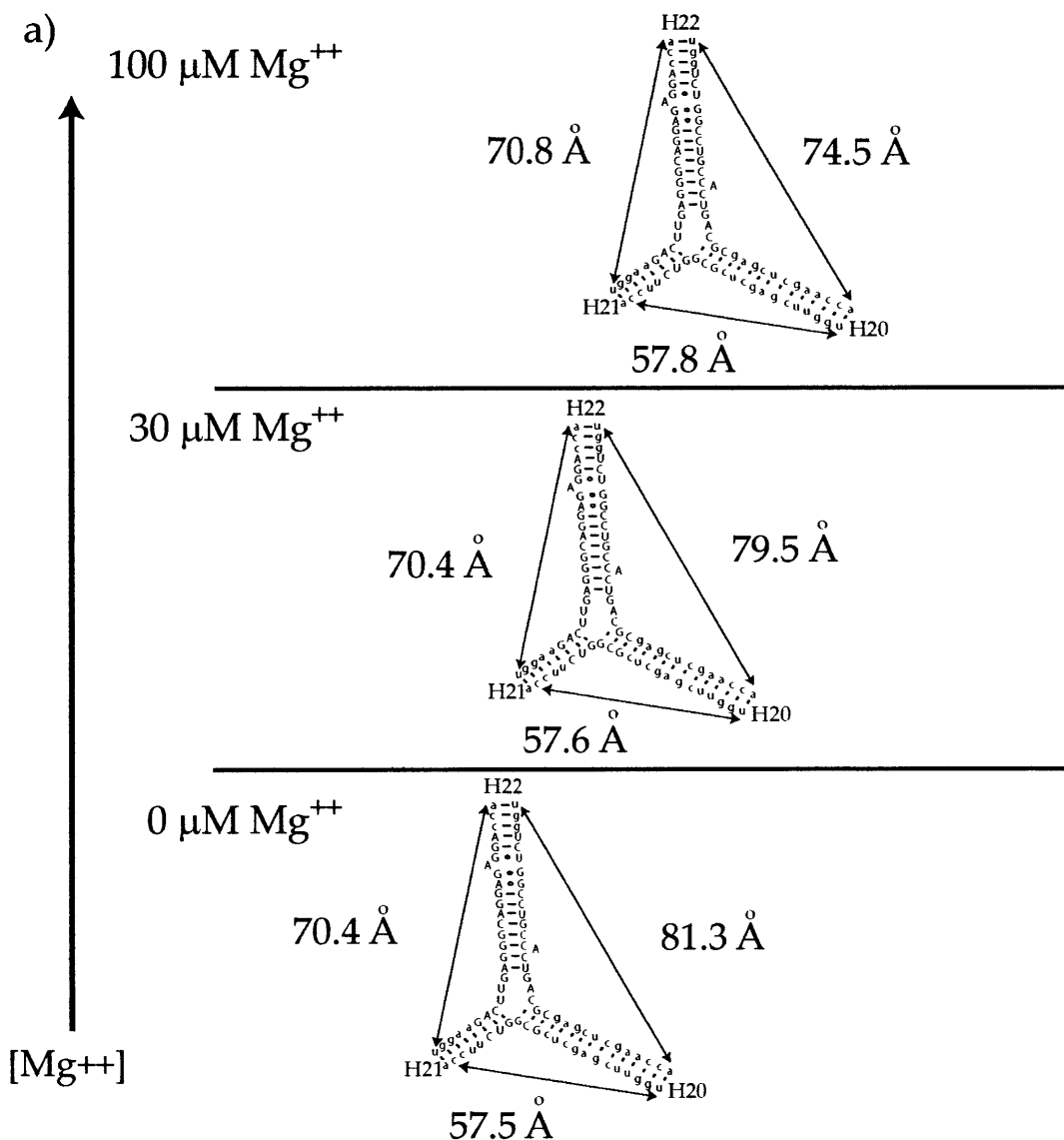


Figure 3.3 *trFRET* results for the helix 20, helix 21, helix 22 rRNA junction upon magnesium chloride titration. This figure shows results for the first half of the magnesium chloride titration from 0 μM to 100 μM . Distances are calculated using an energy transfer model with a single distance. The reported distance is an average of the energy transfer in both directions between helices. At 100 μM magnesium chloride the helix 20-helix 22 distance begins to decrease, while the other distances remain essentially unchanged.

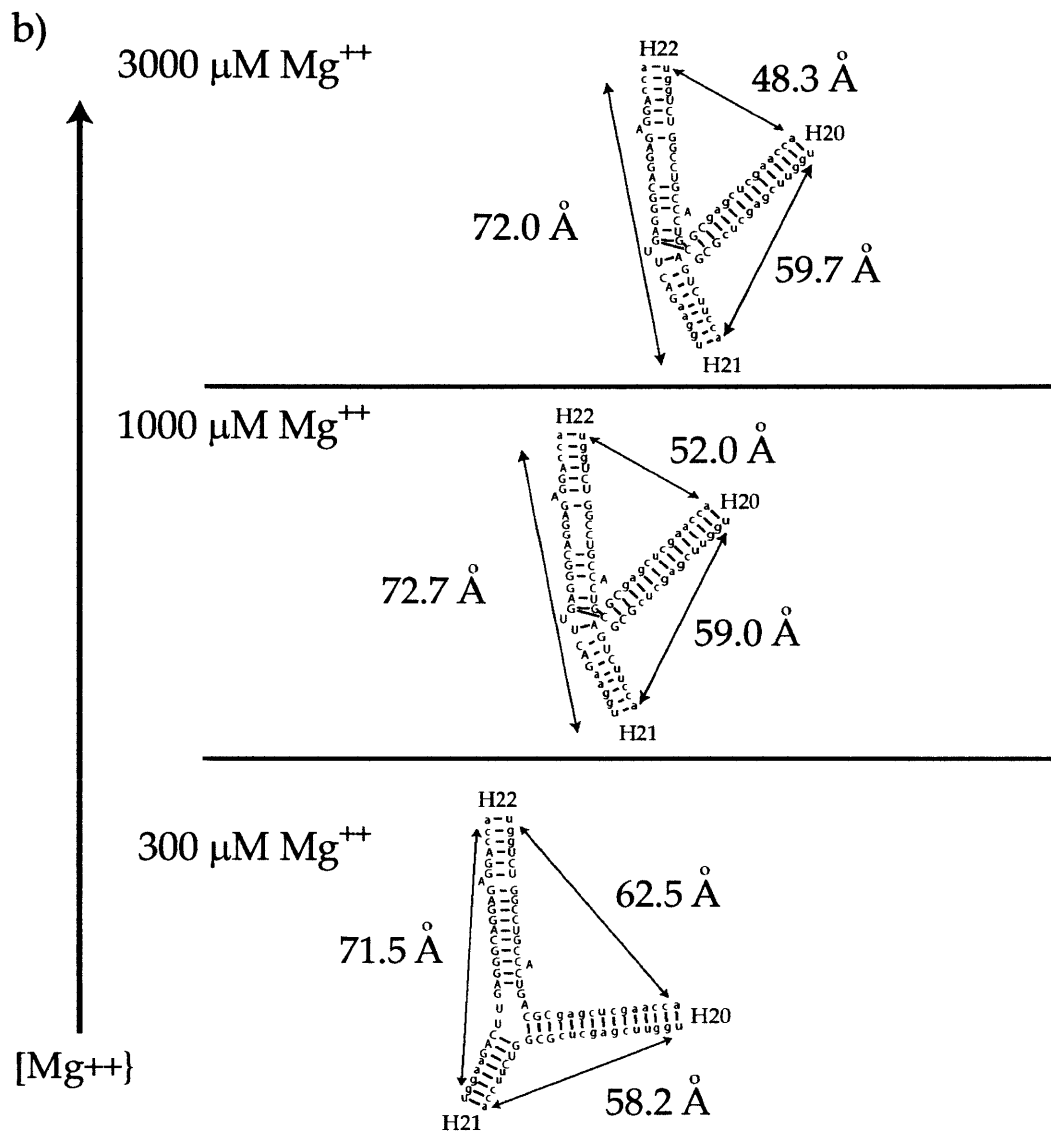


Figure 3.4 *trFRET* results for the helix 20, helix 21, helix 22 rRNA junction upon magnesium chloride titration. This figure shows results for the second half of the magnesium chloride titration from 300 μM to 3000 μM . Distances are calculated using an energy transfer model with a single distance. The reported mean distances are an average of the energy transfer in both directions between helices. As the magnesium chloride concentration increases the helix 20-helix 22 distance continues to decrease, while the other distances show only minor changes.

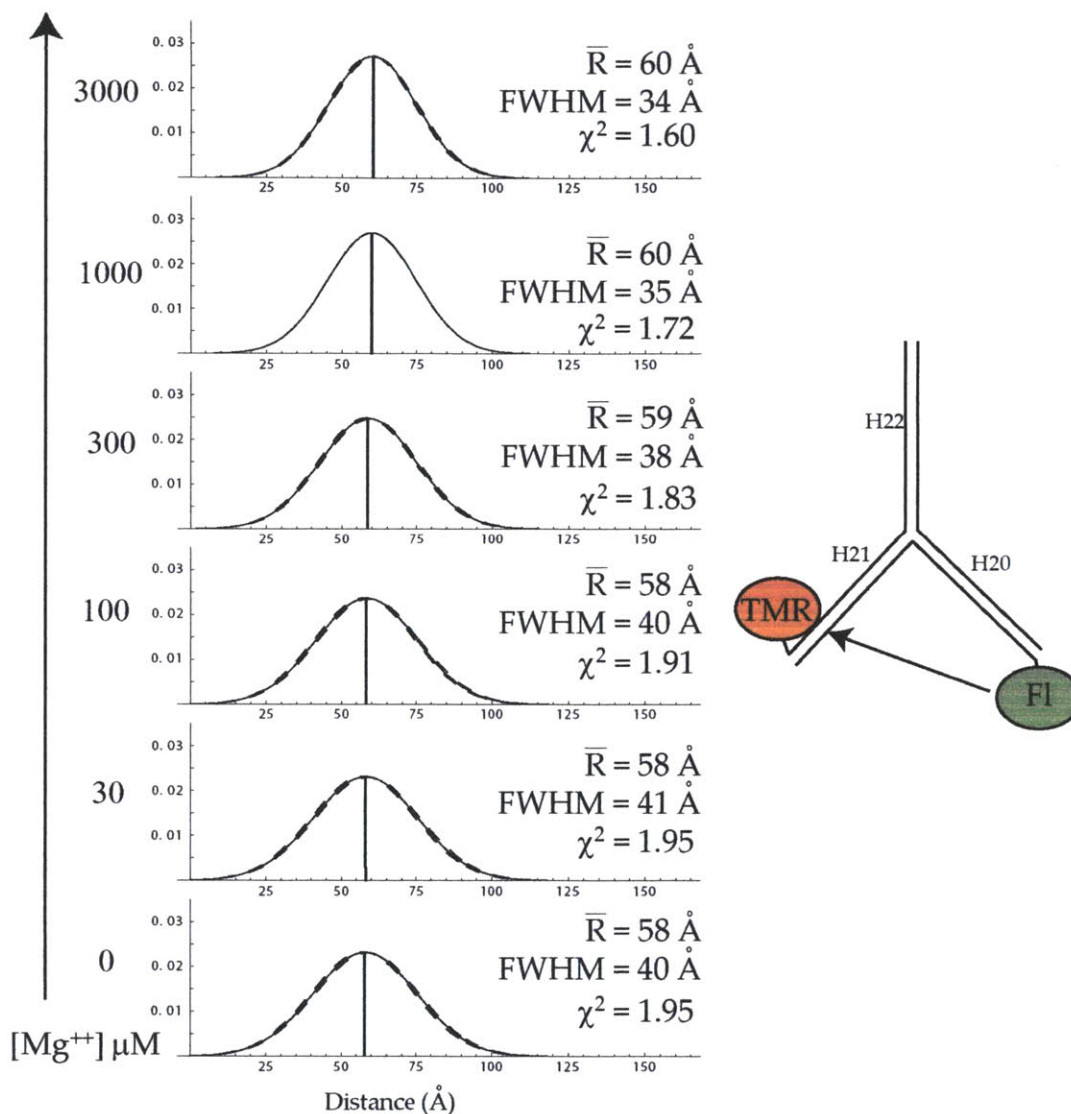


Figure 3.5 Helix 20-helix 21 trFRET results. Here we show the results of the energy transfer calculations using a model with a single distance distribution, and we report the mean distance (\bar{R}), the full width at half max (FWHM), and the goodness of fit (χ^2). We measured the fluorescence decay of a fluorescein moiety attached to the 5' end of helix 20 in the presence of a tetramethylrhodamine moiety attached to the 5' end of helix 21 as magnesium chloride was titrated from 0 μM to 3000 μM . Uncertainties in the distribution are shown as dashed lines. The mean distances between helix 20 and helix 21 remain essentially unchanged upon magnesium titration, and the fits of the data to the model are reasonably good.

than the model with two different distance distributions. In these instance the fraction of each second distance distribution is small (>3%) and the mean values are impossibly long (90 Å to 240 Å).

The energy transfer results between helix 21 and helix 22 using a model with a single distance distribution are shown below (Figure 3.6). At each concentration of magnesium chloride the fit of the data to a model with one distance distribution was nearly identical to the fit to a model with two different distance distributions. Similarly, the energy transfer calculations from helix 22 to helix 21 are fit equally well by models with either one or two distance distributions.

The energy transfer results between helix 20 and helix 22 upon addition of magnesium chloride are both more interesting and more complicated (Figure 3.7). At low magnesium concentrations (< 100 μM) a model with a single distance distribution returns similar mean distances (76-80 Å) and similar quality fits to the data ($\chi^2 > 1.36$) as a model with two distance distributions. At higher magnesium concentrations (300 μM - 3000 μM) the mean distances decrease and the χ^2 values increase. A model with two distance distributions does not fit these data any better; in each case either the mean distances are impossibly long, or the fits have similarly high χ^2 values.

The energy transfer results in the other direction from helix 22 to helix 20 are similarly complicated. At lower magnesium concentration (0 μM to 100 μM) the data are fit similarly well to a model with either one or two distance distributions based on χ^2 values and appearance of the residuals. As the magnesium concentration increases (300 μM to 3000 μM) the fit to the data are less straightforward. At 300 μM magnesium a two distance distributions give a lower χ^2 value, but the second distance is impossibly long and this model is easily rejected. At 1000 μM magnesium the model with two distances fits the data better based on χ^2 values, and the second mean distance (90.6 Å) is not impossible. At 3000 μM magnesium the fit of a single distance distribution to the data is poor ($\chi^2 = 6.26$); yet a model with two distance distributions yields an impossibly long mean distance. In these

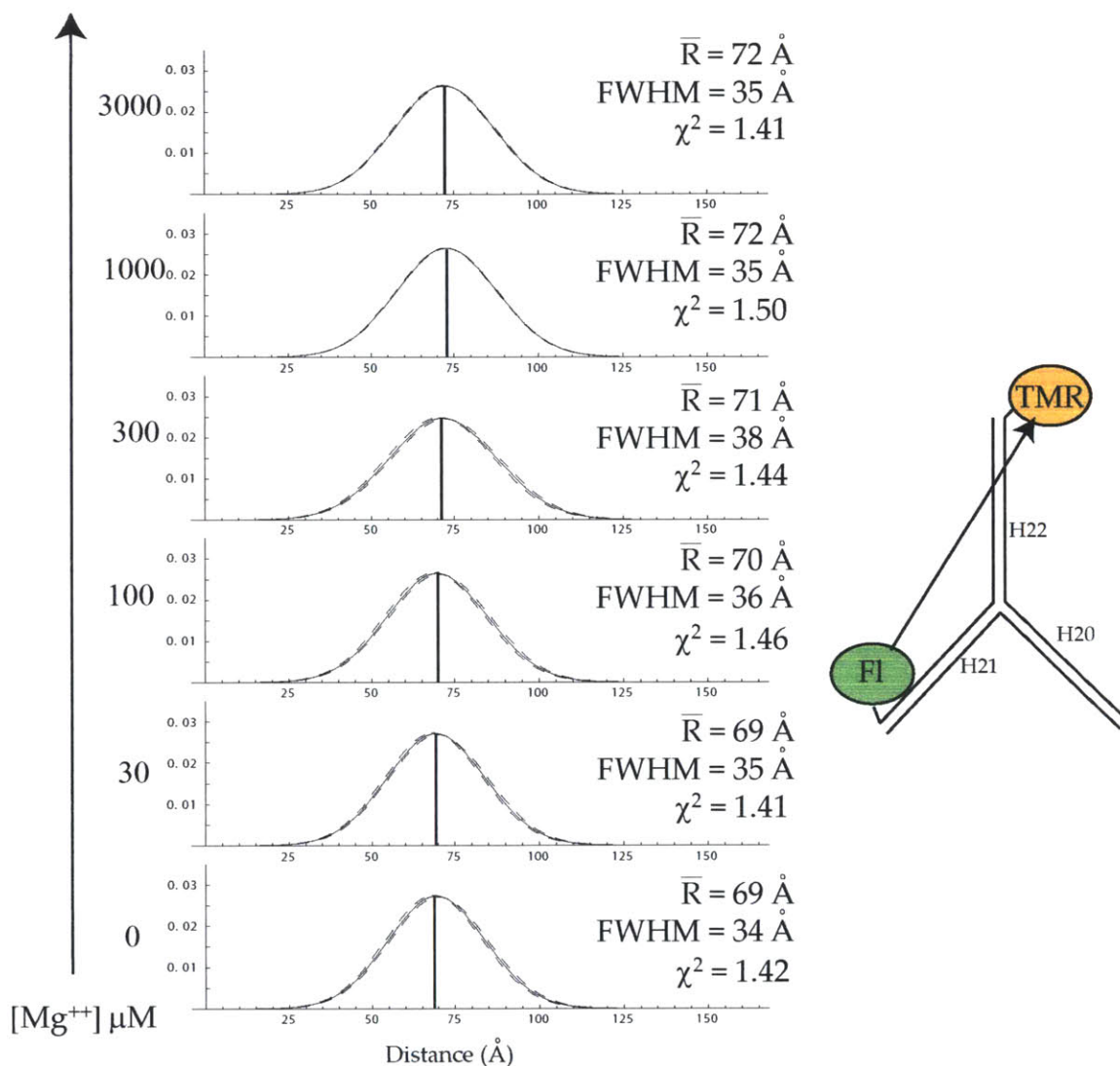


Figure 3.6 *Helix 21-helix 22 trFRET results*. Here we show the results of the energy transfer calculations using a model with a single distance distribution, and report the mean distance (\bar{R}), the full width at half max (FWHM), and the goodness of fit (χ^2). We measured the fluorescence decay of a fluorescein moiety attached to the 5' end of helix 21 in the presence of a tetramethylrhodamine moiety attached to the 5' end of helix 22 as magnesium chloride was titrated from 0 μM to 3000 μM . Uncertainties in the distribution are shown as dashed lines. The mean distances between helix 21 and helix 22 remain essentially unchanged upon magnesium titration, and the fits of the data to the model are quite good.

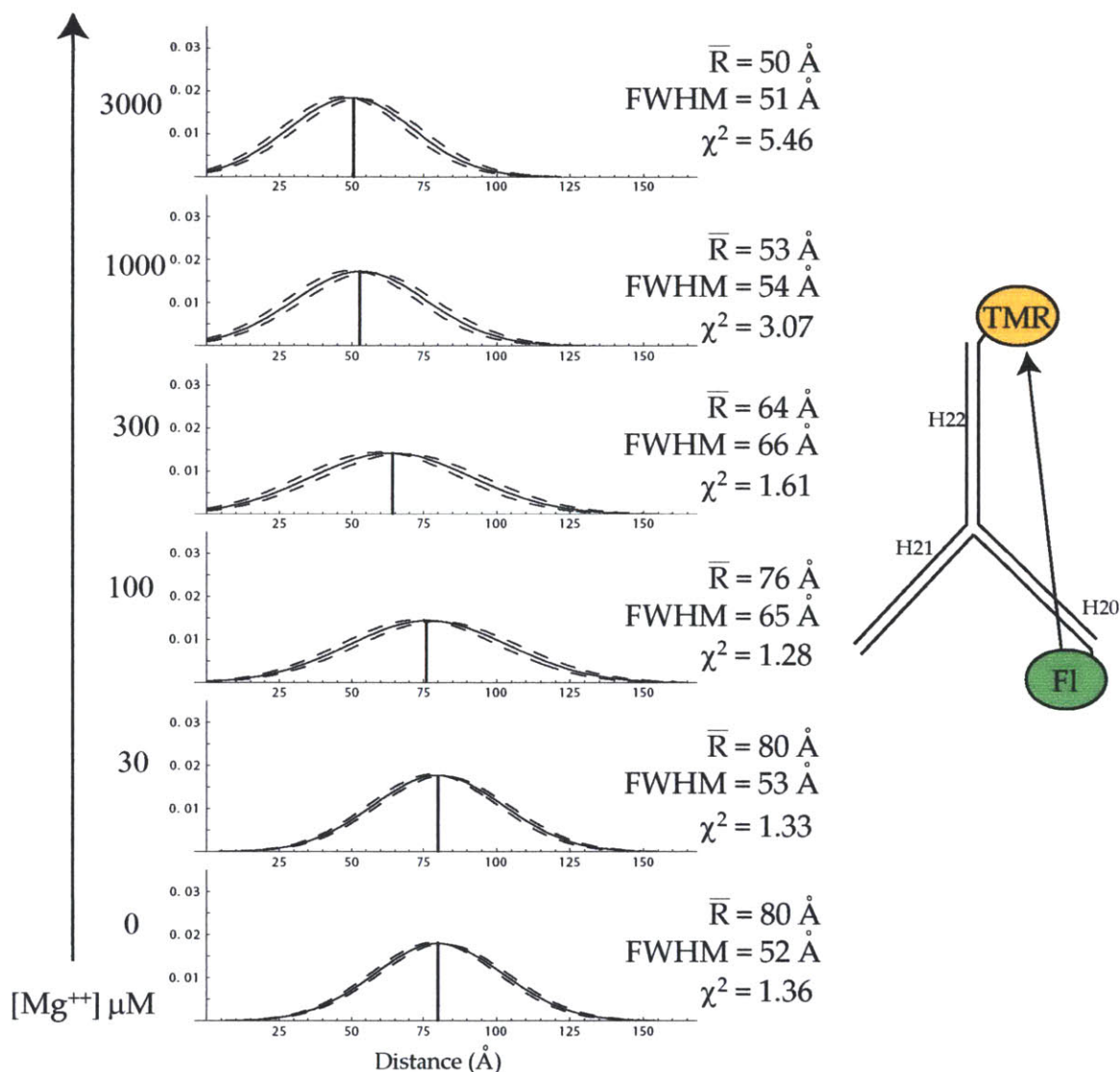


Figure 3.7 Helix 20-helix 22 trFRET results. Here we show the results of the energy transfer calculations using a model with a single distance distribution, and report the mean distance (\bar{R}), the full width at half max (FWHM), and the goodness of fit (χ^2). We measured the fluorescence decay of a fluorescein moiety attached to the 5' end of helix 20 in the presence of a tetramethylrhodamine moiety attached to the 5' end of helix 22 as magnesium chloride was titrated from 0 μM to 3000 μM . Uncertainties in the distribution are shown as dashed lines. The mean distances between helix 20 and helix 22 decrease significantly upon magnesium titration. The quality of the fit to the data based on χ^2 values grows worse as the magnesium increases and the distance between dyes decreases.

instances we can not say the inclusion of a second distance distribution improves the fit to the data.

3.5 BS15 induced conformational change in the helix 20, helix 21, helix 22 rRNA

Previously the helix 20, helix 21, helix 22 rRNA junction has been shown to undergo a conformational change upon binding protein S15 (Batey and Williamson, 1998; Orr *et al.*, 1998). Here we use trFRET to directly monitor these rRNA conformational changes to gain greater insight into assembly of the 30S ribosome central domain.

Three separate donor-only RNA samples were prepared by annealing a single 5' fluorescein-labeled oligonucleotide with a small excess of two unlabeled nucleotides in a low salt buffer (10 mM Hepes pH 6.5, 100 mM NaCl). Each donor-only RNA was prepared to 1 μ M, the sample was illuminated by a femtosecond laser, and BS15 protein was titrated into the RNA at 0 equivalents (0 μ M BS15), 0.5 equivalents (0.5 μ M BS15), and 1.1 equivalents (1.1 μ M BS15). The fluorescence decay data were collected and fit to a model with either two or three exponentials. In each case a model with three exponentials fit the data better than two exponentials based on both lower χ^2 values better fit of the residuals. These values were used later in the energy transfer calculations.

As in the magnesium chloride titration experiments, six individual donor-acceptor rRNA samples were used to measure the distances in both direction around the helix 20, helix 21, helix 22 rRNA junction upon addition of the S15 protein. These RNAs were prepared by annealing a 5' fluorescein-labeled oligonucleotide in a small excess of a 5' tetramethylrhodamine-labeled oligonucleotide and an unlabeled oligonucleotide in the low salt buffer (10 mM Hepes pH 6.5, 100 mM NaCl). The samples were illuminated by a femtosecond laser and the fluorescein fluorescence decay data were collected as BS15 protein was titrated from 0 equivalents to 1.1 equivalents. These data were fit to the energy transfer model using the lifetimes extracted from the donor-only experiments and either one or two distance distributions.

The averaged bi-directional distance calculations are shown below for the helix 20, helix 21, helix 22 junction upon BS15 titration (Fig. 3.8). These results have two striking features: two distances fit the data better at 0.5 equivalents of protein S15, and the mean distances are similar to the titration with magnesium chloride.

The directional energy transfer results between helix 20 and helix 21 using a model with a single distance distribution are shown below (Figure 3.9a). At each S15 concentration a single distance distribution fit the data reasonably well and returned a mean distances between 59 Å and 62 Å. The addition of a second distance distribution returns lower χ^2 values, but the mean distances are impossibly long and this model is rejected. Similarly, the energy transfer calculations in the other direction from helix 21 to helix 20 show a model with a single distance distribution is sufficient; the introduction of a second distance distribution does not offer meaningful improvement.

The energy transfer calculations from helix 21 to helix 22 using a single distance distribution are shown below (Figure 3.9b). Here the different models with one and two distance distributions return similarly good fits based on χ^2 values. Likewise, the energy transfer calculations in the other direction from helix 22 to helix 21 are similar for models with either one or two different distance distributions.

The results of the energy transfer calculations from helix 20 to helix 22 are quite interesting (Fig. 3.10). In the absence of S15 a model with two nearby distance distributions (means 71.9 Å and 83.4Å) gives a better fit to the data than a model with a single distribution. At 0.5 equivalents of S15 the model with two distributions yields a better fit ($\chi^2 = 1.30$) than the model with a single distribution ($\chi^2 = 1.72$). The two distributions both have reasonable fractions and mean distances (53% at 92.0 Å and 47% at 45.3 Å). At 1.1 equivalents of S15 the model with two distance distributions has a better fit; but one of the mean distances is impossibly long, and we are left with the model with a single distance distribution, a physically meaningful mean distance (55.8 Å), and a poor fit ($\chi^2 = 3.89$).

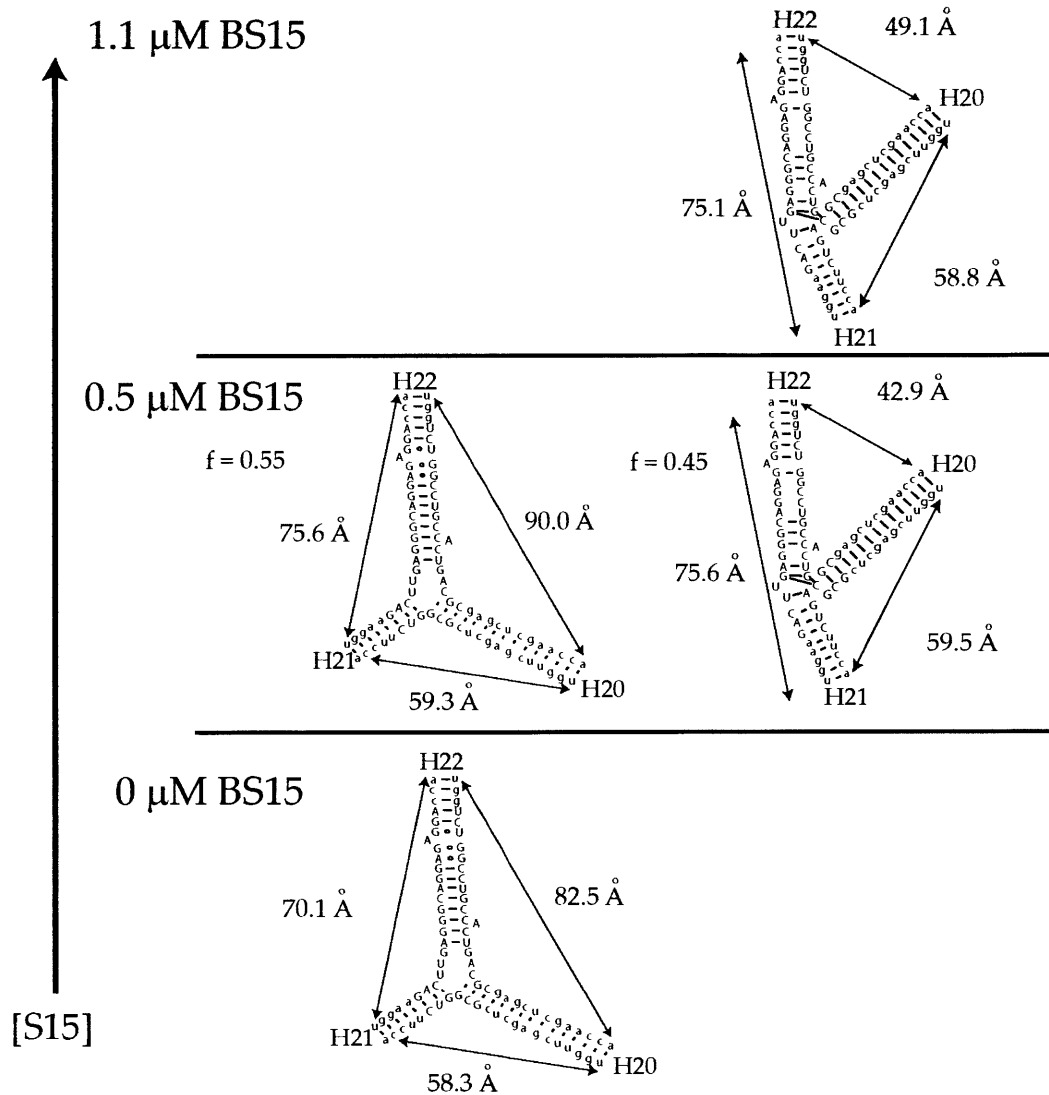


Figure 3.8 *trFRET* results for the helix 20, helix 21, helix 22 rRNA junction upon S15 titration. The reported distances are an average of the energy transfer in both directions between helices. At both low and high concentration of S15 an energy transfer model with a single distance distribution is sufficient to describe the data. At 0.5 equivalents S15 a model with two distance distributions fits the data better. The distance between helix 20 and helix 22 decreases upon addition of S15, and the distances between the other helices remain essentially unchanged.

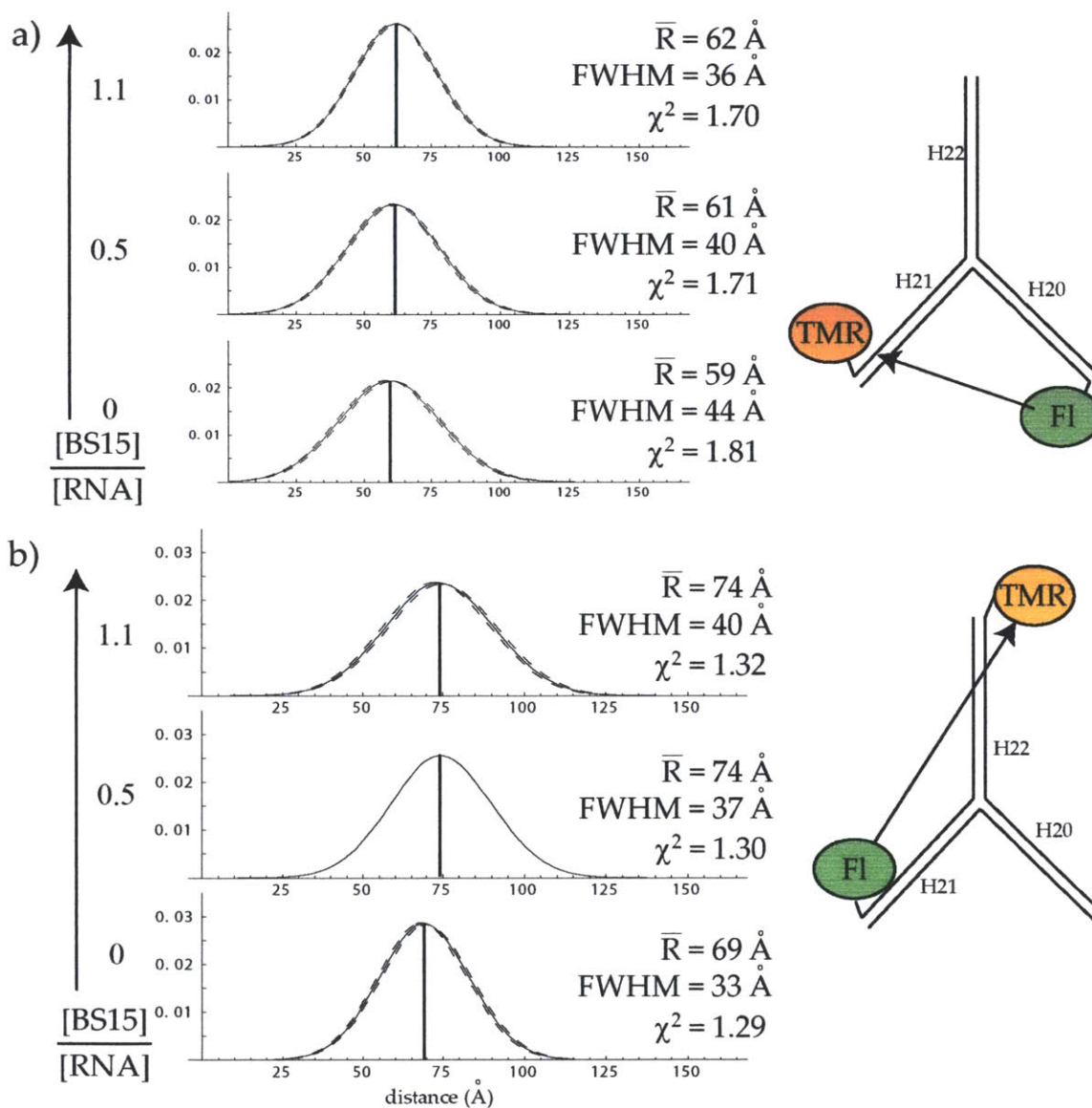


Figure 3.9 Helix 20-helix 21 and helix 21-helix 22 trFRET results upon BS15 titration. a) Directional results of energy transfer from helix 20 to helix 21 modeled by a single distance distribution. The mean distance remains essentially unchanged (59 Å to 62 Å) upon titration with BS15 and the quality of the fits to the data are good. b) Directional results of energy transfer from helix 21 to helix 22 modeled by a single distance distribution. The mean distance remains essentially unchanged (69 Å to 74 Å) upon titration with BS15. The quality of these fits to the data are also good.

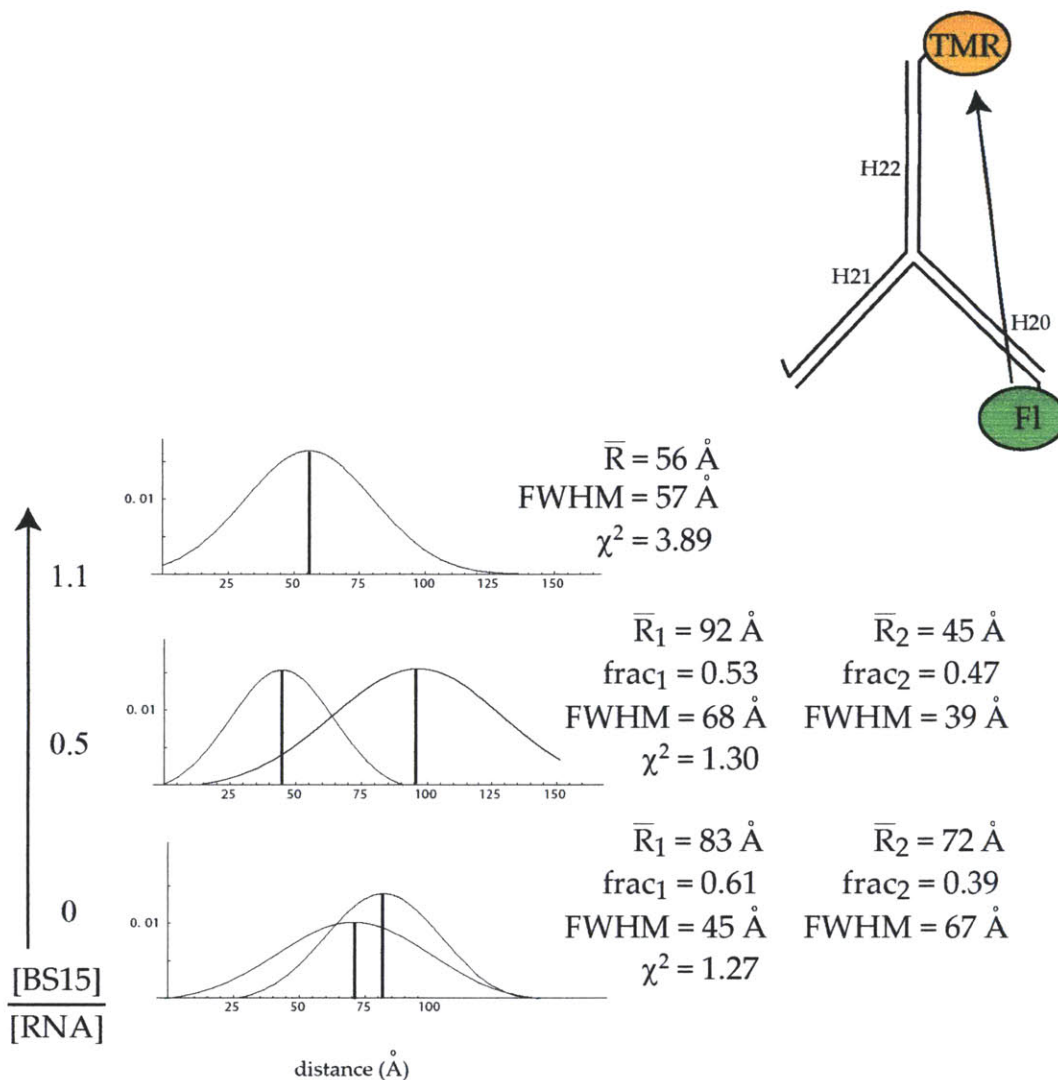


Figure 3.10 *Helix 20-helix 22 trFRET results upon BS15 titration.* In the absence of S15 the fluorescence decay data are fit better by a model with two closely spaced distance distributions. At 0.5 equivalents S15 the data are also fit better by a model with two distance distributions, one representing the unfolded conformation, and the other representing the folded conformation. At high S15 the data are not fit well by either model, but inclusion of a second distribution does not improve the quality of the fit.

The results of the energy transfer calculations in the other direction from helix 22 to helix 20 are similarly interesting. In the absence of S15 a model with a single distance distribution fits the data sufficiently well. At 0.5 equivalents of S15 the model with two distance distributions has an excellent fit ($\chi^2 = 1.14$) and reasonable fractions and mean distances (37% at 88.1 Å and 63% at 40.6 Å). At 1.1 equivalents of S15 the model with two distance distributions has a better fit; but again one of the mean distances is impossibly long, and we are left with the model with a single distance distribution, a physically meaningful mean distance (42.3 Å), and a poor fit ($\chi^2 = 3.52$).

3.6 Conformation of the helix 22, helix 23, helix 23a rRNA junction upon magnesium chloride titration

The helix 22, helix 23, helix 23a rRNA junction is believed to undergo a conformational change upon binding protein S15, and this may explain how S15 can mediate the sequential binding of S6 and S18 in 30S ribosome assembly without direct interaction between protein S15 and the S6:S18 heterodimer (Agalarov and Williamson, 1998; Agalarov *et al.*, 2000). Here we use trFRET to see if the divalent magnesium cation can stabilize a reorganization of this rRNA junction, similar to the stabilization of the folded conformation of the helix 20, helix 21, helix 22 RNA junction.

RNA constructs used to probe magnesium-stabilized conformational changes of the helix 22, helix 23, and helix 23a rRNA junction consists of only two oligonucleotides because helix 23a is a contiguous short stem-loop (Fig. 3.11). The donor-only sample was prepared by annealing two complementary oligonucleotides, one with a fluorescein moiety attached to the 5' strand of helix 23 by a six carbon linker, and the other oligonucleotide unlabeled. The sample was prepared to 1 μ M RNA in a low salt buffer and illuminated with a femtosecond laser as magnesium chloride was titrated from 0 μ M to 3000 μ M. At each concentration of magnesium the fluorescein fluorescence decay data were collected and fit to a model with either two and three exponentials. At each magnesium concentration the model with three exponentials fit the data much better based on lower χ^2 values and appearance of the residuals.

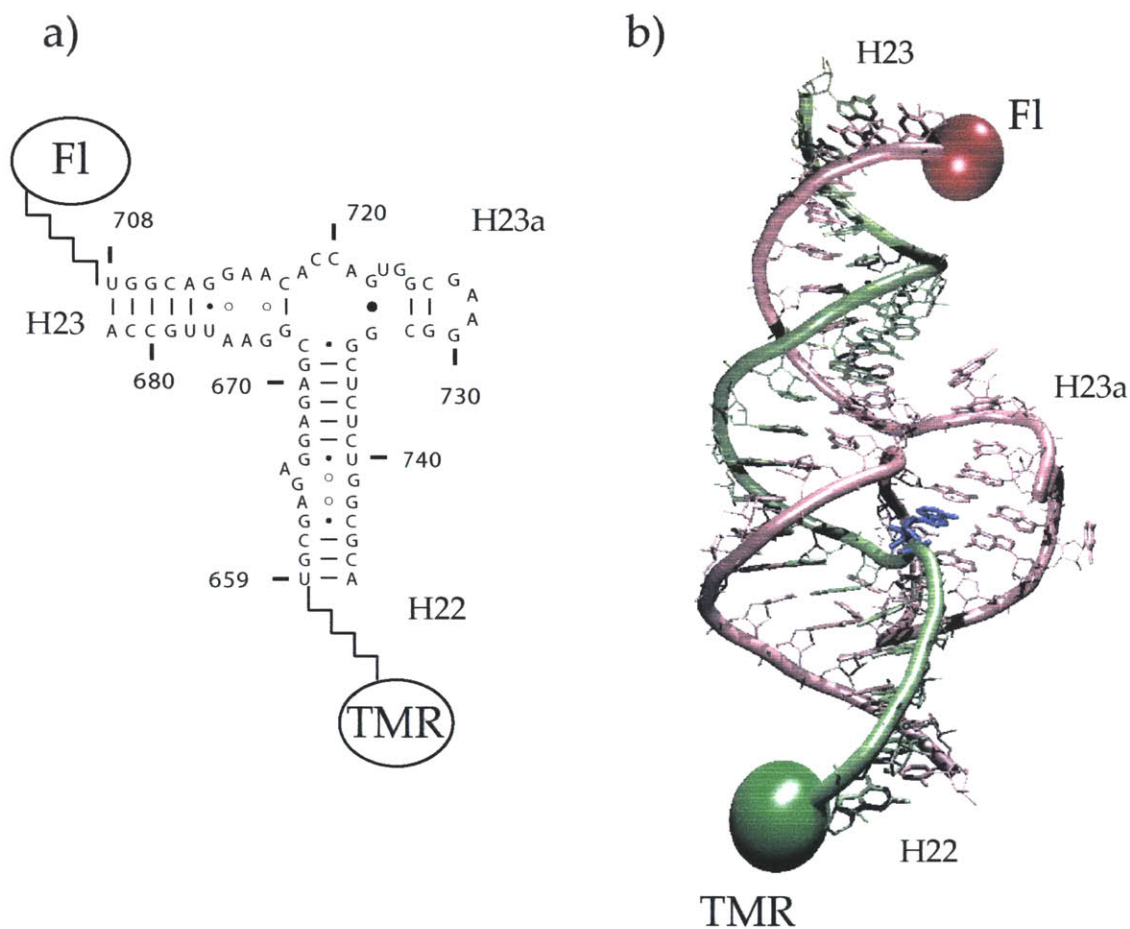


Figure 3.11 *Helix 22, helix 23, helix 23a rRNA trFRET construct*. a) Secondary structure of the dye-labeled oligonucleotides used in trFRET experiments to monitor conformational change in the h22,h23,h23a junction. A donor-only sample was prepared with fluorescein attached to the 5' end of helix 23 and the complementary unlabeled oligonucleotide. A donor-acceptor sample was prepared with fluorescein attached to the 5' end of helix 23 and tetramethylrhodamine attached to the 5' end of helix 22. b) 3D model of the rRNA constructs based on the crystallographic structure of the folded RNA. The dyes fluorescein (red) and tetramethylrhodamine (green) are represented by spheres at the 5' ends of the individual oligonucleotides. The extrahelical A665 from helix 22 is shown in blue, base paired to G724 in helix 23a.

A donor-acceptor RNA sample was prepared similarly to the donor-only sample, but with a fluorescein moiety attached to the 5' end of helix 23 and a tetramethylrhodamine moiety attached to the 5' end of helix 22 (Fig. 3.11). The sample was illuminated with a femto-second laser and the donor fluorescence decays were collected in the presence of the acceptor dye as magnesium chloride was titrated. The donor fluorescence data were fit to an energy transfer model containing either one or two distance distributions using the three lifetimes extracted from the donor-only samples.

At each concentration of magnesium chloride the fluorescence decay data were fit reasonably well by an energy transfer model with a single distance distribution (Fig. 3.12). In a few cases a model with two distance distributions gave a slightly better fit numerically, but the second distance was either impossibly long or unreasonably short. Overall, we see almost no changes in dye separation (77 Å to 79 Å) at magnesium concentrations up to 300 μM, and only minor changes in distance (72 Å) at magnesium concentration up to 3000 μM (72 Å). The reported distances are slightly longer than expected if helix 22 and helix 23 are stacked coaxially (~64 Å), but within the uncertainty of dyes attached by six-carbon flexible linkers.

3.7 Single-pair FRET (spFRET) observation of helix 20, helix 21, helix 22 rRNA conformational subpopulations

Single molecule fluorescence methods allow for direct observation of individual molecules in solution, not just the averaged behavior of an ensemble. Here radiometric single pair fluorescence resonance energy transfer (spFRET) is used to construct a distribution of individual energy transfer events in a population of freely diffusing dye-labeled rRNAs to probe the effects of magnesium and protein S15 on the conformation of the helix 20, helix 21, helix 22 junction.

The experimental setup for these spFRET experiments is outlined below (Fig. 3.13). The rRNA samples were prepared similarly to the ensemble trFRET constructs, here with the dye Cy3 attached to the 5' end of helix 20 and the dye Cy5 attached to the 5' end of helix

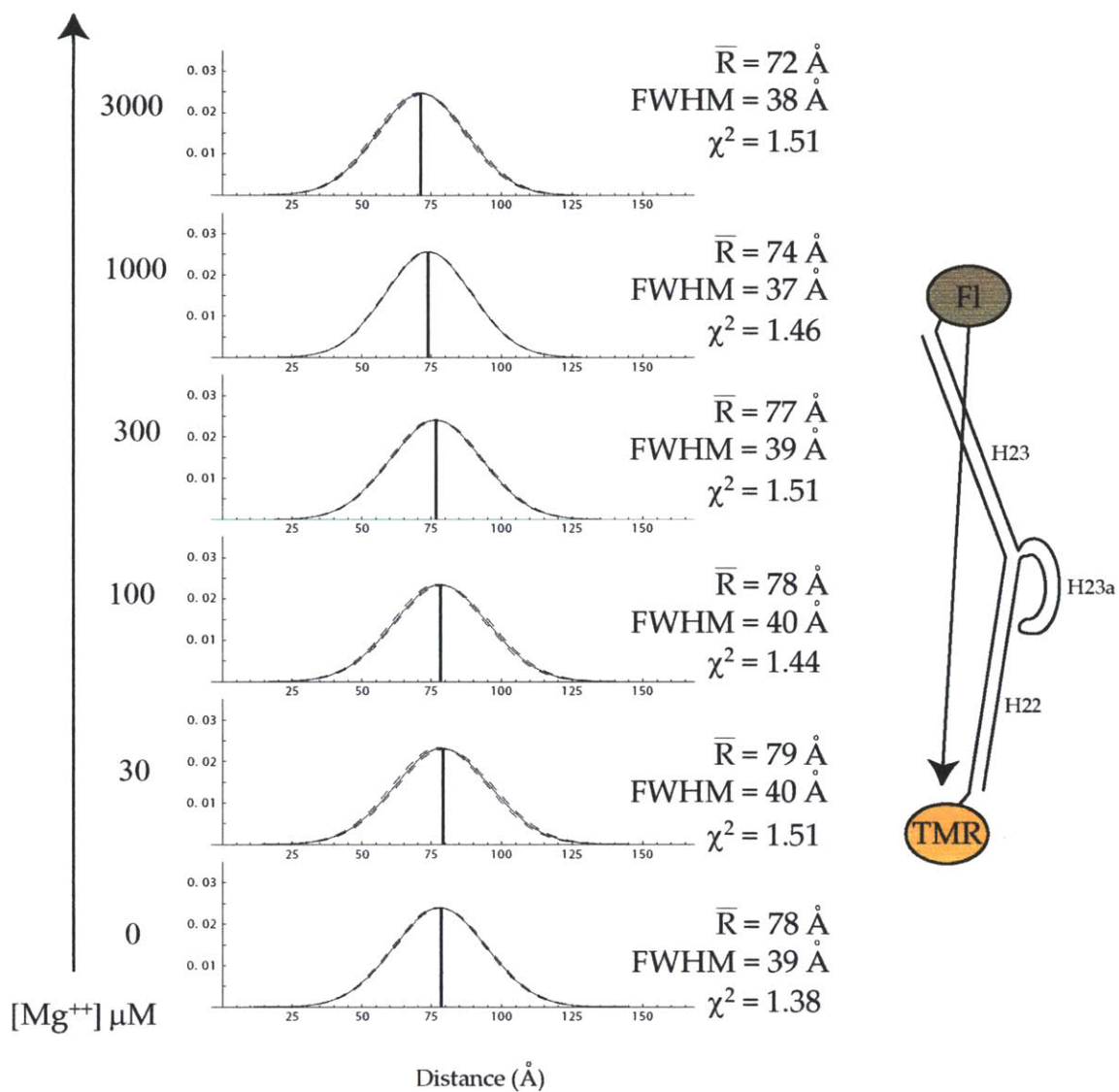


Figure 3.12 *Helix 22, helix 23, helix 23a trFRET magnesium titration results.* This three-helix junction rRNA has a fluorescein moiety attached to the 5' end of helix 23 and a tetramethylrhodamine moiety attached to the 5' end of helix 22. The data were fit sufficiently well by a model with a single distance distribution. The mean distances shorten only slightly from 78 Å to 72 Å as magnesium chloride is titrated from 0 μM to 3000 μM.

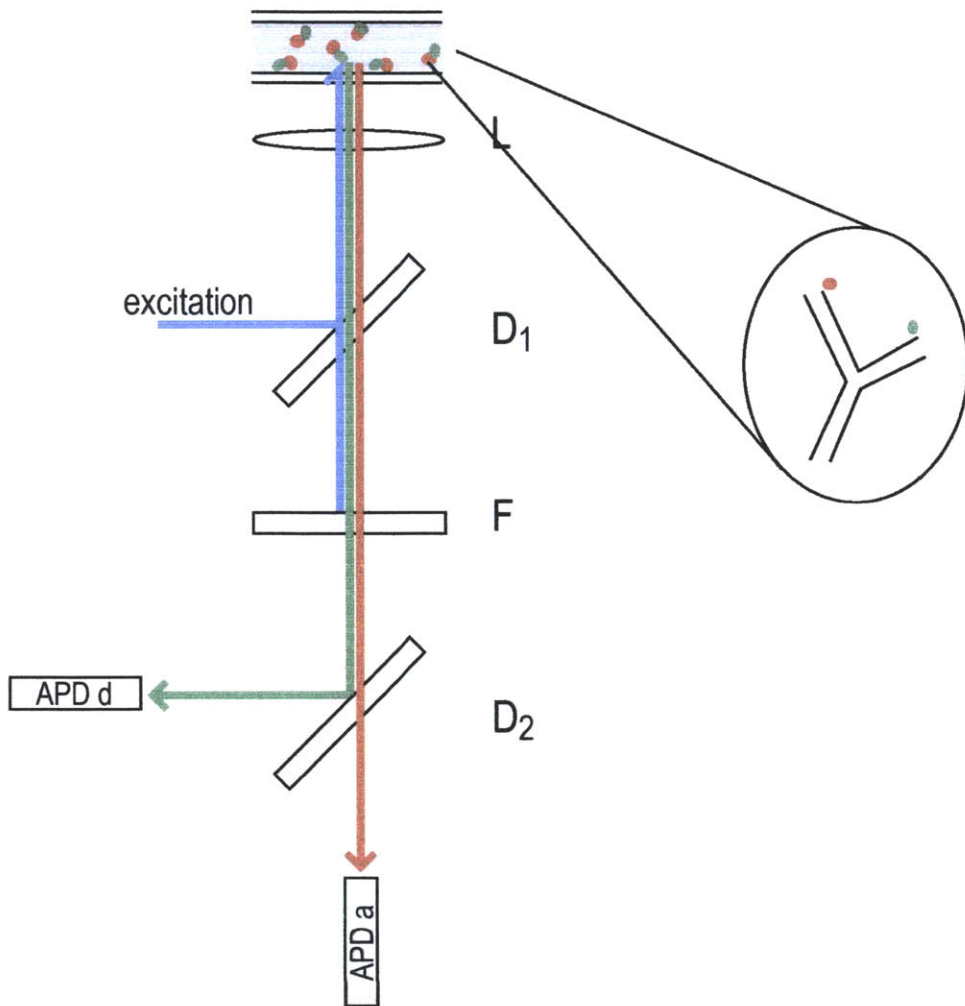


Figure 3.13 Schematic diagram of spFRET experiment. Dye-labeled RNAs are excited through an inverted confocal microscope and fluorescence emissions are collected through the same device. The excitation laser light (blue) is excluded with a filter (F). The individual donor and acceptor emission are separated with a dichroic mirror (D₂) and collected in 50 μ s time bins with separate avalanche photocopies.

22. This dye pair has an R_0 value of 53 Å. The individual RNA oligonucleotides were annealed in a PCR machine and diluted to 10 pM in low salt buffer before addition of magnesium chloride or protein S15. The samples were illuminated with a laser through an inverted confocal microscope, and emissions from a femtoliter volume were selected by passing the light through a pinhole. The emission was filtered to remove any scattered excitation light, separated using a dichroic mirror, and recorded by separate avalanche photo diodes in 50 μs time bins. The data were converted into a histogram of FRET efficiencies to show the distribution of the RNA populations in different conformational states. The FRET efficiency is calculated as $E_i = I_a / (I_a + I_d)$, where I_a is the acceptor intensity, and I_d is the donor intensity.

Our results indicate the helix 20, helix 21, helix 22 rRNA junction has predominately low FRET efficiency in the presence of 0.5 nM S15, well below the reported dissociation constant K_d (Batey and Williamson, 1996a)(Figure 3.14). This low FRET efficiency indicates a distance well above the R_0 value of 53 Å, consistent with our understanding of the rRNA in an ‘unbound’ state. There is also a very small fraction of rRNAs with high FRET efficiency, indicating a separate sub-population of the rRNAs in the folded form. The addition of 5.0 nM ribosomal protein S15, near the K_d for similar rRNAs, shifts the distribution of rRNA structures to a larger fraction of molecules with a high FRET efficiency. This clearly shows the presence of two sub-populations of RNA, one unfolded and the other folded and stabilized by protein S15. At 50 nM S15, well above the K_d , the RNAs shows predominately high efficiency FRET, indicating most of the rRNA molecules are folded and presumably bound to the protein. It is difficult to tell how much of the ‘unbound’ population is hidden under the ‘zero peak’ fluorescence. Similarly, the addition of 6 mM magnesium chloride, well above the reported 150 μM K_d , results in a large fraction of rRNA molecules with high FRET efficiency, indicating most of the rRNAs are folded at high salt concentration with helix 20 and helix 22 close together (Figure 3.15). Again, it is difficult to tell what fraction of the molecules are in the low efficiency conformation because they are hidden under the ‘zero peak’ fluorescence.

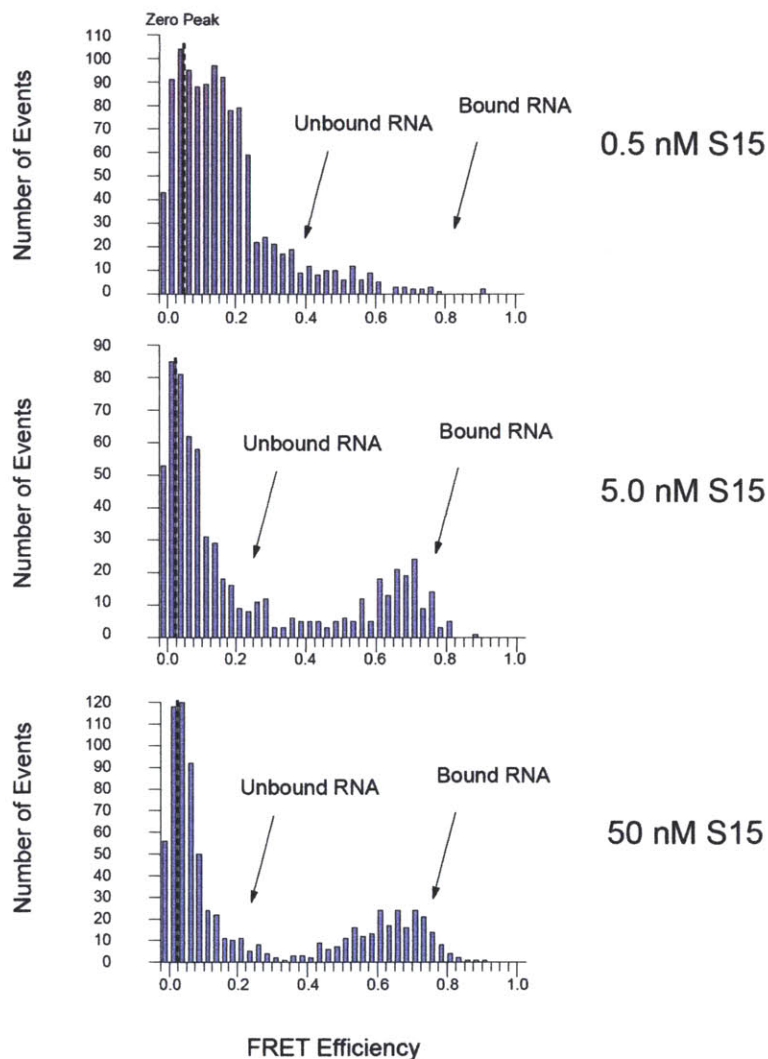


Figure 3.14 *spFRET* results of BS15 protein titration into rRNA binding site. (Upper panel) Addition of BS15 protein below the K_d to the rRNA results in a large fraction of rRNA with low FRET efficiency, indicating a large distance between Helix 20 and Helix 22 and a low fraction of the protein bound. (Middle panel) Addition of BS15 protein near the K_d shows presence of both a low FRET efficiency population and a high FRET efficiency population, indicative of subpopulations of both ‘bound’ and ‘unbound’ rRNA. (Lower panel) Addition of BS15 protein above the K_d shows results in predominately high FRET efficiency, indicating most of the rRNA is ‘bound’ to the protein.

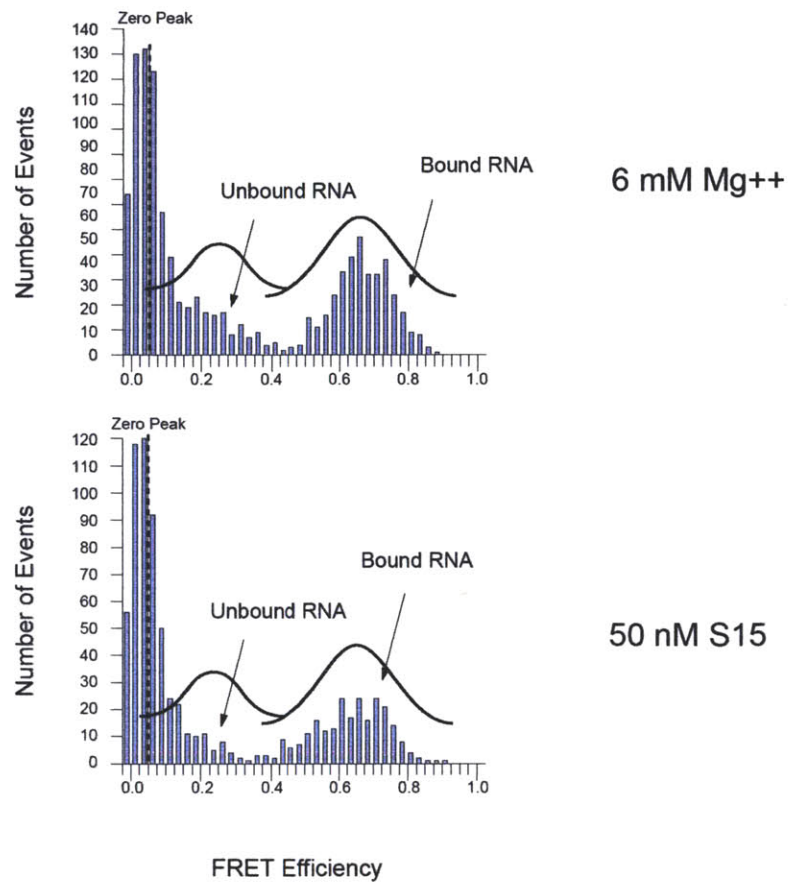


Figure 3.15 *spFRET* results of magnesium chloride addition to rRNA. (Upper panel) Addition of 6 mM magnesium chloride results in a large population of rRNA with high FRET efficiency, indicating a distance between Helix 20 and Helix 22 well below the R_0 value of 53 Å for the Cy3-Cy5 dye pair. These results are similar to the addition of BS15 protein above the K_d , where the rRNA also exhibits a large fraction with high FRET efficiency.

3.8 Discussion

Here we used trFRET methods to investigate conformational changes in the helix 20, helix 21, helix 22 rRNA junction upon addition of magnesium chloride or protein S15. To validate the trFRET method in our system we measured the distance along a 23 base pair duplex A-form RNA corresponding to the helix 20-helix 21 segment in our tripartite RNA. The measured distances at both low magnesium chloride concentration (63.9 Å) and high magnesium chloride concentration (65.3 Å) are in excellent agreement with the expected distance (64.4 Å) based on values from crystallographic measurement of A-form RNA (Bloomfield, et. al., 2000). The results were fit reasonably well by an energy transfer model with a single distance distribution, although the χ^2 value was slightly high at high salt. We did not expect a second distance distribution would improve the fit in this linear duplex.

Our measurements of the distances between helices in the helix 20, helix 21, helix 22 rRNA junction confirm a significant rearrangement of the three-helix junction to bring helix 20 and 22 closer upon addition of either divalent salt or protein S15, confirming earlier observations (Fig. 3.16). Our results show, however, there is no substantial change in the distance between helix 20 and helix 21, nor is there any substantial change in the distance between helix 21 and helix 22. These findings are different from those reported earlier (Orr, *et al.*, 1998), where the three-helix junction in low-salt conditions was shown to be planar with each helix essentially 120° apart, and addition of high-salt or protein S15 mediates both a decrease in distance between helix 20 and helix 22 and the coaxial stacking of helix 21 and helix 22. Our new results suggest the three-helix junction is partially ‘folded’ in the low salt condition, with helix 21 and helix 22 coaxially stacked. The change in distance between helix 20 and helix 22 could be the result of a rotation of helix 20 around this preformed structure to form the G654:G752:C754 base triple and the U652:A753 reverse Hoogsteen in the folded junction. We know there is a kink in the middle of helix 22 from the bulged nucleotide C748, and a rotation of helix 20 from the distal side of this kink to the proximal side could explain how only one distance in the three-helix junction changes, while the other two distances remain essentially unchanged.

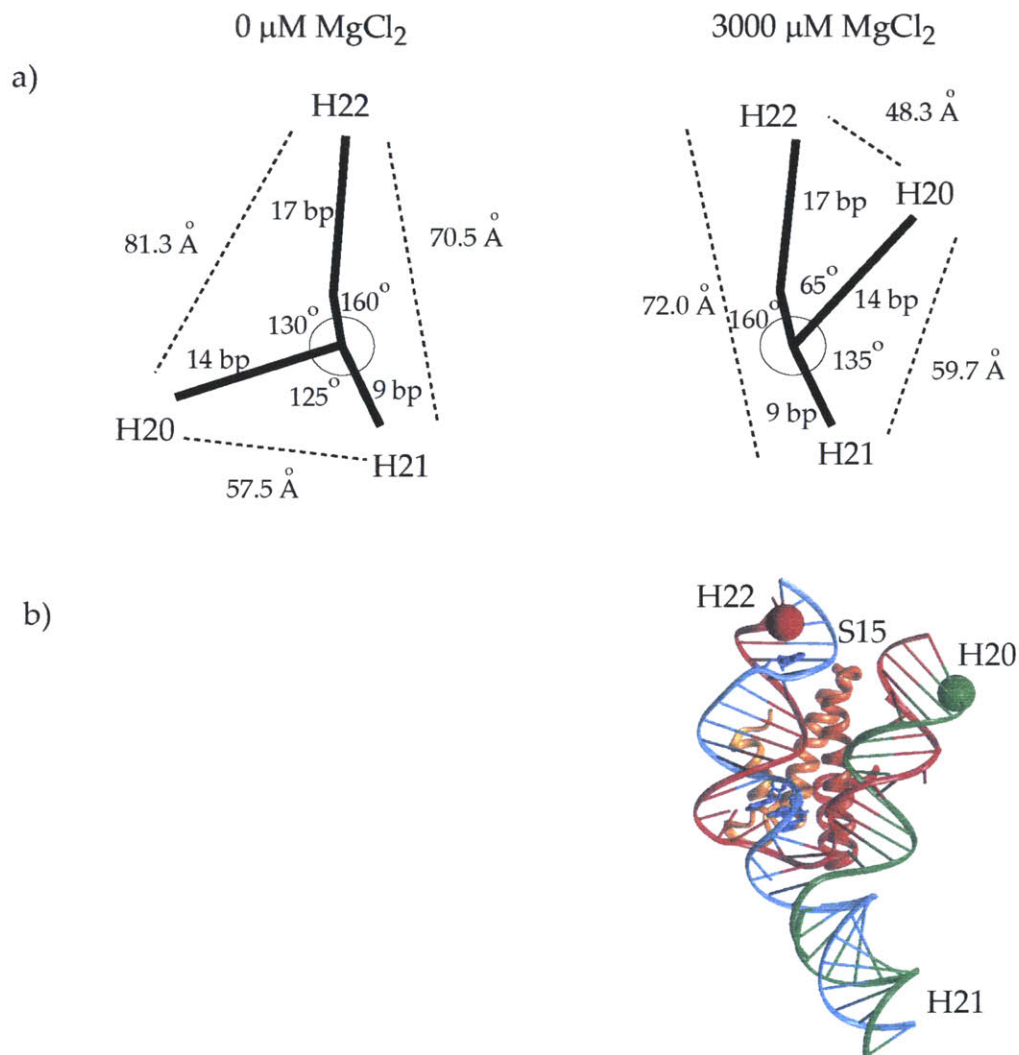


Figure 3.16 *Model of the helix 20, helix 21, helix 22 conformational change upon addition of magnesium.* a) Stick figure of the rRNA showing lengths of helices in base pairs (bp), measured lengths between the dyes (\AA), and angles between the helices. The angles were calculated using A-form RNA parameters for the lengths of the helices. Upon addition of magnesium chloride the distances between helix 20 and helix 21 does not change significantly, nor does the distance between helix 21 and helix 22. The distance between helix 20 and helix 22 shows significant shortening, presumably by a rotation of helix 20 around the partially formed core of the three-helix junction. b) Model of the tripartite rRNA construct based on the rRNA in the ‘folded’ conformation bound to protein S15 from the x-ray crystal structure. Here we see the acute angle between helix 20 and helix 22, coaxial stacking between helix 21 and helix 22, and a small kink in the middle of helix 22 from bulged C748.

The results of the energy transfer calculations between helix 20 and helix 21, and between helix 21 and helix 22 are rather straight forward. A model with a single distance distribution was sufficient to fit the fluorescence decay data reasonably well in almost every instance of addition of magnesium chloride or protein S15 to these RNAs. In some instances the inclusion of a second distance distribution to the energy transfer model did yield a better fit based on lower χ^2 values, but the mean distances were longer than physically possible in most instances and these models were easily rejected in favor of the simpler model with only a single distance distribution.

The results of the energy transfer calculations between helix 20 and helix 22 are both more interesting and more complicated. Upon addition of one-half equivalent of protein S15 we expect half the RNA are bound to protein and 'folded'. Indeed, an energy transfer model with two distance distributions fits these data significantly better and returns physically meaningful distances and fractional populations. In two other instances, however, one at high concentration magnesium chloride and another without either magnesium or S15, the model with two distance distributions fit the data better than a model with only one distance distribution. We have no easy explanation for these observations. Also, at high concentrations of both magnesium and protein S15 the χ^2 values for the fits are quite high, and we have low confidence in the quality of the fits of the data to the model and the reported mean distances. Fortunately, our knowledge of the 'folded' RNA confirmation from the x-ray crystal structure gives us confidence in the essence of the conformational change, if not in the exact numerical results of the energy transfer calculation.

We also used trFRET methods to look for a conformational change in the helix 22, helix 23, helix 23a rRNA junction. We know protein S15 mediates the binding of proteins S6 and S18 in central domain assembly, and because there are no protein-protein contacts in the x-ray crystal structure we infer there must be a conformational change across this three-helix junction. The design of an RNA to probe this conformational change upon binding protein S15 is quite difficult because both three-helix junctions in the S15 RNA binding site were assumed to undergo conformational change. Therefore, we began with a 'simple' construct consisting of only the helix 22, helix 23, helix 23a junction to investi-

gate if magnesium has any effect on the conformation of this RNA junction, similar to the conformational change seen in the helix 20, helix 21, helix 22 junction. Our results showed only a minor decrease in distance between helix 22 and helix 23 at high magnesium chloride concentration (Fig. 3.12). This result indicates there is no major reorganization of the three-helix junction upon addition of magnesium, but might indicate more subtle structural changes. The observed distances (72 Å - 78 Å) are slightly longer than expected if the portions of helix 22 and helix 23 form duplex A-form RNA (64.4 Å), but are within reason for dyes attached with flexible six-carbon linkers. Therefore, we must conclude helix 22 and helix 23a are indeed coaxially stacked in the low salt condition for the dyes to be this far apart. We can also conclude the effect of S15 in the T4 particle is not a complete reorganization of the three-helix junction, but is a more subtle change, perhaps in helix 23a sufficient to form the proper binding site for the S6:S18 heterodimer. This could include stabilizing the formation of the interhelical A665:G724 base pair that has been shown essential to S6:S18 binding in the T4 particle (Agalarov, *et al.*, 2000). Residues 717-719 in a loop region between helix 23 and helix 23a also show S15-dependent enhancement of chemical reactivity, and S6:S18-dependent protection, indicating they might be part of a more subtle S15-stabilized conformational change in this RNA junction (Svensson, *et al.*, 1988).

spFRET methods were also used to investigate the behavior of the helix 20, helix 21, helix 22 RNA junctions free in solution. We observed a transition from low efficiency FRET to high efficiency upon addition of S15 around the K_d value, indicating the stabilization of a folded structure upon protein binding. We also observed distinct subpopulations of each state near the K_d value, showing the true power of single-molecule methods. We also observed high efficiency FRET in an excess of magnesium, which indicates spFRET methods could be useful for further investigation of RNPs free in solution.

We can combine our structural studies of the individual three-helix junctions at each end of helix 22 with other information to build a more complete model of assembly in T4-like RNPs, and by extension formation of the core of the 30S central domain (Figure 3.17). In isolated model systems we have shown both helix 21 and helix 23 stack coaxially onto

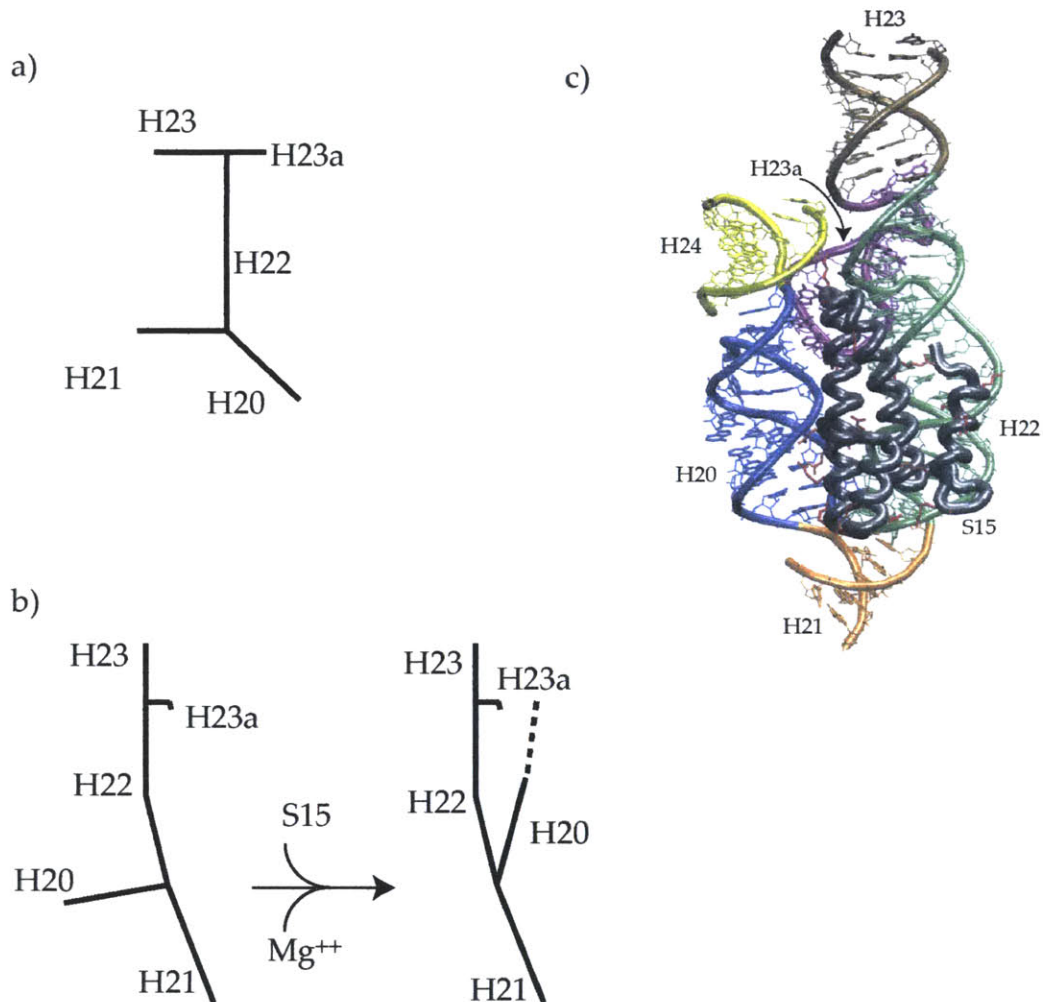


Figure 3.17 *Revised T4 RNP assembly model.* a) Stick-figure representation of the canonical secondary structure of the core of 16S central domain RNA representing a T4-like RNA. b) Combined trFRET results for both three-helix junctions at the ends of 16S RNA helix 22. Helix 21 and helix 23 both stack coaxially onto helix 22 in the absence of either protein S15 or magnesium ion. Addition of either magnesium or S15 promote a rotation of helix 20 proximal to helix 22. c) Structure of the S15-binding site from the 30S subunit, showing close contacts between helix 20 (blue) and helix 23a (purple). The lack of S15-dependent sensitivity to chemical probing of residues in helix 20 may indicate these tertiary contacts are present prior to S15 binding.

helix 22 in the absence of either magnesium or S15. We have also confirmed that addition of either magnesium or S15 promotes a rotation of helix 20 and brings it proximal to helix 22. We know from the T4 particle that S15 is necessary for binding the S6:S18 heterodimer, presumably by stabilization of the A665:G724 interhelical base pair, or stabilization of another particular structure in helix 23a. Studies in a similar system from *Aquifex aeolicus* have shown only very weak binding of the AS6:AS18 heterodimer to the T4-like RNA in the absence of S15, and a 30,00-fold cooperative increase in binding in the presence of AS15 (Recht and Williamson, 2001). Further investigation of central domain assembly thermodynamics using a larger central domain RNA has shown the AS6:AS18 heterodimer can bind the RNA tightly in the absence of S15, presumably because tertiary contacts seen in 30S structures between helix 20 and the helix 23a tetraloop are sufficient to stabilize formation of the binding site for the S6:S18 heterodimer (Fig. 3.17c) (Recht and Williamson, 2004). These additional tertiary RNA contacts decrease the cooperativity between AS15 and AS6:AS18 by a factor of 1000. Residues in helix 20 show no S15-dependent sensitivity to chemical probing, indicating the tertiary contacts with the helix 23a tetraloop may be present before addition of S15 (Svensson, *et al.*, 1988). This may partially explain the reduced cooperativity between S15 and the S6:S18 heterodimer in larger central domain RNPs.

Chapter 4: Materials and Methods

4.1 Reagents

All reagents were of the highest quality available, and used without further purification unless stated otherwise.

RNA samples were generously donated by Robert Batey, Jeff Orr, Dagmar Klostermeier, and Sultan Agalarov. RNA samples for crystallization of the *B. stearrowthermophilus* S15:rRNA complex were prepared by T7 RNA polymerase run-off transcription from SmaI -linearized plasmid DNA (Batey and Williamson, 1996a). RNA samples for crystallization of the *T. thermophilus* S6,S15,S18:rRNA complex were prepared by SP6 RNA polymerase run-off transcription from linearized plasmid DNA (Agalarov and Williamson, 1998).

RNA samples were stored either as frozen lyophilized pellets, as frozen stock solutions, or as refrigerated working solutions. The lyophilized pellets were reconstituted with deionized water passed through 0.22 micron filters. The stock RNA concentration was determined through UV spectroscopy of base hydrolyzed samples by measuring the absorbance at 260 nm. Working samples were stored at 4 °C in 0.5 mL snap-top tubes. These samples were annealed at 95 °C for 2 minutes in a Perkin Elmer PCR-Mate with a heated bonnet. The samples were cooled at -2 °C per minute until at 25 °C or 4 °C.

RNA oligonucleotides for fluorescence studies were purchased from Dharmacon Research, Inc. as lyophilized, unpurified 5'-OH or dye-labeled 2'-orthoester (2'-ACE) protected product from 0.2 μmole 3'- to 5'- solid support-bound phosphoramidite synthesis. RNA oligos were selectively labeled at the 5' position with the fluorescent dyes fluorescein (Fl) and tetramethylrhodamine (TMR), both attached by a six-carbon linker, or with Indodicarbocyanine 3 (Cy3) or Indodicarbocyanine 5 (Cy5), both attached by a three-carbon linker. These dye-labeled samples were handled under low-light conditions to minimize photo-bleaching.

The oligos were deprotected at the 2'-OH by acid hydrolysis at 60° for 30 to 120 minutes in a mixture of acetic acid (100 mM) and N-N-N'-N'-tetramethylethylenediamine, pH 3.8 (Dharmacon), and the volatile deprotection by-products and reagents were removed by lyophilization. The oligos were rehydrated gently in electrophoresis load buffer containing glycerol (15% v/v) in ddH₂O, but without bromphenol blue or xylene cyanol FF marker dyes, then loaded by pairs onto 12 cm wells in denaturing polyacrylamide (20% w/v acrylamide, 29 : 1 acrylamide : bis-acrylamide) gels, containing urea (8 M). The vertical sandwich gels, measuring 1.5 mm W x 240 mm L x 350 mm, were pre-run at 40 W constant power for at least 60 minutes in electrophoresis buffer (0.5x TBE) containing Tris-borate (45 mM, pH 8.0) and ethylenediaminetetraacetic acid (EDTA, 1 mM). After electrophoretic migration through at least 12 cm of gel matrix, usually lasting four to six hours, the gel apparatus was disassembled, one glass plate of the gel sandwich was removed, and the exposed gel surface covered in plastic wrap (Saran, SC Johnson). The dye-labeled oligos were visible even under low ambient light, and were excised directly with a sterile razor blade into 50 mL polypropylene tubes (Fisher). The colorless unlabeled oligos, which were visualized in the gel and marked with a pen after brief UV shadowing at 254 nm, were also cut from the gel. All samples were covered in 25 mL soak buffer containing 0.5x TBE and sodium acetate (0.3 M, pH 5.2), placed on an oscillating shaker.

The ribosomal protein S15 cloned from *Bacillus stearothermophilus* was overexpressed in *E. coli* and purified by HPLC as reported earlier (Batey and Williamson, 1996a).

4.2 T4 RNP crystallography

Preliminary RNP crystal screening on the *B. st.* S15:Fr12 rRNA complex was performed using the Doudna screening method (Doudna, 1993). Two microliters purified BS15 were mixed with two microliters purified Fr12 rRNA on a silanized glass cover slip and inverted over a one milliliter buffer reservoir. The inverted drops were observed every few days for crystal growth. Two different conditions were found, one with ammonium sulfate as precipitant, another with PEG 6000. Purified *T. th.* T4 particles were crystal-

lized by Sultan Agalarov in sitting drops by vapor diffusion in 1.8M ammonium sulfate, 20 mM magnesium chloride, and 50 mM potassium cacodylate (pH 6.5).

High resolution X-ray data were collected at the Stanford Synchrotron Research Laboratory on beamline 7.1 ($\lambda = 1.08 \text{ \AA}$) or beamline 9.1 ($\lambda = 0.98 \text{ \AA}$) (Agalarov, *et al.*, 2000). Crystals were harvested with a loop and transferred to a cryoprotectant solution (20% glycerol in mother liquor) before rapid freezing at 77 K and data collection. The experimental data were collected on a MAR 345 phosphorimage plate detector and the images were processed with MOSFLM (Leslie, 1994). The reflection data were merged into a complete data set, from which the space group and unit cell dimensions were determined. Heavy atom derivative crystals were soaked in 1-10 mM metal ion solution in mother liquor for 12-48 hours, and heavy atom sites were found in Patterson Maps and difference fourier methods using XtalView (McRee, 1999). Experimental phases were first calculated to 3.5 \AA by MIR with seven heavy atom derivatives using Mlphare (Otwinowski, 1994). The initial phases were extended to 2.8 \AA by NCS averaging, histogram matching, solvent flattening, and SigmaA phase matching from model building with DM (Cowtan and Main, 1998). The model was built with Xfit (Mcree, 1999) and extended to 2.6 \AA by iterative rounds of positional and B -factor refinement with CNS (Brunger, *et al.*, 1998). The protein S18 structure was determined incorrect after submission to the Protein Data Bank. The S18 structure from the 30S ribosomal subunit was incorporated into the refinement to improve the 2Fo-Fc map, and the protein was rebuilt into observable density and the sequence realigned. Residues were not incorporated where no density was observed.

4.3 Time-resolved fluorescence resonance energy transfer (trFRET).

Fluorescence intensity decays were measured by time-correlated single-photon counting. Fluorescein-labeled RNAs ($\sim 1 \text{ \mu M}$, 150 \mu L) were excited at 480 nm by short pulses ($\sim 20 \text{ ps}$ full-width at half-maximum) of vertically polarized, frequency-doubled light from a tunable Ti:Sapphire laser (Coherent 900S), pumped with 9.5 mW at 532 nm from an argon-ion laser (Coherent Verdi V-10). The laser cavity was mode-locked at 76 MHz (13.2 ns) and tuned to 960 nm. The repetition rate was reduced to 7.6 MHz by a pulse picker (Coherent 9200), and the frequency doubled to 480 nm in a $\text{KD}\text{H}_2\text{PO}_4$ crystal.

Emission from a 2 mm quartz cell mounted in a thermo-stated holder was observed perpendicular to excitation. Fluorescence emission was passed through polarizing optics at the magic angle, 54.7° , a 530 nm Schott glass low-pass cutoff filter, a monochromator at 530 nm with 2 mm slits, and the intensity measured by a microchannel plate photomultiplier (Hamamatsu R280) operated at 2.9 kV.

The laser instrument response functions (irf) were measured with a dilute scattering solution (powdered milk; 1:50 w/v) at 473 nm wavelength. The fluorescent lifetimes of the donor dyes were extracted from the decay curves by a process of convoluting the irf with a sum of two or three exponential decays and comparing the test functions to the experimental data by non-linear least squares fitting. The results of the decay fitting were compared for size of the chi-square value and appearance of the plotted residuals.

Fluorescence decay data for fluorescein-tetramethylrhodamine dye pairs labeled RNAs were collected and fit to an energy transfer model by optimizing the parameters of a weighted gaussian distribution of distances (Yang and Millar, 1996). The R_0 value used in our calculations (51.0 Å; J.W. Orr, personal communication) is slightly different from a value reported in the literature (54.3 Å; Eis and Millar, 1996), but does not significantly effect the results. Models with either one and two discrete distance distributions compared to see which best fit the data.

4.4 Single-pair fluorescence resonance energy transfer (spFRET)

Single-pair fluorescence microscopy experiments were carried out as described previously (Pljevaljic, 1994). Briefly, fluorescence measurements were carried out using a home-build laser confocal microscope system, based on an Axiovert 200 microscope (Zeiss, Thornwood, NY). Excitation was achieved by focusing the 514 -nm line of a 543-AP_A01 tunable argon-ion laser (Melles Griot, Carlsbad, CA) inside the sample solution, 10 μm from the glass coverslip surface, using a Plan Apo 100 x, 1.4 NA oil immersion objective (Zeiss). The fluorescence emission was collected using the same objective, separated from the excitation light using a dichroic filter (540 DRLP, Omega Optical, Brattleboro, VT), spatially filtered using a 100 μm pinhole, and separated into donor and acceptor components using a second dichroic filter (630 DLRP, Omega Optical). The

donor and acceptor signals were further filtered using an HQ585/60m band-pass filter (donor, Chroma Technology corp., Rockingham, VT) and a 640AELP long-pass filter (acceptor, Omega Optical), then detected using SPCM-AQR-14 avalanche photodiodes (Perkin-Elmer Optoelectronics, Fremont, CA), and the signals were recorded using a photon counting card (PCI 6602, National Instruments, Austin, TX) and computer.

The FRET efficiency histograms were generated using a two-channel data collection mode to simultaneously record donor and acceptor signals in 0.5 ms bins. The donor-acceptor RNA samples were 100 pM to ensure only single molecules in the illuminated volume. The signals were corrected for average background due to buffer, the effects of Cy3 leakage into the Cy5 channel, and direct excitation of Cy5 at 514 nm. A threshold of 40 counts (sum of signals from the two channels) was then used to separate fluorescence signals from background, and FRET efficiencies were calculated for each accepted event using the equation $E_i = I_a / (I_a + I_d)$, where I_a is the acceptor intensity, and I_d is the donor intensity.

Bibliography

Agalarov, S.C., Prasad, S. G., Funke, P. M., Stout, C. D., and Williamson, J. R. Structure of the S15,S6,S18-rRNA complex: assembly of the 30S ribosome central domain. *Science* **288**, 107 (2000).

Agalarov, S. C., and Williamson, J. R. A hierarchy of RNA subdomains in assembly of the central domain of the 30 S ribosomal subunit. *RNA* **6**, 402 (2000).

Agalarov, S. C., Zheleznyakova, E. N., Selivanova, O. M., Zheleznyadagger, L. A., Matvienko, N. I., Vasiliev, V. D., and Spirin, A. S. In vitro assembly of a ribonucleoprotein particle corresponding to the platform domain of the 30S ribosomal subunit. *Proc. Natl. Acad. Sci. U.S.A.* **95**, 999 (1998).

Ban, N., Nissen, P., Penczek, P., Hansen, J., Capel, M., Moore, P. B. and Steitz, T. A. Placement of protein and RNA structures into a 5 Å-resolution map of the 50S ribosomal subunit. *Nature* **400**, 841 (1999).

Ban, N., Nissen, P., Hansen, J., Moore, P.B., Steitz, T.A. The complete atomic structure of the large ribosomal subunit at 2.4 Å resolution. *Science* **289**, 905 (2000).

Batey, R.T., and Williamson, J.R. Interaction of the *Bacillus stearothermophilus* ribosomal protein S15 with 16 S rRNA: I. Defining the minimal RNA site. *J. Mol. Biol.* **255**, 536 (1996).

Batey, R.T., and Williamson, J.R. Interaction of the *Bacillus stearothermophilus* ribosomal protein S15 with 16 S rRNA: II. Specificity Determinants of RNA-Protein Recognition. *J. Mol. Biol.* **255**, 261 (1996).

Batey, R. T., and Williamson, J. R. Effects of polyvalent cations on the folding of an rRNA three-way junction and binding of ribosomal protein S15. *RNA* **4**, 984 (1998).

Berglund, H., Rak, A., Serganov, A., Garber, M. and Härd, T. Solution structure of the ribosomal RNA binding protein S15 from *Thermus thermophilus*. *Nature Structural Biology* **4**, 20 (1997).

Bloomfield, V. A., Crothers, D. M., Tinoco Jr, I. *Nucleic Acids: Structures, Properties, and Functions*. University Science Books, 2000.

Brünger, A. T., Adams, P. D., Clore, G. M., DeLano, W. L., Gros, P., Grosse-Kunstleve, R. W., Jiang, J.-S., Kuszewski, J., Nilges, M., Pannu, N. S., Read, R. J., Rice, L. M., Simonson, T., and Warren, G. L. Crystallography & NMR System: A New Software Suite for Macromolecular Structure Determination. *Acta Crystallographica D* **54**, 905 (1998).

Capel, M. S. and Moore, P. B. Quaternary structure of the small ribosomal subunit of *Escherichia coli* determined by neutron diffraction. *J. Appl. Cryst.* **21**, 823-827 (1988).

Carter, A.P., Clemons Jr., W.M., Brodersen, D.E., Morgan-Warren, R.J., Wimberly, B.T., and Ramakrishnan, V. Functional insights from the structure of the 30S ribosomal subunit and its interactions with antibiotics. *Nature* **407**, 340-348 (2000).

Cate, J.H., M.M. Yusupov, G.Zh. Yusupova, T.N. Earnest, and H.F. Noller. X-ray Crystal Structures of 70S Ribosome Functional Complexes. *Science* **285**, 2095 (1999).

Clemons, W. M., Davies, C., White, S. W., and Ramakrishnan, V. Conformational variability of the N-terminal helix in the structure of ribosomal protein S15. *Structure* **6**, 429 (1998).

Clemons, W.M., May, J.L.C., Wimberly, B.T., McCutcheon, J.P., Capel, M.S. and Ramakrishnan, V. Structure of a bacterial 30S ribosomal subunit at 5.5 Å resolution. *Nature* **400**, 833 (1999).

Conn, G.L., Draper, D.E., Lattman, E.E., Gittis, A.G. Crystal structure of a conserved ribosomal protein-RNA complex. *Science* **284**, 1171-1174 (1999).

Cowtan, K., and Main, P. Miscellaneous Algorithms for Density Modification. *Acta Crystallogr. D* **54**, 487 (1998).

Crick, F. Central Dogma of Molecular Biology *Nature* **227**, 561 (1970).

Culver, G. M., Cate, J. H., Yusupova, G. Zh., Yusupov, M. M., and Noller, H. F. Identification of an RNA-Protein Bridge Spanning the Ribosomal Subunit Interface. *Science* **285**, 2133 (1999).

Doudna, J., Grosshans, C., Gooding, A., and Kundrot, C. E. Crystallization of ribozymes and small RNA motifs by a sparse matrix approach. *Proc. Natl. Acad. Sci. USA* **90**, 7829 (1993).

Fahnestock, S., Erdmann, V., and Nomura, M. Reconstitution of 50S ribosomal subunits from protein-free ribonucleic acid. *Biochemistry* **12(2)**, 220 (1973)

Gabashvili, I.S., Agrawal, R.K., Spahn, C.M., Grassucci, R.A., Svergun, D.I., Frank, J., and Penczek, P. Solution structure of the E. coli 70S ribosome at 11.5 Å resolution. *Cell* **100**, 537 (2000).

Guttel, R. R. Collection of small subunit (16S- and 16S-like) ribosomal RNA structures. *Nucleic Acids Research* **22**, 3502 (1994).

Ha, T., Zhuang, X., Kim, H. D., Orr, J. W., Williamson, J. R., and Chu, S. Ligand-induced conformational changes observed in single molecule RNA molecules, *Proc. Natl. Acad. Sci. USA* **96**, 9077 (1999).

Inouye, A., Shinagawa, Y., Masamura, S., Hori, S., Irimaziri, A., and Yahara, S. Purification and Electron Microscope Observations of Ribosomes from Beef Brain Cortex. *Journal of Electron Microscopy* **13(3)**, 113-118 (1964).

Kim, H. D., Nienhaus, G. U., Ha, T., Orr, J. W., Williamson, J. R., and Chu, S. Mg²⁺-dependent conformational change of RNA studied by fluorescence correlation and FRET on immobilized single molecules. *Proc. Natl. Acad. Sci. U.S.* **99**, 4284 (2002)

- Klostermeier, D., and Millar, D. P. Time-Resolved Fluorescence Resonance Energy Transfer: A Versatile Tool for the Analysis of Nucleic Acids. *Biopolymers* **61**, 159 (2002).
- Leijonmarck, M., and Liljas, A. Structure of the C-terminal domain of the ribosomal protein L7/L12 from *Escherichia coli* at 1.7 Å. *J.Mol.Biol.* **195**, 555-579 (1987).
- Leslie, A. G. W. The CCP4 suite: programs for protein crystallography. *Acta Crystallographica D* **50**, 760 (1994).
- Lindahl, M., Svensson, L.A., Liljas, A., Sedelnikova, S.E., Eliseikina, I.A., Fomenkova, N.P., Nevskaya, N., Nikonov, S.V., Garber, M.B., Muranova, T.A., Rykonove, A. I., and Amons, R. Crystal structure of the ribosomal protein S6 from *Thermus thermophilus*. *EMBO J.* **13**, 1249 (1994).
- Lu, M., Steitz, T.A. Structure of *Escherichia coli* ribosomal protein L25 complexed with a 5S rRNA fragment at 1.8-Å resolution. *Proc.Natl.Acad.Sci.USA* **97**, 2023-2028 (2000).
- McRee, D. E. XtalView/Xfit—A Versatile Program for Manipulating Atomic Coordinates and Electron Density. *J. Struct. Biol.* **125**, 156 (1999).
- Moazed, D., and Noller, H. F. Binding of tRNA to the ribosomal A and P sites protects two distinct sets of nucleotides in 16 S rRNA. *J. Mol. Biol.* **211**, 135 (1990).
- Mueller, F., Sommer, I., Baranov, P., Matadeen, R., Stoldt, M., Wohnert, J., Gorlach, M., van Heel, M., and Brimacombe, R. The 3D arrangement of the 23 S and 5 S rRNA in the *Escherichia coli* 50 S ribosomal subunit based on a cryo-electron microscopic reconstruction at 7.5 Å resolution. *J. Mol. Biol.* **298**, 35 (2000).
- Nikulin, A., Serganov, A., Ennifar, E., Tishchenko, S., Nevskaya, N., Shepard, W., Portier, C., Garber, M., Ehresmann, B., Ehresmann, C., Nikonov, S., and Dumas, P. Crystal structure of the S15-rRNA complex. *Nat.Struct.Biol.* **7**, 273-277 (2000).

- Nomura, M. Assembly of Bacterial Ribosomes: In vitro reconstitution systems facilitate study of ribosome structure, function, and assembly. *Science* **179**, 864-873 (1973).
- Orr, J. W., Hagerman, P. J., and Williamson, J. R. Protein and Mg²⁺-induced conformational changes in the S15 binding site of 16 S ribosomal RNA. *J. Mol. Biol.* **275**, 453 (1998).
- Otwinowski, Z. The CCP4 suite: programs for protein crystallography. *Acta Crystallographica D* **50**, 760 (1994).
- Pestka, S. Inhibitors of ribosome functions. *Annual Review of Microbiology* **25**, 1580 (1971).
- Pljevaljcic, G, Millar, DP, Deniz, AA. Freely-diffusing single hairpin ribozymes provide insights into the role of secondary structure and partially folded states in RNA folding. *Biophysical Journal* **87**, 457 (2004).
- Powers, T., and Noller, H. F. Hydroxyl radical footprinting of ribosomal proteins on 16S rRNA. *RNA* **1**, 194 (1995).
- Recht, M. I. and Williamson, J. R. Central domain assembly: thermodynamics and kinetics of S6 and S18 binding to an S15-RNA complex. *JMB* **313**, 35 (2001).
- Recht, M. I. and Williamson, J. R. RNA Tertiary Structure and Cooperative Assembly of a Large Ribonucleoprotein Complex. *JMB* **344**, 395 (2004).
- Samaha, R. R., O'Brien, B., O'Brien, T. W., and Noller, H. F. Independent in vitro Assembly of a Ribonucleoprotein Particle Containing the 3' Domain of 16S rRNA. *Proc. Natl. Acad. Sci. U.S.A.* **91**, 7884 (1994).
- Sambrook, J., Fritsch, E. F., and Maniatis, T. Molecular Cloning: A Laboratory Manual. *Cold Spring Harbor Laboratory Press*, 2nd edition (1989).

Schluzen, F., Tocilj, A., Zarivach, R., Harms, J., Gluehmann, M., Janell, D., Bashan, A., Bartels, H., Agmon, I., Franceschi, F., and Yonath, A. Structure of functionally activated small ribosomal subunit at 3.3 angstroms resolution. *Cell* **102**, 615 (2000).

Stoldt, M., Wohnert, J., Ohlenschlager, O., Gorlach, M., Brown, L.R. The NMR structure of the 5S rRNA E-domain-protein L25 complex shows preformed and induced recognition. *EMBO J.* **18**, 6508 (1999).

Svensson, P., Changchien, L.M., Craven, G.R., and Noller, H.F. Interaction of ribosomal proteins, S6, S8, S15 and S18 with the central domain of 16 S ribosomal RNA. *J. Mol. Biol.* **200**, 301 (1988).

Tocilj, A., Schlunzen, F., Janell, D., Gluhmann, M., Hansen, H.A., Harms, J., Bashan, A., Bartels, H., Agmon, I., Franceschi, F., and Yonath, A. The small ribosomal subunit from *Thermus thermophilus* at 4.5 Å resolution: pattern fittings and the identification of a functional site. *Proc. Natl. Acad. Sci. USA* **96**, 14252 (1999).

Traub, P. and Nomura, M. Structure and function of *E. coli* ribosomes. Reconstitution of functionally active 30S ribosomal particles from RNA and proteins. *Proc. Natl. Acad. Sci. USA* **59**, 777 (1968)

Wimberly, B.T., Brodersen, D.E., Clemons, W.M. Jr., Carter, A.P., Morgan-Warren, R.J., Vornrhein, C., Hartsch, T. and Ramakrishnan, V. Structure of the 30S ribosomal subunit. *Nature* **407**, 327 (2000).

Wimberly, B.T., Guymon, R., McCutcheon, J.P., White, S.W., and Ramakrishnan, V. A detailed view of a ribosomal active site: the structure of the L11-RNA complex. *Cell* **97**, 491 (1999).

Yang, M., and Millar, D. P. Conformational Flexibility of Three-Way DNA Junctions Containing Unpaired Nucleotides. *Biochemistry* **35**, 7959 (1996).

Yonath A., Leonard K. R., and Wittmann, H.G. A tunnel in the large ribosomal subunit revealed by three-dimensional image reconstruction. *Science* **236**, 813 (1987).

Yusupov, M. M., Yusupova, G. Z, Baucom, A. Lieberman, K, Earnest, T. N., Cate, J. H. D., and Noller, H. F. Crystal structure of the ribosome at 5.5 Å resolution. *Science* **292**, 883 (2001).